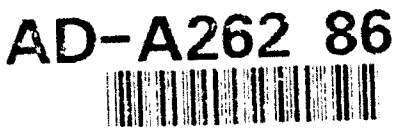

NAVAL POSTGRADUATE SCHOOL

Monterey, California

THESIS

DESIGN OF A HIGH RESOLUTION
SPATIAL HETERODYNE
INTERFEROMETER

by

Kenneth M. Wallace, Jr.

December, 1992

Thesis Advisor: D. D. Cleary

Approved for public release; distribution is unlimited.

REPORT DOCUMENTATION PAGE

1a. REPORT SECURITY CLASSIFICATION Unclassified	1b RESTRICTIVE MARKINGS
2a. SECURITY CLASSIFICATION AUTHORITY	3 DISTRIBUTION/AVAILABILITY OF REPORT Approved for public release; distribution is unlimited.
2b. DECLASSIFICATION/DOWNGRADING SCHEDULE	
4 PERFORMING ORGANIZATION REPORT NUMBER(S)	5 MONITORING ORGANIZATION REPORT NUMBER(S)
6a. NAME OF PERFORMING ORGANIZATION Naval Postgraduate School 6b OFFICE SYMBOL *(If applicable)* 31	7a NAME OF MONITORING ORGANIZATION Naval Postgraduate School
6c. ADDRESS *(City, State, and ZIP Code)* Monterey, CA 93943-5000	7b ADDRESS *(City, State, and ZIP Code)* Monterey, CA 93943-5000
8a. NAME OF FUNDING/SPONSORING ORGANIZATION 8b OFFICE SYMBOL *(If applicable)*	9 PROCUREMENT INSTRUMENT IDENTIFICATION NUMBER
8c. ADDRESS *(City, State, and ZIP Code)*	10 SOURCE OF FUNDING NUMBERS Program Element No / Project No / Task No / Work Unit Accession Number
11 TITLE *(Include Security Classification)* Design of a High Resolution Spatial Heterodyne Interferometer	
12 PERSONAL AUTHOR(S) Kenneth M. Wallace, Jr.	
13a. TYPE OF REPORT Master's Thesis 13b TIME COVERED From To	14 DATE OF REPORT *(year, month, day)* December 1992 15 PAGE COUNT 111
16. SUPPLEMENTARY NOTATION The views expressed in this thesis are those of the author and do not reflect the official policy or position of the Department of Defense or the U. S. Government.	
17. COSATI CODES FIELD / GROUP / SUBGROUP	18. SUBJECT TERMS *(continue on reverse if necessary and identify by block number)* Spectroscopy, Spatial Heterodyne Spectroscopy, High Resolution Interferometer, Optical Design, Interferometer, Diffraction Grating Interferometer.

19. ABSTRACT *(continue on reverse if necessary and identify by block number)*

Several new spatial heterodyne interferometers were evaluated using ray tracing analysis. A spherical grating interferometer was examined and found to have nonlinear fringe patterns that are difficult to interpret. A new plane grating interferometer was designed, built and tested using a visible light laser as the source. The new design uses two mirrors and a single, planar diffraction grating to divide and recombine incident collimated light. The zero and first order ray paths recombine to produce a high contrast, linear, interference fringe pattern suitable for Fourier Transform analysis. The instrument has the potential to perform extremely high resolution spectroscopy in the FUV and EUV portions of the electromagnetic spectrum with resolving powers on the order of 10^6. High resolution analysis of emission line profiles should enable an observer to more accurately determine atmospheric temperature and density profiles. The simple, lightweight and compact instrument has no moving parts and is suitable for remote sensing from sounding rocket or satellite platforms.

20. DISTRIBUTION/AVAILABILITY OF ABSTRACT ☒ UNCLASSIFIED/UNLIMITED ☐ SAME AS REPORT ☐ DTIC USERS	21 ABSTRACT SECURITY CLASSIFICATION Unclassified
22a NAME OF RESPONSIBLE INDIVIDUAL David D. Cleary	22b TELEPHONE *(Include Area code)* (408) 656-2828 22c OFFICE SYMBOL PH / CL

DD FORM 1473, 84 MAR 83 APR edition may be used until exhausted
All other editions are obsolete

SECURITY CLASSIFICATION OF THIS PAGE
Unclassified

Approved for public release; distribution is unlimited.

Design of a High Resolution

Spatial Heterodyne Interferometer

by

Kenneth M. Wallace, Jr.
Lieutenant Commander, United States Navy
B.S., United States Naval Academy, 1978

Submitted in partial fulfillment of the
requirements for the degrees

MASTER OF SCIENCE IN PHYSICS

and

MASTER OF SCIENCE IN ENGINEERING SCIENCE (ASTRONAUTICS)

from the

NAVAL POSTGRADUATE SCHOOL
December 1992

Author: _____
Kenneth M. Wallace, Jr.

Approved By: _____
D. D. Cleary, Thesis Advisor

_____
O. Biblarz, Co-Advisor

_____
K. E. Woehler, Chairman, Department of Physics

_____
D. J. Collins, Chairman, Department
of Aeronautics and Astronautics

ABSTRACT

Several new spatial heterodyne interferometers were evaluated using ray tracing analysis. A spherical grating interferometer was examined and found to have nonlinear fringe patterns that are difficult to interpret. A new plane grating interferometer was designed, built and tested using a visible light laser as the source. The new design uses two mirrors and a single, planar diffraction grating to divide and recombine incident collimated light. The zero and first order ray paths recombine to produce a high contrast, linear, interference fringe pattern suitable for Fourier Transform analysis. The instrument has the potential to perform extremely high resolution spectroscopy in the FUV and EUV portions of the electromagnetic spectrum with resolving powers on the order of 10^6. High resolution analysis of emission line profiles should enable an observer to more accurately determine atmospheric temperature and density profiles. The simple, lightweight and compact instrument has no moving parts and is suitable for remote sensing from sounding rocket or satellite platforms.

TABLE OF CONTENTS

LIST OF TABLES

LIST OF FIGURES

I. INTRODUCTION

The Naval Postgraduate School (NPS), in cooperation with the Naval Research Laboratory (NRL), has conducted two sounding rocket experiments since March 1990. The purpose of the experiments has been to study the ionosphere. One of the experimental payloads aboard the sounding rockets is an instrument called the MUSTANG (Middle Ultraviolet Spectrograph). The MUSTANG was designed and built by the NPS Physics Department to perform medium resolution observations of the ionosphere for emissions in the middle ultraviolet band of the electromagnetic spectrum. In the same year, Nichols (1990) at NPS began to investigate new high resolution instrument designs to observe the far ultraviolet (FUV) portion of the spectrum. He designed and built a prototype interferometer using all-reflective optics and a spherical grating. A feasibility test with a visible light source was conducted in the laboratory (Cleary et al., 1992) This thesis is a continuation of that project.

The requirements to study the ionosphere have been established by many organizations, including the Department of Defense (DOD). Mapping of the electron density in the ionosphere is one specific requirement, for it has important implications with the transmission of electromagnetic waves. The mapping task is not simple because the ionosphere is very dynamic and complex. Local snapshots of certain parameters are obtained today by systems that measure portions of the ionosphere from ground or sounding rocket platforms. In order to observe broader regions and measure other parameters, it is desirable to have an instrument capable of remote sensing from a satellite. This is the ultimate goal for the instrument presented in this thesis.

The focus of this thesis is to develop a high resolution interferometer suitable for use in aeronomy, which is the scientific term for the study of planetary atmospheres. Although the interferometer may have applications in aeronomy for other planets, the focus for this instrument is

on the earth's atmospheric emissions in the FUV band of 1000 to 2000 Å. Specific constituents can be identified by detection of these emissions with lower resolution, broad band instruments. A high resolution interferometer will serve as the tool to perform a detailed study of a specific emission line in order to extract temperature or radiation transport information. The next generation interferometer from this basic design may concentrate on wavelengths below 1000 Å in the extreme ultraviolet (EUV) region.

A. THESIS OBJECTIVES

The primary objective for this thesis was to design an instrument with the potential to meet the requirement for a high resolution FUV interferometer suitable for ionospheric studies. This objective was first pursued by conducting a ray trace analysis of a previous design. Initial results of the ray tracing led to a redesign of the instrument. A new prototype was built, and a feasibility test was performed in the laboratory by using visible light.

The design constraints remained the same as the previous design, (Nichols, 1990). Specifically, these constraints were to :

1. Operate in the FUV and EUV (reflective surfaces only).
2. Be sensitive to low intensity atomic emissions (minimize losses).
3. Have a high resolution across a narrow bandwidth.
4. Be compact and lightweight.
5. Be suitable for the space flight environment.
6. Be economical and cost effective (additionally imposed constraint).

B. THESIS OUTLINE

Chapter II includes an overview of the earth's atmosphere, the ionosphere and the electromagnetic propagation characteristics. Ionospheric observations and motivation for study are also discussed, along with background on the ray trace programs used in the thesis. The theory in Chapter III includes a brief review of interference and diffraction theory, interferometric devices

and spectral line broadening. Chapter IV provides the procedures and results for the ray tracing and the feasibility test of the interferometer. Chapter V discusses the conclusions and recommendations for further study. The Appendices provide the text files from the ray trace programs.

II. BACKGROUND

This chapter provides the foundation and motivation behind the development of an FUV interferometer. The earth's atmosphere is discussed as the medium of interest. A high resolution interferometer provides the tool to analyze and understand in more detail the processes, profiles and dynamics in the atmosphere. A deeper understanding of the atmosphere enhances the applications in fields such as communications, navigation, and over-the-horizon radar (OTHR), the environmental sciences and astronomy.

A. ATMOSPHERE OF THE EARTH

The following is a general overview with emphasis on specific areas of interest pertaining to the FUV interferometer and its applications. A detailed description of the atmosphere is beyond the scope of this thesis, but it may be found in a text such as Green and Wyatt (1965).

The atmosphere of the earth is generally categorized by a physical variable or property such as temperature, composition, chemical reactions and electrical characteristics. These categories divide the atmosphere into "shells" containing common properties or characteristics.

1. Atmospheric Temperature and Composition Profile

Four regions or shells make up the temperature divisions of the atmosphere. Each shell is separated by a transition region typically defined by an inflection point on the temperature profile. The troposphere is the lowest region, followed by the stratosphere, mesosphere, and the thermosphere. Different sources provide the warming in certain portions of the atmosphere. In the case of the troposphere, the surface of the earth provides the warming. In the stratosphere warming is caused by the absorption of UV solar radiation by the ozone. The heating in the highest region, the thermosphere is caused by solar wavelengths at less than 1750 Å. This region is of the most interest for applications discussed in this thesis. The temperature and composition distributions of the atmosphere are illustrated in Figure 1.

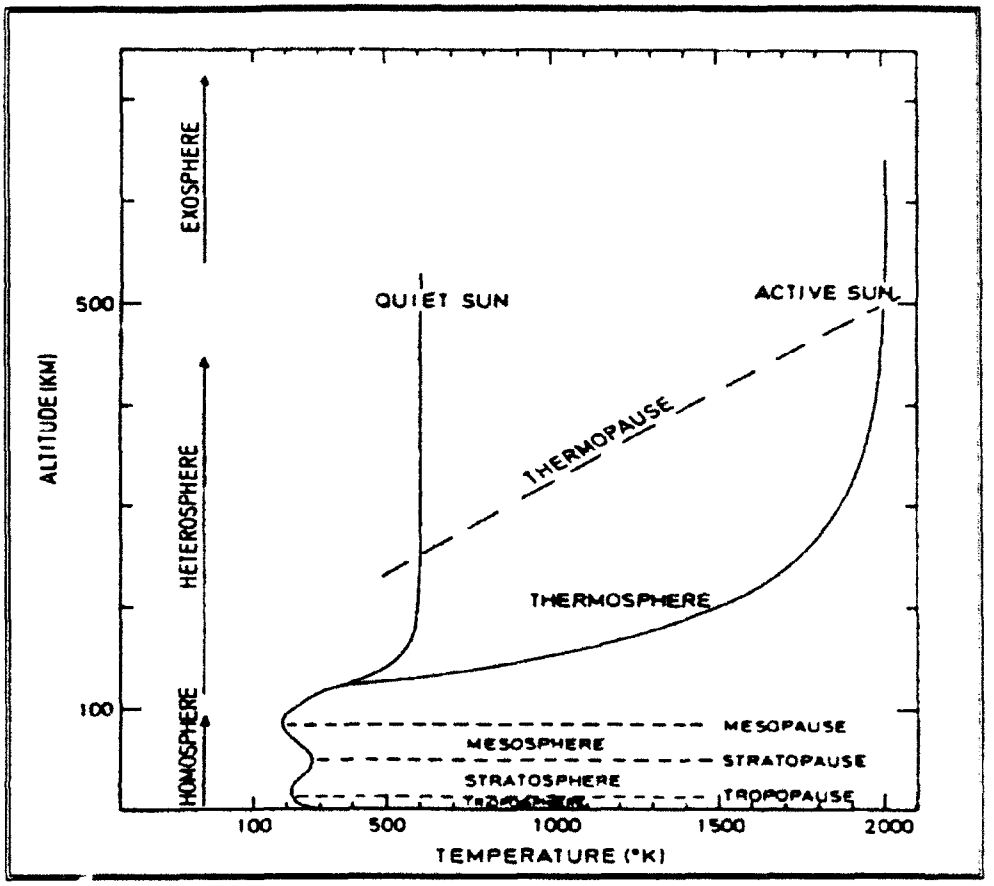

Figure 1 Atmospheric Regions and Temperature Profile
(from Banks and Kockarts, 1973)

Three regions or shells can be described by categorizing the atmosphere according to its composition. The homosphere is the lowest region, extending from the surface to the homopause located at an altitude of about 80 - 100 km. Below the homopause, the mean molecular weight is constant with fairly uniform composition, and the primary transport mechanism is eddy diffusion.

The heterosphere lies above the homopause and has a significant variation of composition with altitude. Molecular weight decreases with increasing altitude and molecular dissociation begins to occur. Unlike the homosphere, there is very little vertical mixing in the heterosphere. The atmospheric constituents diffuse at a rate that depends on their atomic mass. Molecular

diffusion is the primary transport mechanism in the heterosphere. Above a certain altitude, collision between atoms becomes extremely remote. This altitude is called the critical level and marks the start of the exosphere. At this critical level, a fraction of the high velocity particles may have a trajectory that allows them to escape the earth's atmosphere.

2. Ionosphere

The ionosphere is that region of the atmosphere where electrical properties affect the propagation of electromagnetic radiation. Although electrically neutral as a whole, the ion mass can be over 50,000 times as massive as the electron mass; hence, ion mobility is significantly less than electron mobility and can be ignored for the general case. It is the free-moving electrons that interact with radio waves and are of primary interest in the study of the ionosphere. Knowledge of the electron density profiles enhances accurate predictions of the propagation characteristics for the ionosphere.

The ionization processes that occur in the ionosphere are many and complex. A detailed description can be found in Banks and Kockarts (1973). The primary process for electron production is the photoionization process generalized by

$$M + h\nu = M^{+} + e^{-} \quad , \qquad (1)$$

where M is either a molecule or atom, $h\nu$ is the photon, M^{+} is the ion and e^{-} is the electron. The ionization rate will be a function of the density of the species M and photon flux, all of which vary with altitude.

The ionosphere is divided into several layers which vary with night, day, latitude and solar cycle. The superposition of these layers constructs the profile of the ionosphere. The lowest layer is the D region, which extends from 50 to 90 km with a maximum density of $10^{3} e / cm^{3}$. This region is only weakly ionized during the day and may completely disappear at night, except in the auroral and polar latitudes. Molecules of O_2 and N_2 are ionized by X-ray radiation, and NO is ionized by due to Lyman α radiation at 1216 Å. Figure 2 illustrates the average daytime electron

density distribution and the principle ions in the ionosphere, along with the incident radiation at various levels.

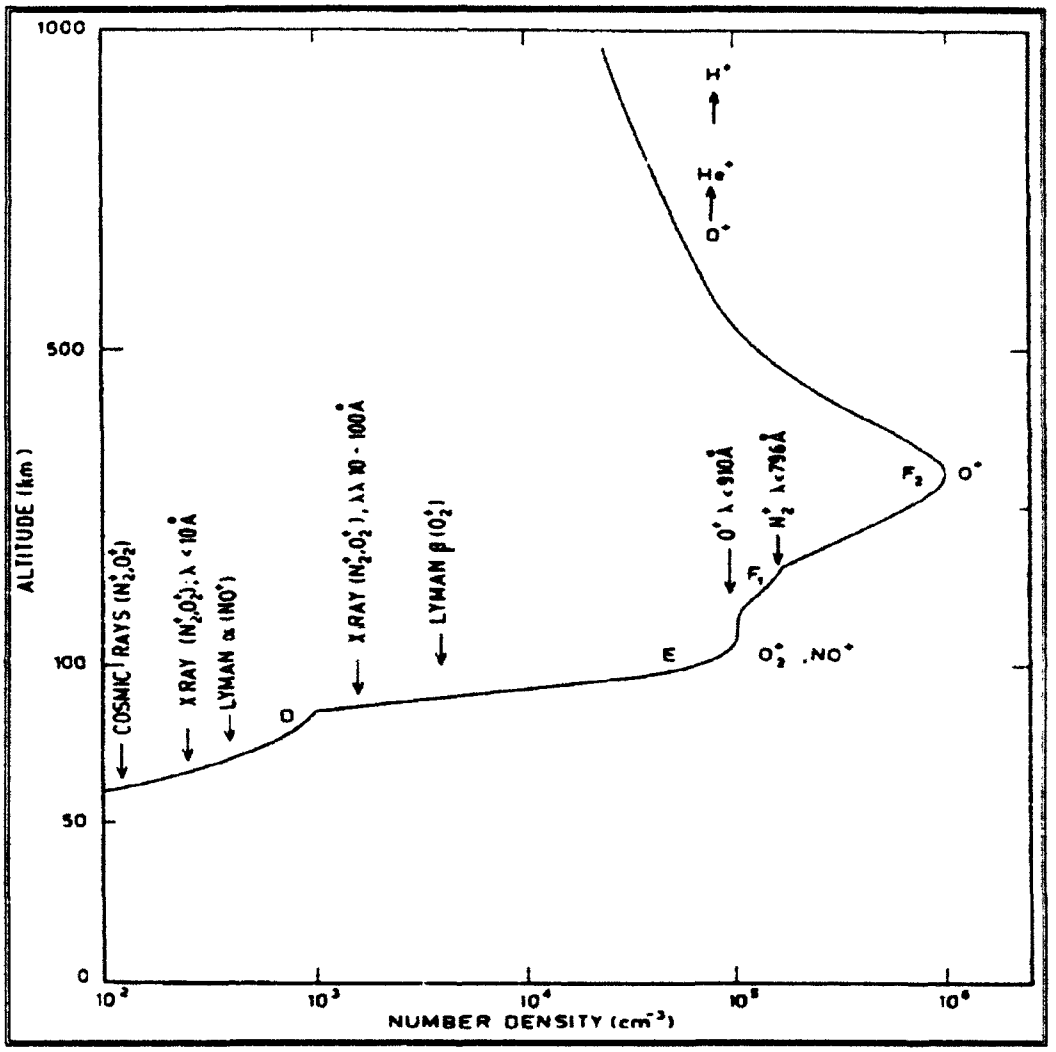

Figure 2
Average Daytime Electron Distribution, Principal Ions and Regions
(from Banks and Kockarts, 1973)

The E region extends from 85 to 140 km with a daylight maximum electron density of approximately 10^5 *e* / cm^3 at 100 km. The E region diminishes at night to low electron densities

that are latitude dependent. Soft X-rays and ultraviolet incident radiation is responsible for the production of the dominant ion species NO^+ and O_2^+ in this region.

The final region is broken down into the F_1 and F_2 layers. The F_1 extends from 140 to 200 km and creates a daytime ledge of the F_2 region, which extends above 200 km. Electron density of the F_1 region may be as high as $3x10^5 e$ / cm^3. This density is directly proportional to the amount of solar activity. The F_2 region contains the largest electron density ($2x10^6 e$ / cm^3 in the day and about 10^5 at night). The F_1 and F_2 regions merge to form a single region at night.

3. Electromagnetic Wave Propagation

The ionospheric influence on radio waves is significant and is the basis for a great deal of interest in the investigation of the ionosphere. The radio frequency (RF) atmospheric window ranges from 10 MHZ - 20 GHZ. Due to interaction with electrons, radio wave frequencies must be higher than what is termed the "plasma frequency" in order to pass through the atmosphere and communicate with a satellite or probe. The plasma frequency is the natural oscillation that electrons have about stationary ions. Reflection of RF waves occurs if frequencies are below this critical frequency. This reflection is desired for OTHR and "skip" communications, but the characteristics of the "mirror" must be known to evaluate system performance and accuracy. This establishes the DOD requirement for an accurate electron density "map" of the ionosphere.

B. OBSERVATIONS OF THE IONOSPHERE

Observations of the ionosphere have been conducted by numerous sources to date. The observations may be from ground RF stations, sounding rockets or satellites, with each having their advantages. One major limitation of ground based ionosonde systems is that they provide local layer data only, and must be combined with other ionosonde systems around the world to provide any kind of global coverage. The ultimate goal is to determine the electron density profiles

of the ionosphere on a continuous basis and with increased global coverage. Remote sensing from a space based platform has the most potential.

1. NPS Observations

NPS has been working with the Naval Research Laboratory (NRL) in performing ionospheric observations from sounding rockets. Two rockets have been launched from the White Sands Missile Range in New Mexico with two instruments onboard. One instrument, NRL's HIgh Resolution Airglow and Aurora Spectrograph (HIRAAS), observes the F_2 region for O^+ emissions at 834 Å. HIRAAS is an electro-photographic instrument with a band width of 500 to 1500 Å and a resolvable wavelength difference ($\Delta\lambda$) estimated to be between 0.1 to 0.5 Å. The other instrument is the MUSTANG, which observes emissions primarily from N_2 and NO in a band width of 1800 to 3400 Å. The MUSTANG has a resolution of about 10 Å (Anderson, 1990; Chase, 1992). The MUSTANG uses an Ebert-Fastie spectrograph configuration and is scheduled for another launch in 1993 from Poker Flat, Alaska.

The Ionospheric Spectroscopy And Atmospheric Composition (ISAAC) instrument is a second-generation MUSTANG being designed at NPS for follow-on experiments. Designed to have a resolution of about 1.5 Å, this instrument is scheduled to be launched in 1995 on a low earth orbiting science satellite called ARGOS.

2. Motivation for Study

The MUSTANG is satisfactory for performing broad bandwidth observations at medium resolution. The resolving power of the MUSTANG is approximately $\lambda/\Delta\lambda = 2500/10 = 250$, which is adequate for identifying spectral line intensity and, therefore, composition of the atmosphere. The second-generation ISAAC will have a resolving power on the order of 10^3. This should provide the capability to measure neutral temperatures in the thermosphere. (Cleary et al., 1992)

With an instrument capable of obtaining a resolving power on the order of 10^6, a detailed analysis of the emission line profiles could be accomplished. From this analysis, radiation transport and more accurate temperature information could be extracted from the emission lines (Cleary et al., 1992). In addition, there is the potential to use the higher resolution to single out individual emission lines from the strong solar continuum or to isolate very close emission lines. An example is the atomic oxygen triplet in the 1304 Å region. With detailed analysis of the 1304 Å emission, an estimation of atomic oxygen density can be inferred. This is the motivation behind the high resolution interferometer design in this thesis.

C. RAY TRACING PROGRAMS

Two personal computer programs were used to conduct the ray trace analysis of the designed interferometers. One program is a commercial product, and the other was developed at NPS. The programs are based on geometric optic principles and not the electromagnetic wave theory. The brief descriptions include the input and output format for each program, as well as the capabilities, limitations, and characteristics.

1. Beam Four Optical Ray Tracer

Beam Four is a ray tracing program that was developed by and is commercially distributed by Stellar Software in Berkeley, CA. The program runs on DOS-based personal computers and provides accuracy to 12 significant figures when used with a math coprocessor. A detailed discussion of the theory of ray tracing is available in Kingslake (1978).

The input format consists of tabulated data for the type and position of both source and optical elements. The source data is listed in a file with a ".RAY" file extension name, which lists the wavelength, position, initial angle of each ray, along with a column for goal and actual final position. The optical elements file is given an ".OPT" file extension and lists the type, position, size, orientation and desired diffraction order. Beam Four has an AUTOADJUST feature that

solves iteratively for a solution to optimize position or shape of an optical element for a desired or "goal" outcome.

Beam Four output comes in a variety of formats, including quantitative tables, plots, and a diagram of system layout. Performance of the optical system may be evaluated with tolerance error calculations and spot diagram analysis.

Beam Four was designed as a ray tracer and does not take into account the electromagnetic wave theory principles. A ray has no lateral width, angular parameters or polarization. The program provides ray path information only.

2. Dudley Atkinson Ray Tracer (DART)

DART is a personal computer program developed as a thesis project at the Naval Postgraduate School. The program is based on a FORTRAN ray tracing code written by Diane Prinz at NRL in Washington, D.C. The initial code was converted into a Turbo Pascal programming code with additional features. For a detailed description with supporting documentation, see Atkinson (1993).

A user-friendly screen format enables the user to input beam source and optical elements into one file tagged with a ".RTD" file extension. Wavelength, position and orientation of ray source is input, followed by the optical elements in the sequence of ray path interaction. Optical elements are specified by type, size, position, orientation, and desired diffraction order.

Output formats include text files of run results, spot diagrams and interference diagrams. Calculation accuracy is at least to 14 significant figures using a math coprocessor. The interference feature was added on to the initial code and provides an interference pattern based on path length differences. Input rays can be randomly scattered and then re-run with the same pseudo-random scatter on different optics for interference analysis.

DART has the same restriction as Beam Four in that it is a geometric optics ray tracer and does not take into account the electromagnetic wave theory. Each ray has no lateral width or angular parameter.

III. THEORY

The following discussion provides the foundation necessary to describe the operation of the interferometer. First, a review of interference and diffraction properties is presented, followed by a discussion of diffraction gratings and interferometric devices. Lastly, a brief discussion on spectral line broadening is presented as substance for the purpose of a high resolution interferometer.

Optical devices are described with applications in the visible portion of the electromagnetic spectrum and then are developed to include the ultraviolet portion of the spectrum. A detailed discussion is beyond the scope of this thesis but may be referenced from the optics text sources such as Hecht (1968), Young (1986), or Jenkins and White (1976).

A. INTERFERENCE AND DIFFRACTION

Interference and diffraction are presented separately, although distinction between the two is sometimes used interchangeably.

1. Interference

Interference is the phenomenon that occurs when radiation emanating from a source recombines after traveling over two different paths. Interference can be described with the classical wave theory of light.

There are two transverse vector components that make up light, the magnetic field and the electric field. It is the electric field intensity E, or actually, the time average of the magnitude of the electric field intensity squared, $E * E = \langle E^2 \rangle$, that is of most interest in optics. This quantity, called irradiance (I), is what is actually sensed by a detector.

The first discussion relates to the superposition of two waves emanating from the same source and traveling in the same direction. To simplify the development, assumptions are made in

order to perform scalar manipulations of what is generally a vector representation of a light wave equation. If the polarization of two waves are aligned, the magnitudes of the electric field intensity are equal, and the phase difference between the two waves is ϕ. The complex representation for two waves emanating from the same source traveling in the x direction are

$$E_1 = Ae^{-i(kx-\omega t)} \tag{2}$$

and

$$E_2 = Ae^{-i(kx-\omega t+\phi)} \quad , \tag{3}$$

where A is the field amplitude, k is the wave number ($k = 2\pi/\lambda$), ω is the angular frequency, and ϕ is the phase shift or difference between the two waves.

The sum of the electric fields is

$$E = E_1 + E_2 = Ae^{-i(kx-\omega t)}(1+e^{-i\phi}) \quad , \tag{4}$$

where the last parenthetical term may be rewritten

$$(1+e^{-i\phi}) = e^{-i\frac{\phi}{2}}(e^{-i\frac{\phi}{2}} + e^{i\frac{\phi}{2}}) = 2e^{-i\frac{\phi}{2}}\cos(\frac{\phi}{2}) \quad . \tag{5}$$

Now the irradiance may be written

$$I = E^* E = 4A^2\cos^2(\frac{\phi}{2}) \quad , \tag{6}$$

which is a maximum when $\phi = 2m\pi$ and a minimum for $\phi = (2m+1)\pi$ for any integer m or zero.

A plane of constant phase that is perpendicular to the direction of propagation is called a wave front. Interference can result after the splitting of a wave front into two paths, which creates a phase shift due to a path length difference. In fact, the phase difference ϕ is really a combination of path length difference and initial phase shift difference.

Wave front splitting and amplitude splitting are common as beam splitter processes in an interferometer. Amplitude splitting occurs in a partially silvered glass that a Michelson interferometer uses and is discussed in the Interferometric Devices section.

The best example of wave front splitting may be the double-slit interference example. For the illustration, assume a monochromatic plane wave strikes an opaque screen with two infinitesimally narrow slits spaced a distance *d* apart as is depicted in Figure 3.

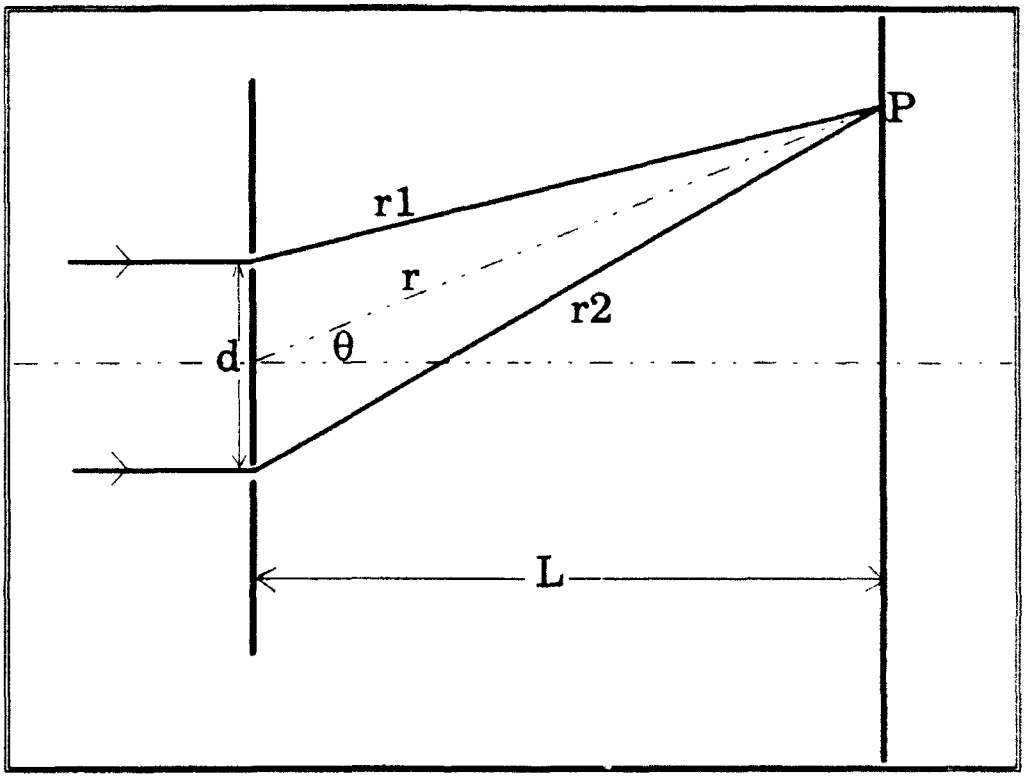

Figure 3 Double-Slit Interference

With the screen a large distance (L) away from the slits, the path length difference, which in the above figure is $\mathbf{r_2}$-$\mathbf{r_1}$, is approximately equal to $\mathbf{d}\sin\theta$. The optical path difference is therefore defined as: OPD = $\mathbf{d}\sin\theta$. The resultant E field at point P can be written as

$$E = Ae^{-i(kr_1-\omega t)}(1+e^{-ikd\sin\theta}) \quad , \tag{7}$$

which is similar to Equation 4, except that the phase difference in this case is given by $\phi = kd\sin\theta$.

The irradiance is rewritten with a substitution for the wave number,

$$I = 4A^2 \cos^2(\frac{\phi}{2}) = 4A^2 \cos^2(\frac{kd \sin\theta}{2}) = 4A^2 \cos^2(\frac{\pi d \sin\theta}{\lambda}) \quad . \qquad (8)$$

Equation 8 shows that irradiance is a maximum when the OPD is an integer multiple of λ ($OPD = m\lambda$) and is a minimum when $OPD = (m+1/2)\lambda$.

The double-slit interference pattern will not extend off to infinity from the center line axis for two reasons: The first reason is from the assumption of infinitesimally wide slits radiate uniformly in all directions. Due to diffraction effects, the light does not radiate uniformly but actually falls off to zero for large angles. Diffraction is discussed in the next section. The other reason fringe degradation occurs is due to the coherence length as discussed below.

Figure 4 depicts light incident on a double slit. The light has a coherence length (Δx_C) which is characteristic for a quasi monochromatic light wave. Light does not propagate as a perfect sinusoid but rather in wave groups that appear sinusoidal for some specified coherence length. This is described as a photon wave train. In part (a) of the figure, the OPD exceeds the coherence length, and identically paired wave groups do not arrive at P at the same time. In Figure 4(b), the OPD is within the coherence length; therefore, the phases are somewhat correlated, forming a stable interference pattern. If the coherence length is long, as is the case with a laser, the OPD can vary over a greater range for stable interference patterns. It is for this reason interference patterns are easy to produce with a laboratory laser.

Coherence length is not constant for a particular radiation source. Each transition has an associated coherence length. Coherence length is related to coherence time (Δt_c) by the speed of light c,

$$\Delta x_c = c\Delta t_c \quad . \qquad (9)$$

The coherence time is inversely related to the frequency line width of a spectral line. This ties in

with the line broadening mechanisms discussed later in this chapter. Therefore, a measure of the coherence length provides information on the line width of a spectral line.

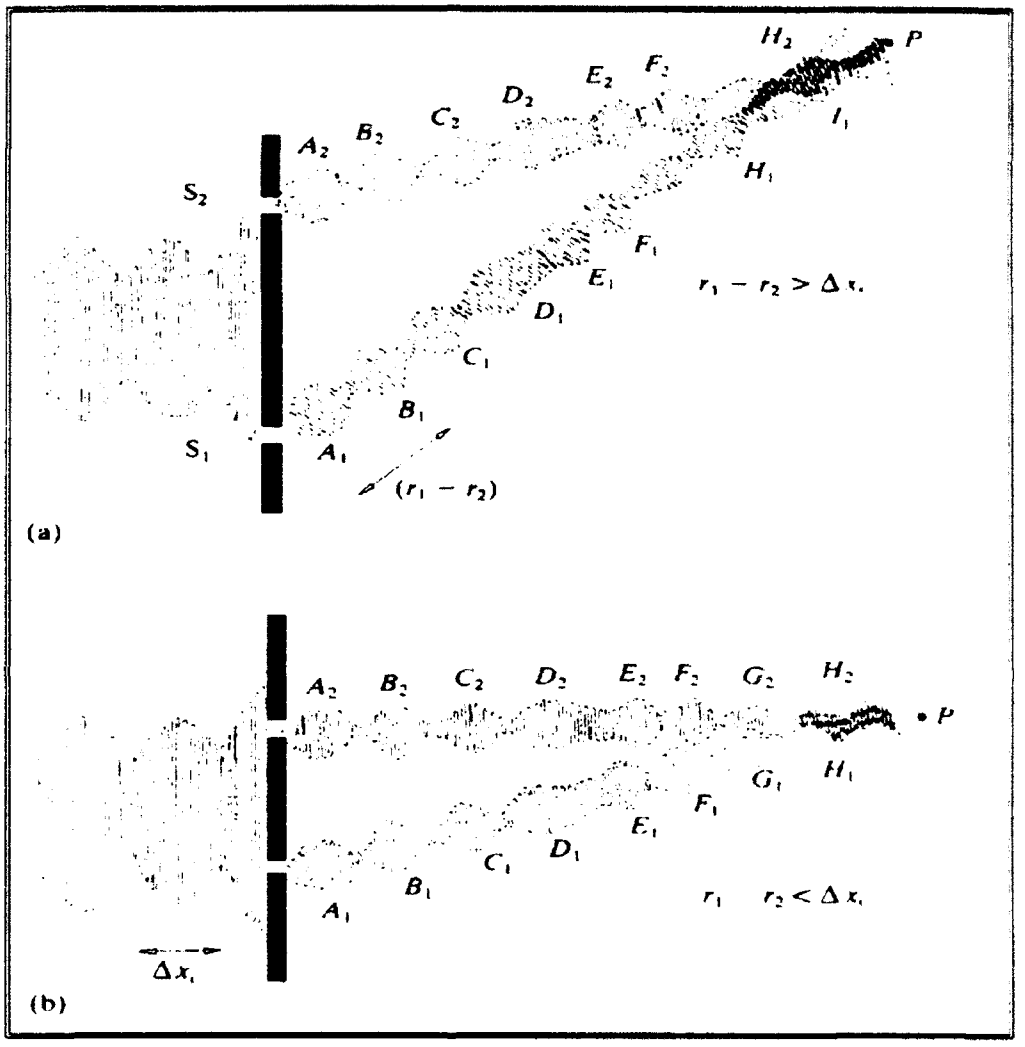

Figure 4 Coherence Length Illustration (from Hecht, 1987)

2. Diffraction

Diffraction is the phenomenon that occurs when wave fronts interact with an obstruction. Generally, diffraction theory is broken into two regions of interest: The first is the near field, when the plane of observation is in near proximity to the obstruction. The second is the far field,

whereby the plane of observation and the source is distant to the obstruction. The far field or Fraunhofer diffraction is applicable to this thesis and is the only portion discussed.

In order to model diffraction characteristics, it is common to use Huygens's construction. The basis for Huygens's construction is that for every point across an aperture, there radiates an individual spherical wavelet. When the wavelets are combined, they produce a wave front corresponding to a constant phase as illustrated in Figure 5. In the central portion of the aperture, the wave fronts continue to propagate in the same direction that is normal to the aperture. Closer in toward the edges of the aperture, "bending" takes place. Ultimately at far distances from the aperture, the entire wave fronts become spherical.

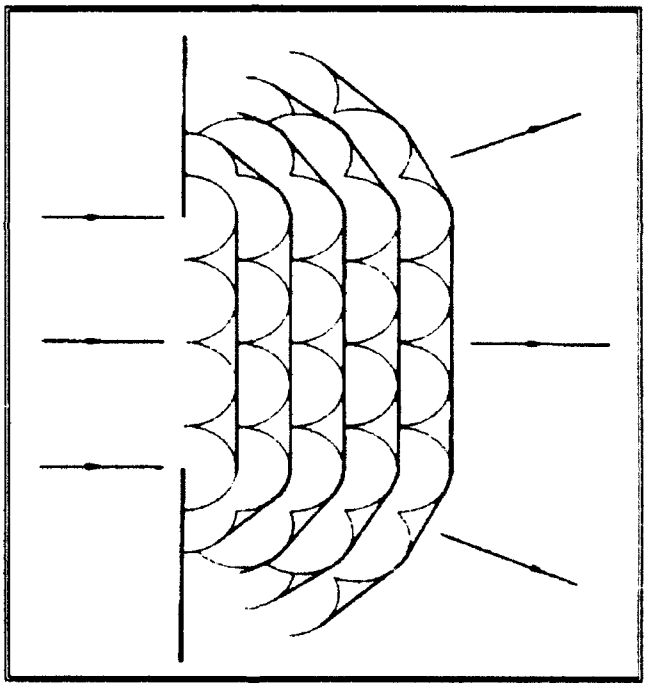

Figure 5 Huygens's Construction (from Young, 1986)

The wave fronts in the last figure can be applied to the constant phase points on the spherical wavelets emanating from multiple slits. If an opaque screen with multiple slits is illuminated by monochromatic light, the wave fronts propagate in directions corresponding to

different diffraction orders. This is illustrated in Figure 6 in which the propagation direction is indicated for the orders m = 1, 0 and -1.

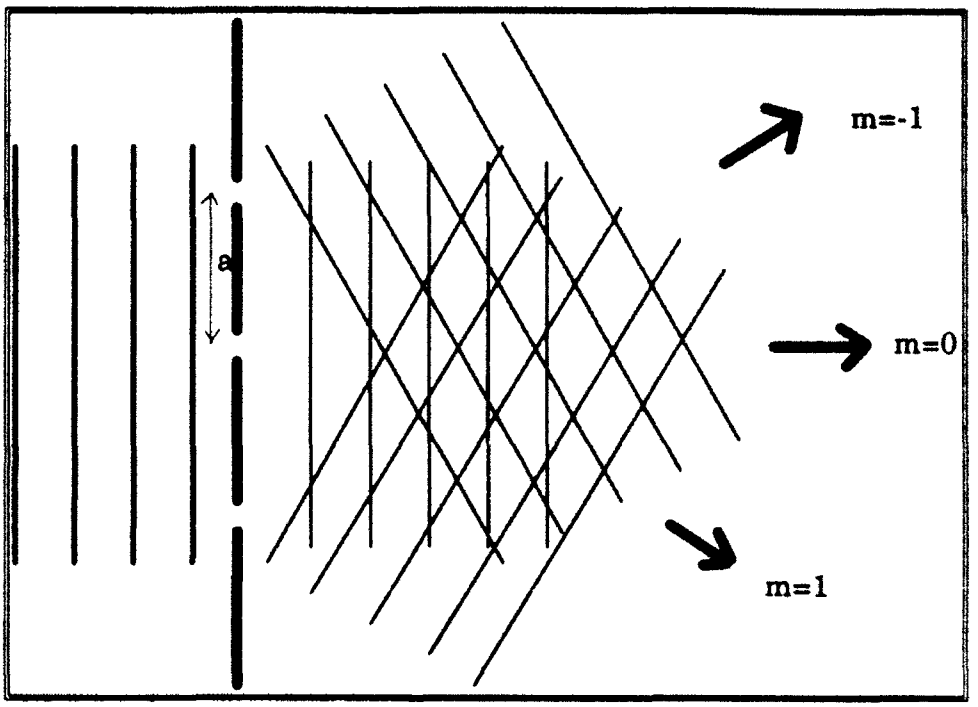

Figure 6 Multiple-Slit Diffraction

The grating equation describes the relationships in Figure 6,

$$m\lambda = a \sin \theta_d \quad , \tag{10}$$

where m is the order, λ is the wavelength, a is the distance between the center of the apertures, and θ_d is the deflection angle of the order from grating normal. The characteristics of a transmission grating are provided by Equation 10 and Figure 6.

B. REFLECTION GRATING

A reflection grating is similar to the transmission grating, except the differences in path length are generated in the groove depth and spacing. If incident light is normal to the grating, the grating equation is the same as Equation 10. If the incident light is oblique to the grating normal, the

grating equation becomes

$$m\lambda = a(\sin\theta_i + \sin\theta_d) \quad , \tag{11}$$

where the incident angle (θ_i) and diffraction angle (θ_d) are measured clockwise from the grating normal. Figure 7 illustrates the reflected orders off of a grating with oblique incidence.

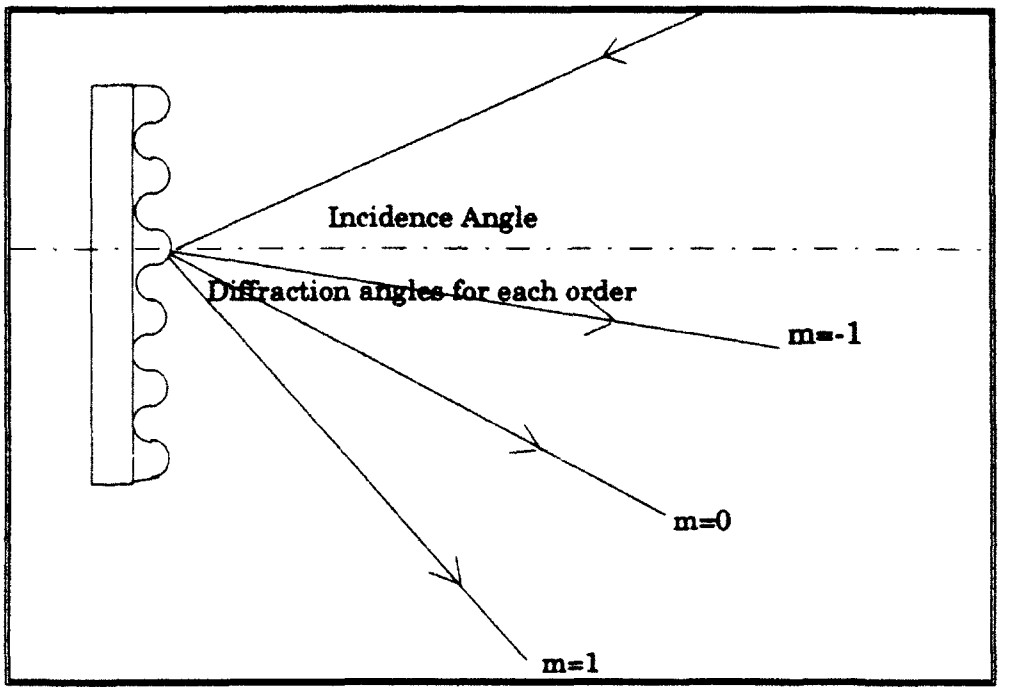

Figure 7 Reflection Grating With Oblique Incidence

C. INTERFEROMETRIC DEVICES

1. All-reflection Interferometer

The emissions of interest in this thesis fall into the EUV and FUV portion of the spectrum. Interferometers require the use of reflective optics due to the opacity of materials for wavelengths in this region. Several all-reflection interferometers using diffraction gratings as beam splitters have been built and evaluated (Roesler and Harlander, 1990; Fonck et al., 1978; Kruger et al., 1972; Kruger et al., 1973). In the design of a FUV and EUV instrument, consideration must be given to minimize the number of reflections that occur for each path due to the reduction in

intensity at each reflection. The optimization of the throughput of the instrument is particularly important due to the low reflectivity in the EUV/FUV region.

A detailed discussion on the development and design of the spherical grating interferometer designed at NPS, can be found in the thesis by Nichols (1990). The spherical grating design is based on the Rowland Circle Mount spectrometer. A general layout of the spherical grating interferometer and the basic principles are presented in this section as background.

The Rowland circle has a diameter equal to the radius of curvature of the spherical grating. The optical characteristics are such that light emanating from a point source on the Rowland circle diffracts off of the spherical grating and focuses back onto the Rowland circle. Light at different wavelengths would focus at different positions along the detector. A diagram of the Rowland Circle Mount is shown in Figure 8. The spherical grating model extends this into another dimension.

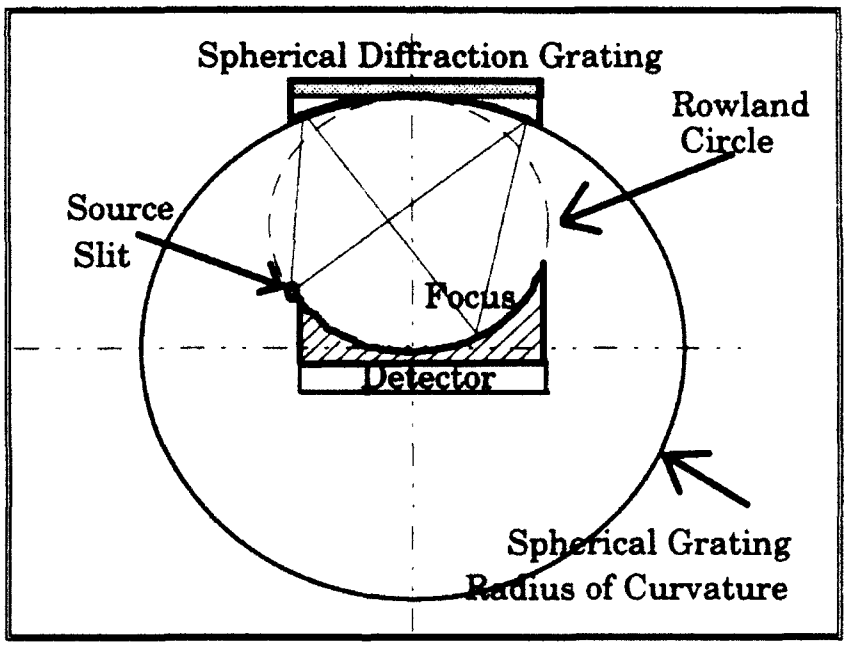

Figure 8 Rowland Circle Mount

2. Modified Michelson Interferometer

The Michelson interferometer is probably the most notable interferometric device. The conventional Michelson interferometer, shown in Figure 9, is an amplitude-splitting interferometer.

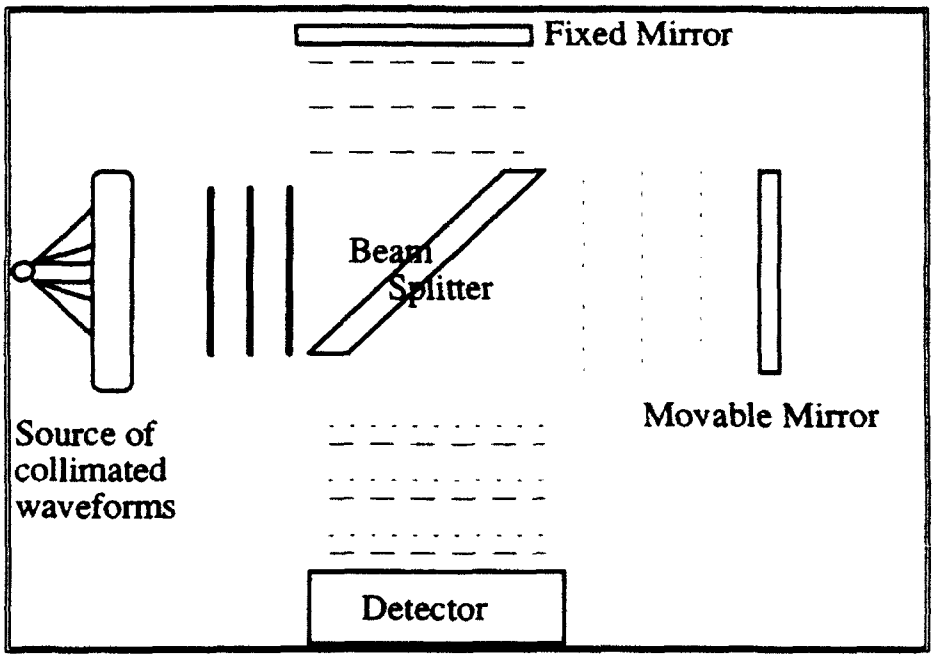

Figure 9 Conventional Michelson Interferometer

Collimated light illuminates the beam splitter, which is simply a partially silvered mirror. From this position, the beam continues to travel as a plane wave but splits into two directions: One direction toward the fixed mirror and the other toward the movable mirror. Reflection occurs off of both of the mirrors, and the plane waves recombine at the beam splitter with a portion of the recombined plane waves falling upon the detector. If the optical path lengths of the two paths are the same, the result is constructive interference at the detector. The movable mirror drives the interference characteristics with the irradiance varying from bright (constructive interference) to dark (destructive interference) to bright again as the movable mirror traverses one-half wavelength.

This mirror scan and the mirrors themselves can be eliminated by the introduction of a diffraction grating, a wavelength dependent optical element. Recall that for a given diffraction grating, the direction that wave fronts proceed after diffraction depends upon the radiation wavelength, order and incidence angle (see Equation 11). This wavelength dependence provides interesting characteristics for the interferometer. If the mirrors on the Michelson interferometer are replaced with properly oriented diffraction gratings, as in Figure 10 below, a reflected wave front can be returned to the beam splitter in a fashion similar to the conventional Michelson interferometer. To reflect the incident beam directly back to the beam splitter, the angle θ must equal to one of the diffraction angles (θ_d).

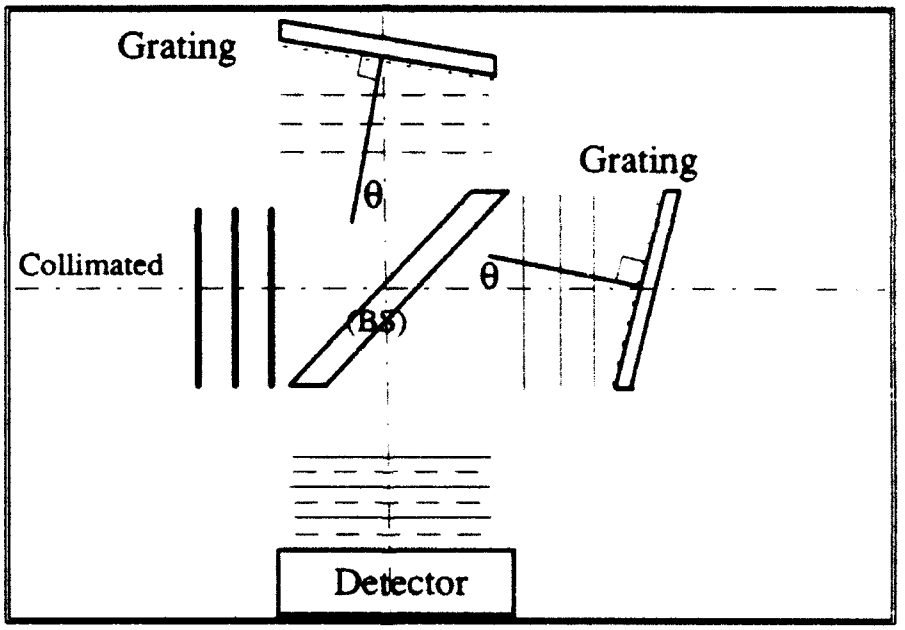

Figure 10 Modified Michelson Interferometer with Gratings

Suppose the gratings are positioned such that the minus one diffraction angle is equal to the incident angle. The device is "tuned" to a particular wavelength of light, denoted by λ_o, by first making the optical path distances the same for each path, and, second, by rotating both gratings to the angle θ described above. From this "tuned" λ_o position, the input wavelength is determined

by the spatial fringe pattern on the position detector. The spatial pattern is a function of the difference in wavelength from λ_o. In order to better visualize the operation of the device and the characteristics of the interference, assume plane waves of wavelength $\lambda = \lambda_o + \Delta\lambda$ are input into the device. According to the grating equation, the first order will reflect off of the grating at an angle equal to the sum of θ and some difference angle $\Delta\theta$ due to the $\Delta\lambda$. These in turn creates plane waves that recombine at the beam splitter with the same difference angle $\Delta\theta$, thus creating interference fringes at the overlap points. Figures 11 and 12 illustrate the principles of operation.

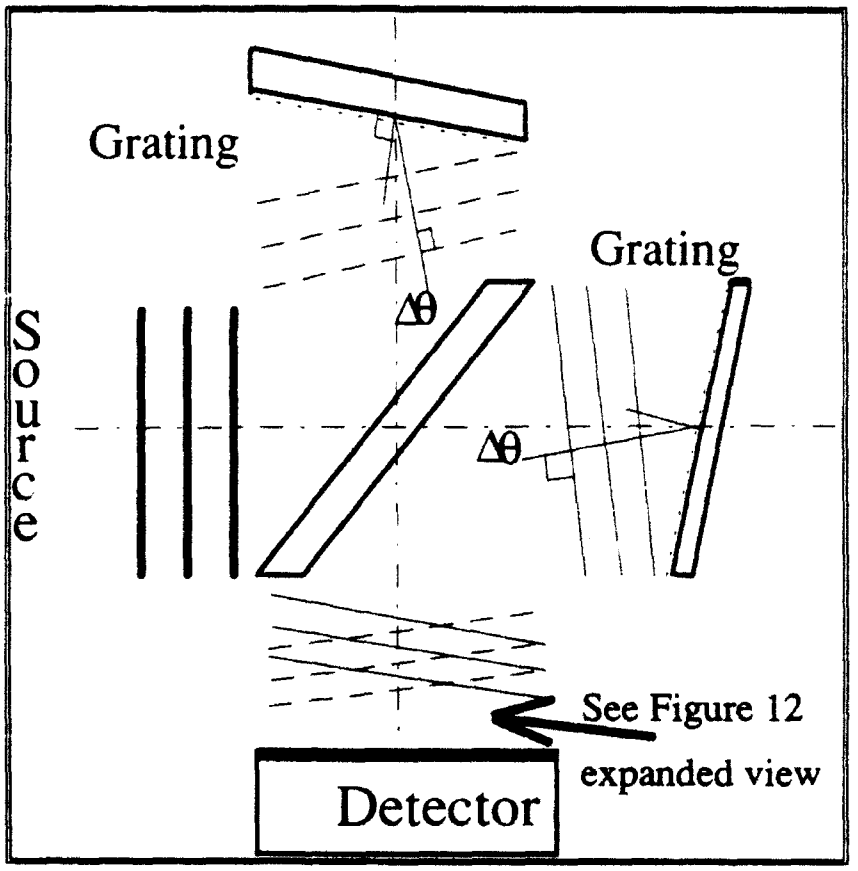

Figure 11 Michelson Interferometer Modified with Rotated Gratings

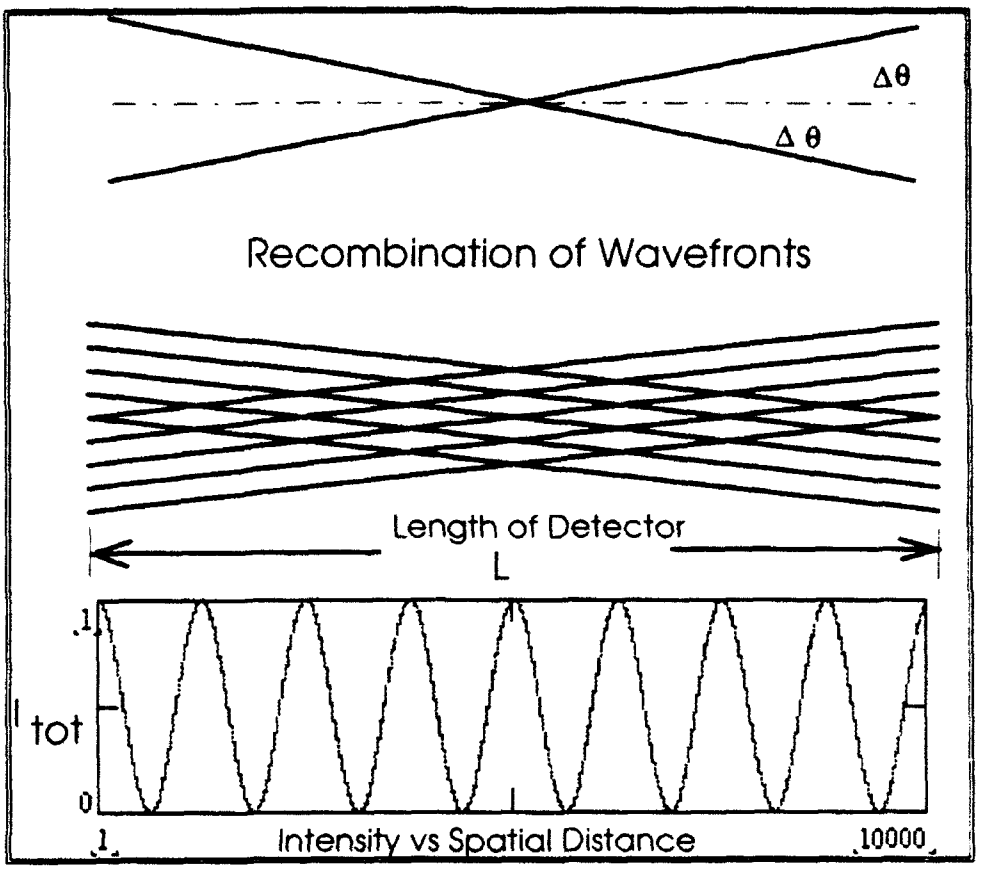

Figure 12 Expanded View of Interference at Detector with Normalized Intensity Plot

The Fourier Transform of the pattern in Figure 12 would be a delta function corresponding to the spatial frequency of the interference pattern. This spatial frequency of this pattern is directly proportional to $\Delta\lambda$. This is termed "spatial heterodyning" since the reference point on a spatial frequency scale is not zero, as it would be on a scanning interferometer. Instead, the reference point corresponds to the "tuned" λ_0 wavelength condition.

To develop the details of this interferometer further, consider the grating equation for off-axis incident rays,

$$\frac{m}{a}\lambda = \sin\theta_i + \sin\theta_d \quad , \tag{12}$$

where **m** is the order, **a** is the spacing between lines on the grating, θ_i is the incidence angle and θ_d

is the angle of the m^{th} diffraction order. Assuming first order ($m = 1$), the "tuned" condition for λ_o is specified by setting the incident angle equal to the diffraction angle ($\theta_i = \theta_d = \theta$). Equation (12) can then be rewritten as

$$\sin(\theta) = \frac{\lambda_o}{2a} \quad , \tag{13}$$

which provides the grating angle for the tuned wavelength condition.

With the reference condition satisfied, the grating equation is manipulated to solve for the relationship between changes in wavelength and changes in angle. For very small incremental changes, the derivative of the grating equation (Equation 11) becomes

$$\Delta\lambda = a\cos(\theta)\Delta\theta \quad . \tag{14}$$

where m has been set to one.

By performing trigonometric identity substitution for the cosine term and then substituting Equation (13) for the resulting sine term, this equation may be rewritten as

$$\Delta\lambda = a\Delta\theta\sqrt{1 - \sin^2(\theta)} = a\Delta\theta\sqrt{1 - (\frac{\lambda_o}{2a})^2} \quad . \tag{15}$$

Equation (15) holds for any value of $\Delta\lambda$. In order to determine the minimum resolvable change in wavelength ($\Delta\lambda_{min}$) for the instrument, the details of the instrument need to be considered. Specifically, the length of the detector determines the limit of resolution.

Consider the sinusoidal pattern shown in Figure 12. A lower spatial frequency would elongate the pattern, spreading the intensity points along the detector. The limit of resolution would be obtained when a total of only two maximum (or minimum) intensity points remain on the detector (located at opposite ends). The smallest angular difference between the wave fronts that provide such an intensity maximum (or minimum) at each end of the detector defines the limit of resolution of the instrument. A variation of Figure 12 is provided in Figure 13, which illustrates this principle.

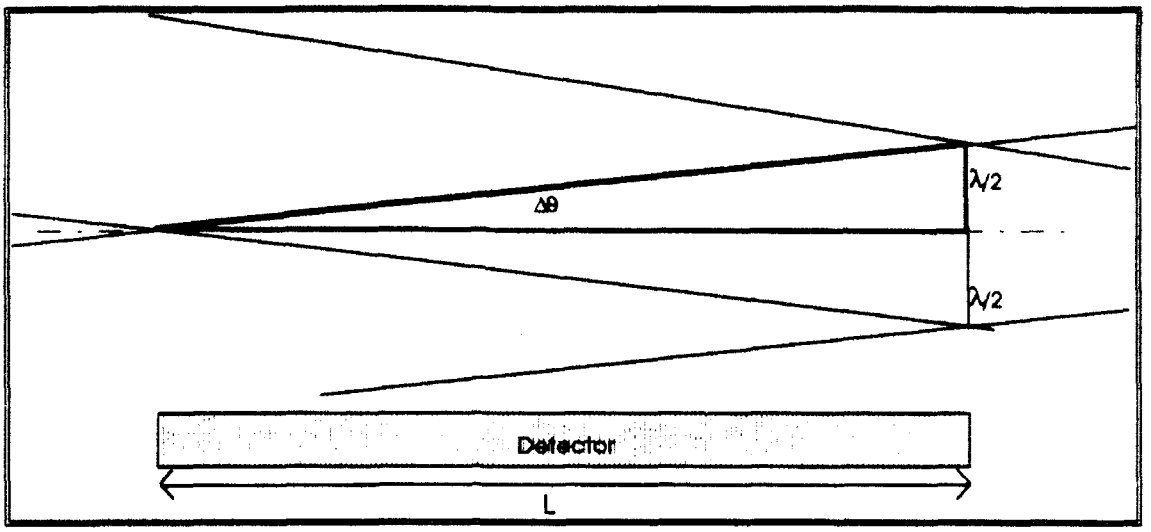

Figure 13 Interference and Detector Length Relationship for Resolution Limit

With a small angle approximation, Figure 13 reveals the angle $\Delta\theta$ can be specified as

$$\frac{\lambda_o/2}{L} = \tan(\Delta\theta) \approx \Delta\theta \quad . \tag{16}$$

From this angular relationship, Equation (15) can now be rewritten to provide the equation for the limit of resolution for the instrument,

$$\Delta\lambda_{min} = \frac{\lambda_o}{2L}\sqrt{a^2 - (\frac{\lambda_o}{2})^2} \quad . \tag{17}$$

D. SPECTRAL LINE BROADENING

Basic theory on the mechanisms of line broadening is presented to establish the reasoning behind the requirement for a high resolution interferometer. There are several factors that account for observed spectral line widths other than instrument characteristics alone. There are primarily three mechanisms that cause broadening. These three mechanisms are discussed briefly, and a more detailed description can be found in Webb (1969) or Mihalas (1978).

The first broadening mechanism is natural line broadening. Natural line width is directly proportional to the Einstein A-coefficient, which is inversely proportional to the lifetime of the transition between quantum levels of atoms. Transitions that take on the order of a second have a

very narrow natural line width, whereby transitions with lifetimes of 10^{-8} seconds would have a broad natural line width. The profile of the line width is Lorentzian in shape. The uncertainty principle may be used to describe the relationship between energy and lifetime,

$$\Delta E \Delta t \geq h \quad , \tag{18}$$

where ΔE is the uncertainty of the energy level, Δt is the lifetime and h is Planck's constant. From this, the uncertainty in frequency ($\Delta \nu$) can be expressed by

$$\Delta E = h \Delta \nu \quad . \tag{19}$$

Pressure or collision broadening is the interruption of an emission wave train by collisions with other atoms. The Heisenberg uncertainty principle (Equation 18) is called upon again to provide the relationship. When a collision shortens the wave train, Δt decreases, therefore ΔE must increase, causing the spectral broadening of $\Delta \nu$.

Atoms experience a random motion or thermal activity, which can create doppler shifts dependent upon whether the motion is toward or away from an observer. The result is Doppler broadening, which has a Gaussian line shape. Line width for a typical Doppler broadened emission is on the order one hundredth of an angstrom. The relationship between temperature and the Doppler width of the spectral is given by

$$\Delta \nu_{Doppler} = \frac{\nu_o}{c} \sqrt{\frac{2kT}{M}} \quad , \tag{20}$$

where $\Delta \nu$ is the thermal Doppler width of the line, ν_0 is the line center frequency, c is the speed of light, k is Boltzmann's constant, T is the temperature and M is the atomic mass. Figure 14 illustrates the principles of Doppler broadening.

All of these broadening mechanisms contribute to the line width of an emission line. The relative importance of one mechanism with respect to another depends on temperature, pressure, and the lifetime of the state. Natural line broadening is inherently small, and the low pressures in

the ionosphere result in pressure broadening contributions that are significantly less than the dominant Doppler broadening.

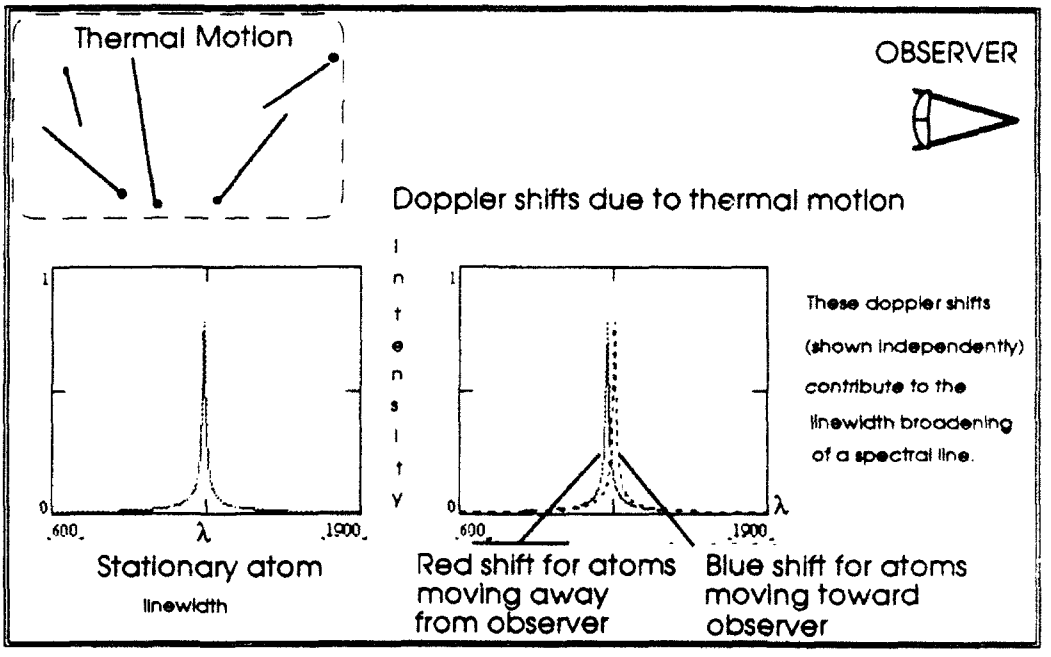

Figure 14 Doppler Line Broadening

Having presented the fundamentals of the various broadening mechanisms, we can now understand the importance of extremely high resolution spectroscopy. For example, by observing a Doppler broadened emission line with sufficient resolution, one can infer the kinetic temperature of the atmosphere. In addition, by directly observing spectral line profiles, it is expected that more accurate atmospheric density profiles can be obtained using fewer assumptions.

IV. SPHERICAL GRATING INTERFEROMETER

This chapter describes the procedures used ray trace the spherical grating interferometer. The ray trace results are also presented and discussed. A more detailed background on the development of the spherical grating interferometer is presented in the thesis by Nichols (1990). A brief overview of the layout is presented herein.

A. SPHERICAL GRATING INTERFEROMETER DESCRIPTION

The design of the spherical grating was based on the Rowland Circle Mount spectrometer. Figures 15 and 16 illustrate the spherical grating interferometer model. In this design, a single grating is used to split the incident beam and recombine the reflected beams for the interference pattern. The upper mirrors in the figures were positioned to reflect the beams back toward the spherical grating for recombination. These recombined beams produced the interference fringes at the detector.

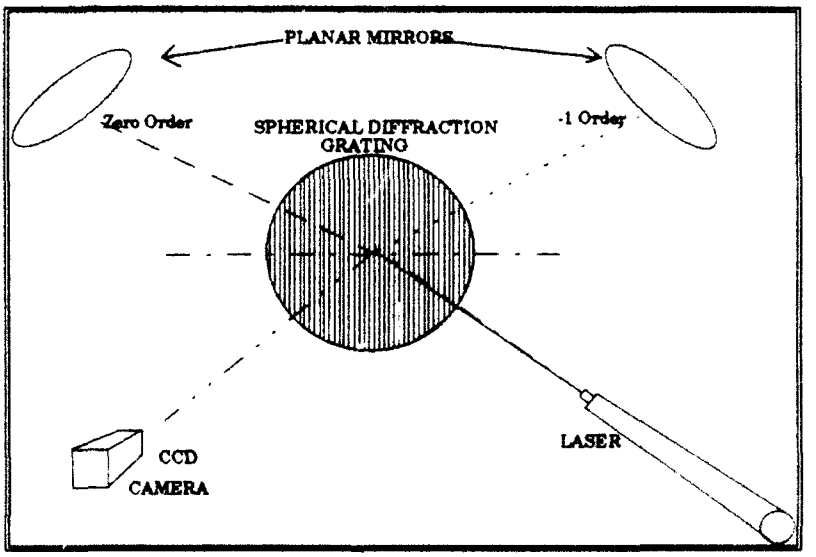

Figure 15 Spherical Grating Model (View From Grating Normal)

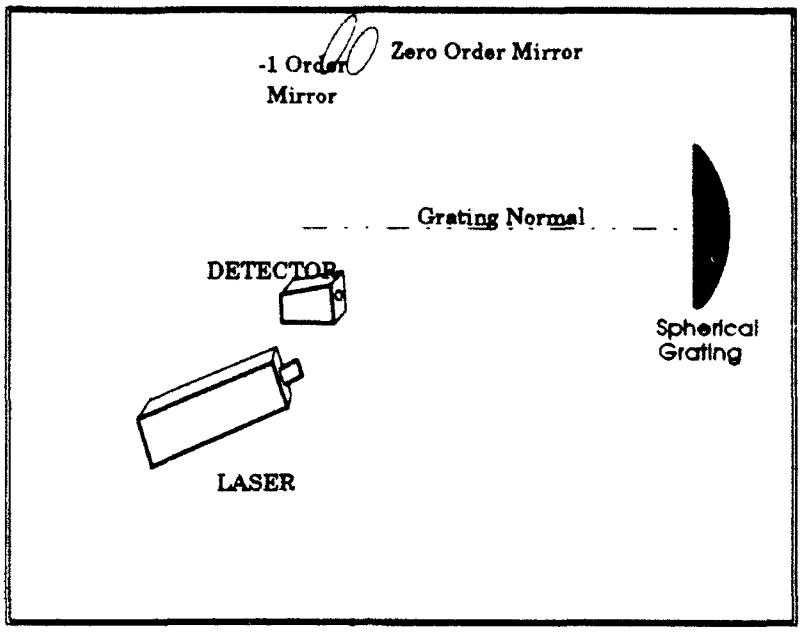

Figure 16 Spherical Grating Model (Side View)

The holographic grating used in the model has a ruling density of 1200 lines per mm and a radius of curvature of 20.14 cm. The flat circular mirrors are one inch in diameter. The light source is a green helium neon (He-Ne) laser that operates at a wavelength of λ = 5435 Å and is fitted with a beam expander. The detector is a charge-coupled device (CCD) imager that is connected to a black and white monitor.

In order to maintain equal path lengths, an out-of-plane design was selected such that the incidence angle was equal to the diffraction angle of the minus one order. The resulting configuration placed the mirrors directly over the source and detector ray paths.

B. BEAM FOUR RAY TRACING PROCEDURES

Ray tracing was performed to determine the optimal optical element configurations and locations required to produce an interference fringe pattern suitable for inversion. Initial ray tracing of the spherical grating interferometer was conducted using a simplified two--dimensional

model similar to Figure 17. While this configuration can be modeled using the ray trace program, the model cannot be physically constructed due to the obstruction of the ray path by the optical elements located on the same axes.

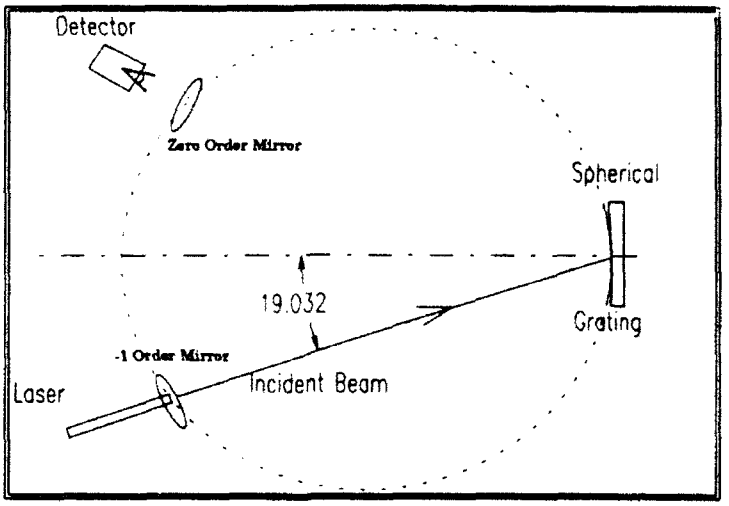

Figure 17 Two-Dimensional Spherical Grating Diagram (overhead view)

Figure 18 illustrates the ray paths for the spherical grating interferometer. The expanding beam from the laser source is collected and diffracted off of the spherical grating (Figure 18a). The divided beams are directed toward two mirrors (Figure 18b). The mirrors then reflect the rays back to the spherical grating for recombination (Figure 18c). The CCD detector senses the interference pattern due to the ray recombination (Figure 18d). In order to model the beam splitting at the grating, two separate runs of the ray trace code were required. The files with "Zero Order" in the title trace the zero order path off of the initial grating diffraction. The "One Order" files trace the first negative order path off of the initial grating diffraction. The dimensions of the two-dimensional model used for the tracing are illustrated in Figure 19.

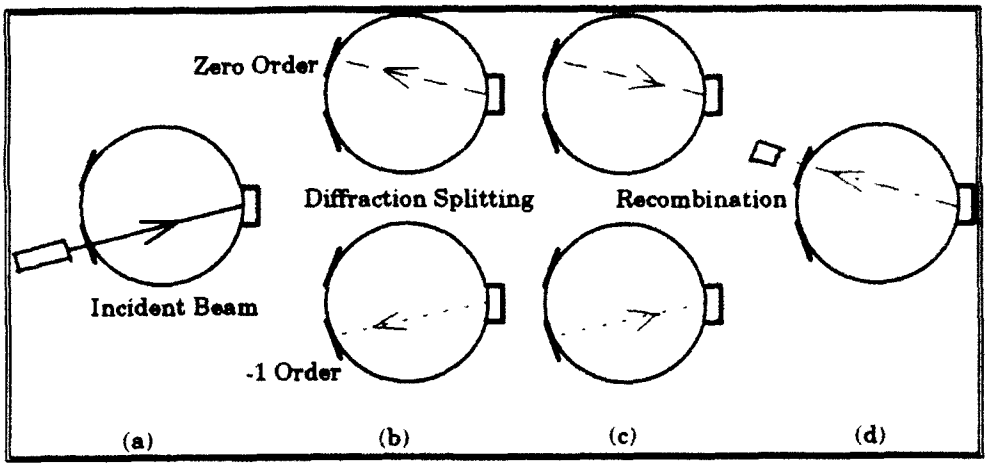

Figure 18 2-D Ray Path For Spherical Grating Interferometer

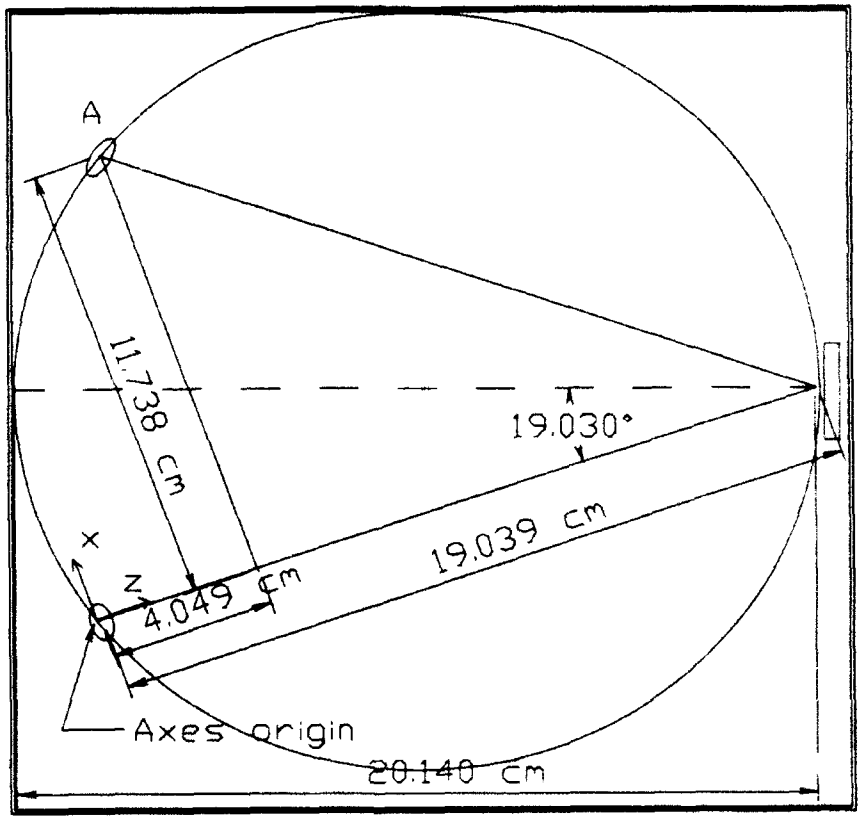

Figure 19 2-D Spherical Grating Dimensions

The RAY file consisted of 21 rays that specify the spread and the maximum span of the source ray cone (± 2°). Two perpendicular fan beams were created for the runs to facilitate the analysis of the sagittal and tangential focal planes. Alignment of the elements was verified by observing the position of the central or chief ray. This single ray was tagged with a green color in the RAY files.

The RAY and OPTICS (OPT) files for the ray tracing are contained in Appendices A and B. These data files list the source and optical element parameters respectively. Tables 1 and 2 define the column headings on the data files.

TABLE 1

COLUMN HEADERS FOR BEAM FOUR OPTICS FILE

Header	Description
Mir,Grat,I,Det	Mirror, Grating, Iris, Detector, element type or identity
Xv,Yv,Zv	Vertex coordinates of the element
Tilt	Element rotation in degrees around X axis
Pitch	Element rotation in degrees around Y axis
Roll	Element rotation in degrees around Z axis
Shape	1-(eccentricity)^2:ellipse, 0 = paraboloid,1 = sphere
Curv	Curvature=1/(radius of curvature of element), flat = 0
Cx	Toric surface curvature (along x axis)
Diam	Outside diameter of optic or iris
Ord	Desired order of diffraction for ray trace
Gx	Diffraction grating ruling density in x (lines/μm)

TABLE 2

COLUMN HEADERS FOR BEAM FOUR RAY FILES

Header	Description
X0,Y0,Z0	Global coordinates for source of ray
U0,V0,W0	Direction cosines for ray start
@wavelen	Wavelength (μm) of light
xg,yg,zg	Local coordinate system goal for final ray landing
Xf,Yf,Zf	Global coordinate for final ray landing
Note	Provides surface element number of ray finish after run

To observe the spatial relationship of the rays landing on the detector, an output format created by the PLOT command was used. The PLOT command provides a two-dimensional spot diagram of ray intersection points on the detector screen. More rays could be observed by the use of the RANDOM command. This command would generate randomly-spaced rays to fill the spot diagram with extra rays confined within the fan limits established by the RAY file. BEAM FOUR also calculated a root mean square (RMS) distribution or standard deviation of the ray scatter from the mean position on the detector. This parameter provides a quantitative measure of the quality of the focusing or image sharpness on the detector.

Ray tracing with BEAM FOUR generates the spot diagrams for various detector positions. The detector was placed on the Rowland Circle for the initial runs. Thereafter, the AUTOADJUST feature was used to determine the tangential, sagittal and circle of least confusion detector positions. The desired AUTOADJUST parameter was "flagged" in the OPTICS file by placing a question mark (?) in the detector Z position column. The xgoal and ygoal columns in the RAY file constrained the final ray landing position along the specified axes. By listing a very

small number in either the xgoal, ygoal or both columns, the tangential, sagittal and circle of least confusion positions were solved for respectively by the AUTOADJUST feature. The data files for the detector positioning runs are located in Appendix A.

The LAYOUT command in BEAM FOUR generates a pictorial display of the ray trace model and is presented in Figure 20. The detector is located on the Rowland circle in the lower portion of the figure. The source and first order mirror are co-located in the upper left portion of the figure. The spherical grating is the element on the right.

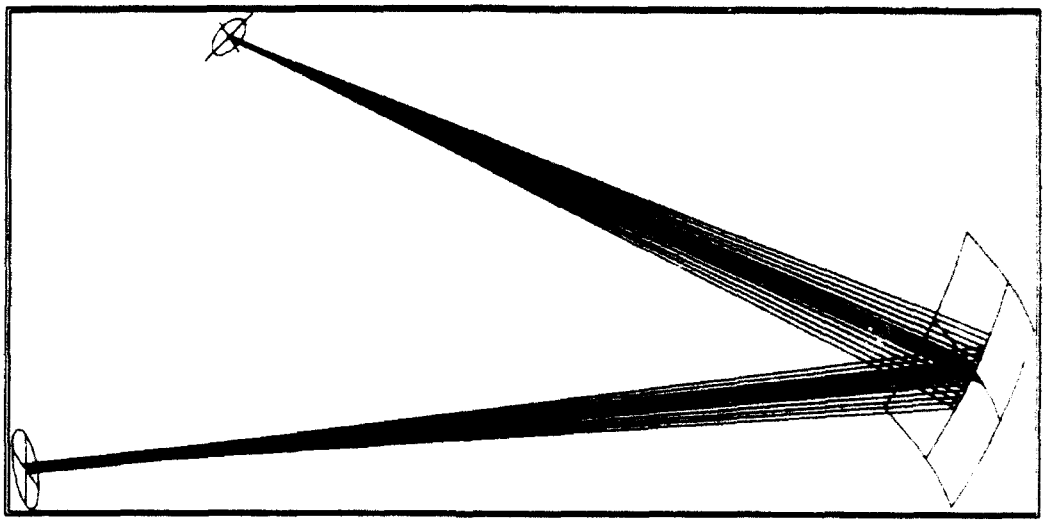

Figure 20 Ray Trace of Spherical Grating Model (Detector on Rowland Circle)

On the quest to obtain a suitable interference pattern, one possible solution was to evaluate the use of an anamorphic or compound aspheric surface to improve the performance of the instrument (Cleary et al., 1992). To investigate this, the mirrors were shaped in a manner to combine the sagittal and tangential focal planes. This design curved the mirror in only one axis, creating a cylindrical shape. The AUTOADJUST feature of BEAM FOUR was utilized in the runs to determine optimal mirror curvature (Cx) parameter. The data files for these runs are listed in Appendix B.

C. BEAM FOUR RESULTS AND DISCUSSION

Appendices A and B contain the BEAM FOUR results in the output format of data files and spot diagrams. The BEAM FOUR results are summarized in Table 3 and are discussed within this section.

TABLE 3

BEAM FOUR RESULTS SUMMARY

Description of Ray Trace	Detector Distance From Grating (cm)		RMS Deviation (cm) (based on 21 rays)	
	Zero Order	First	Zero Order	First
Detector on Rowland Circle	19.0391	19.0391	0.0007	0.0011
Tangential Focal Plane Search	19.0451	19.0458	0.0008	0.0011
Sagittal Focal Plane Search	45.6135	45.6476	0.0001	0.0001
Circle of Least Confusion	19.9545	19.9558	0.0708	0.0708
Detector Position Cyl. Mirror	19.0454	19.0451	0.0003	0.0003

1. Detector Position Ray Tracing Discussion

The detector positions were consistent between each order in the ray trace, with the maximum difference being 0.3 mm for the sagittal calculations. For the positions located near the Rowland Circle (within 20 cm of the detector), the error was approximately 1/100 of a mm, well below the positioning error estimate of 1 mm for placement of the physical optics. With the long coherence length of the visible laser source used in the laboratory test, the positioning error was even less critical for optical path length considerations.

The circle of least confusion and tangential focal planes were very near the Rowland Circle as observed in the physical model and as anticipated theoretically. The Rowland Circle spot diagrams (Figures 32 and 33) looked very similar to the tangential diagrams (Figures 34 and 35) as

anticipated. Figures 34 through 41 illustrate the results for each axes collapsing to a focal point for the tangential and sagittal focal planes, and a broadened pattern for the circle of least confusion. The results were as expected.

At first glance, it may appear that choosing the tangential or sagittal focal planes would provide a symmetric spot pattern from which favorable wave fronts could emanate. By moving the detector out of plane as in the physical model, the tangential and sagittal lines rotate away from each other forming an X shape. Interference occurs only at the intersection resulting in the non-circular and non-linear patterns fringe patterns observed in the physical model. The additional aberration and astigmatism effects caused from moving the detector (and source) out of plane makes simple positioning of the detector an unlikely solution to obtaining a suitable spot pattern.

The next approach was to try and make all of the ray paths focus to a single point. These results are presented in Appendix B. By curving the mirrors along the axes that lay in the same plane as the sagittal line and not changing the mirror in the axes for the tangential rays, the two planes could be overlapped. The shape of the mirrors were cylindrical, curving in only the one axis that focused the sagittal plane. The AUTOADJUST iteration placed the detector on the tangential focal plane as desired and calculated a radius of curvature for the concave mirrors to be 5.128 cm (the inverse of the Cx parameter).

The Figure 42 through 45 spot diagrams illustrate a very small focus area for the cylindrical mirror runs. Although this configuration generated the smallest focus for all of the spherical grating runs, it is obvious in the multiple ray diagram that the spherical aberration and astigmatism effects continue to shape the spot diagram into unsuitable patterns. As in the previous case, further aberrations would occur as the detector was moved out of the two-dimensional plane. Therefore, the runs did not achieve a circular symmetric or other suitable pattern as was hoped, and other methods of shaping the spot diagram were investigated.

2. Other Modifications

In an attempt to obtain a circular symmetric or reasonable spot pattern, an elliptical grating was considered. Figure 21 illustrates the unique characteristic of an elliptical reflector whereby rays emanating from one foci are focused at the conjugate foci.

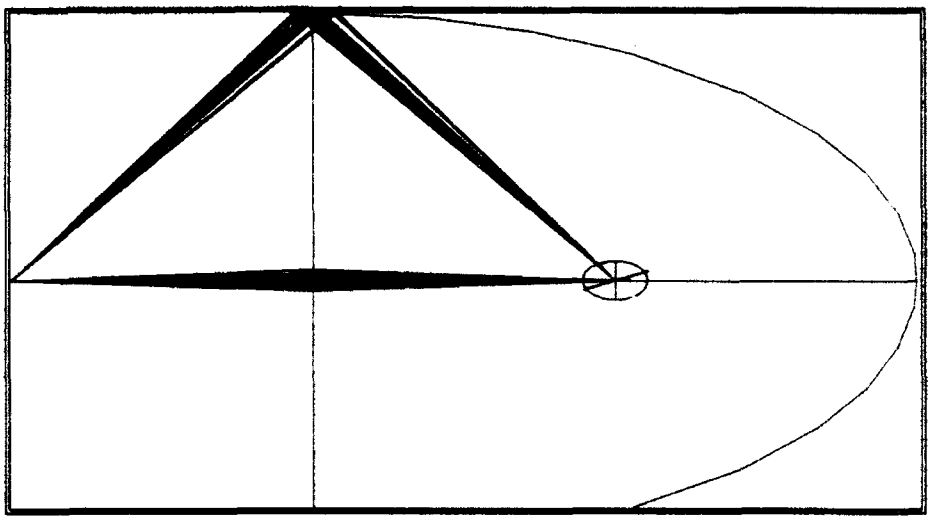

Figure 21 Elliptical Mirror Characteristics

There were two significant drawbacks to this design however that changed the direction of the investigation after only a brief analysis. First, although the focus may be acceptable in the two-dimensional model, it is anticipated that off-axis illumination (away from the centerline of the ellipsoid) would cause aberrations more severe than a spherical model. The second and most important reason for discontinuing further investigation was the cost factor. Although there are a great many prolate (end section) ellipsoidal reflectors on the commercial market, oblate (middle section) elements are more difficult obtain. Manufacturing a grating on such an element was cost prohibitive, especially for a device that would be optimized to observe just one particular wavelength.

D. SPHERICAL GRATING INTERFERENCE WITH DART PROCEDURES

The DART program was used to model the interference pattern characteristics in the spherical grating model. The accuracy of the interference patterns generated by DART is unknown as the program had not been validated at the time of this writing. With this in mind, the runs were made to provide a cursory comparison of the DART results with the physical model observations.

DART uses a Graphical User Interface to simplify data entry. The contents of the input data was similar to BEAM FOUR. The input parameters consisted of the optical element description, position, orientation and source characteristics. The origin of the coordinate system was placed at the source with the Z-axis aligned along the axis of ray centerline.

The program code used an interference module to calculate the path length differences between two ray paths. Two separate runs were required to trace the individual sequences of diffraction orders for this model. The interference module compared the separate path lengths from the same ray source in the two runs. The interference output is in the form of a two-dimensional plot displaying complete constructive interference with a black pixel, complete destructive interference with a white pixel, and over 200 various shades of gray for interim values.

The display of the interference pattern was enhanced by running the SCATTER feature on DART. This feature created a pseudo-random source of rays confined within designated parameters. The pseudo-random code was repeatable for the alternate ray path run in order to determine interference calculations. The SCATTER command smoothed the interference pattern by eliminating the regularly shaped matrix input of rays. This had the effect of removing any moiré patterns from the interference display.

After performing the ray tracing for the laser source wavelength (5435 Å), it was decided to view the interference characteristics with small incremental changes of wavelength. Wavelength

changes of +0.5, +1.0 and -0.5 Å were added to the reference wavelength of 5435 Å for the interference runs. The data files for these runs are included in Appendix C.

E. SPHERICAL GRATING INTERFERENCE RESULTS AND DISCUSSION

The interference pattern results from the spherical grating ray tracing are illustrated in Figures 46 through 49 in Appendix C. The pattern in the figures are hyperbolic in nature, similar to those observed on the laboratory model. The asymmetry may be due to position errors in the interference calculations.

The four figures show the effects of wavelength changes. The increase in wavelength created a spreading of the hyperbolic centroids and appeared to improve the symmetry. Further analysis was postponed until a validated program was available to provide more accurate interference results.

After reviewing and discussing the results of the spherical grating ray traces, it was decided that further study was warranted in the spatial heterodyning spectroscopy techniques described by other investigators (Harlender et. al., 1990). The impetus for this redirection in the investigation was the concern about the astigmatism effects of the spherical grating and the anticipated difficulty in the interpretation of the Fourier Transform from the observed non-linear interference patterns.

V. SPATIAL HETERODYNE INTERFEROMETER

A device operating in one plane with a flat grating offers the advantage of linear interference characteristics, a clear improvement over the spherical grating non-linear characteristics previously discussed. The disadvantage is the loss of light gathering and focusing effects that a spherical grating provides; the significance of which is unknown at this time. This chapter describes the procedures used in designing the prototype of a flat grating interferometer for feasibility testing with visible light. The model is hereafter referred to as the SH (Spatial Heterodyne) model. The section begins with an overview of the design concept, followed by a description of the layout, the ray tracing procedures and the DART interference results.

A. PRELIMINARY DESIGN CONCEPT OF THE SH MODEL

The transition from the spherical grating interferometer carried forward the same design constraints. Several of the design characteristics were also incorporated into the SH model. Some of these design characteristics include :

a. Only one diffraction grating is used, which eliminates the problems associated with multiple grating alignment or ruling density disparities.

b. The ruling density of the grating is optimized by eliminating the undesired diffraction orders to improve the efficiency of the instrument.

c. Contrast is optimized in the interference pattern by using equal intensity ray recombination. This was accomplished by taking one of the split ray paths through the minus one and zero order diffractions and the alternate ray path through the zero and a minus one order concurrently.

For interference to occur, the difference in optical path length between two split ray paths must remain within the coherence length of the source. In the case of the spherical grating, a

requirement was placed on the incidence angle to be equal to the minus one diffraction angle in order to maintain equal path lengths on the Rowland Circle. With a plane grating, the path lengths of split rays can be equalized without this restriction.

The grating equation for oblique incidence can be rewritten with a substitution of ruling density ($\rho = 1/a$) as

$$\rho m\lambda = (\sin\theta_i + \sin\theta_d) \quad , \tag{21}$$

where ρ is the grating ruling density (lines/mm), m is the order, λ is the wavelength, θ_i is the incidence angle, and θ_d is the diffraction angle. Figure 22 shows a typical setup with this design. The angles are measured clockwise from the grating normal as indicated in the figure (minus sign used for θ_i, θ_{-1} and θ_{-2}).

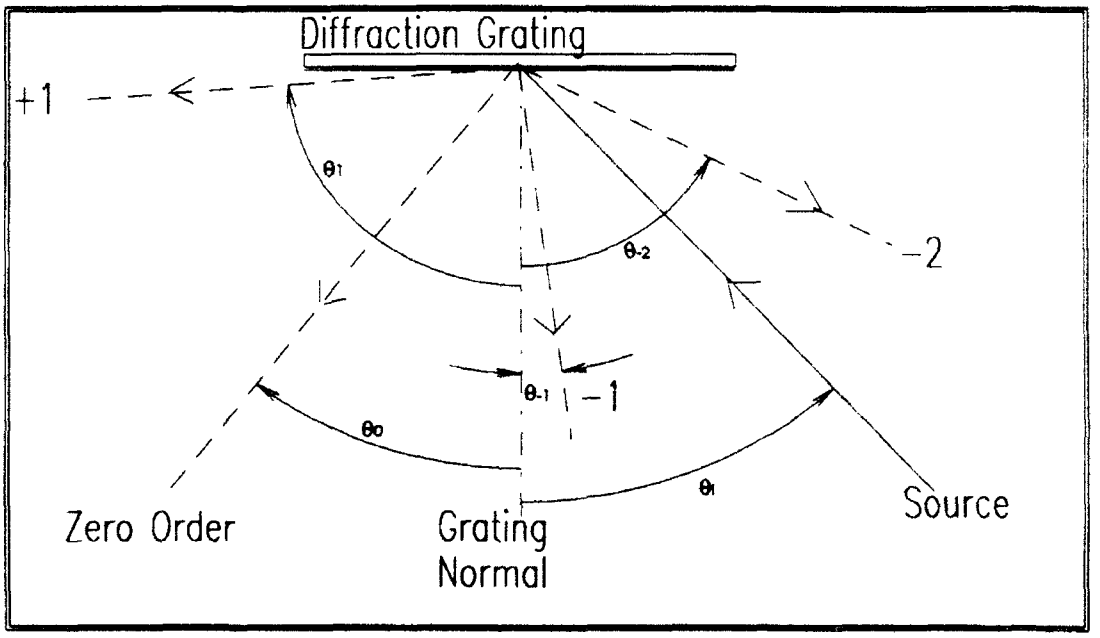

Figure 22 Plane Grating Diffraction Orders

If the incidence angle is set such that the zero and minus one order diffraction rays are used for the split ray paths, a configuration similar to the two-dimensional spherical grating model can be obtained. Figure 23 illustrates the sequence of the ray paths shown from an overhead view.

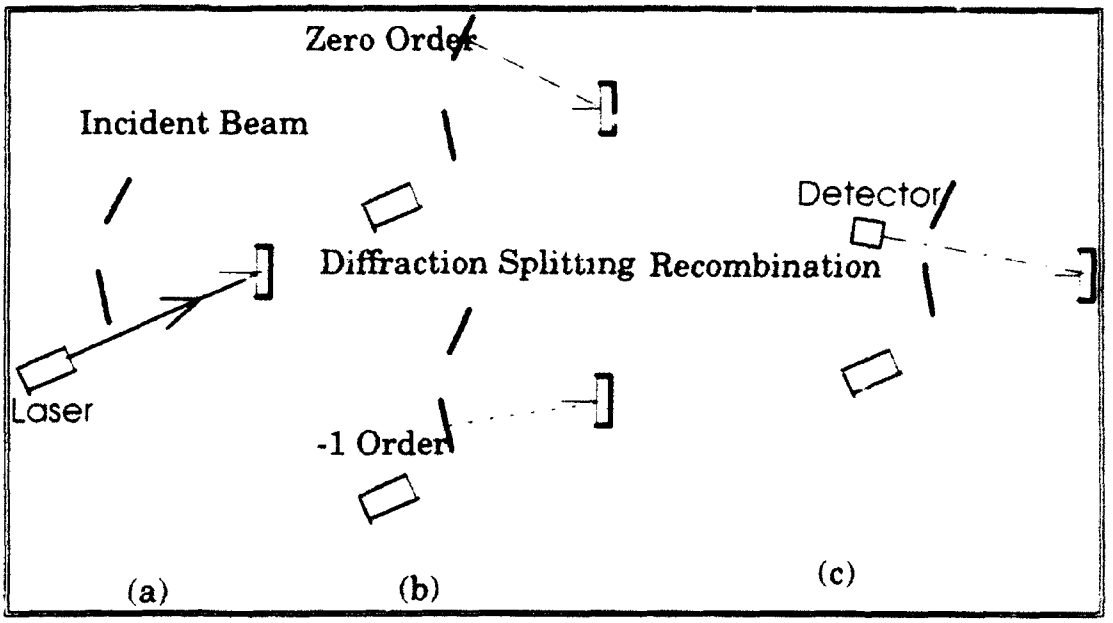

Figure 23 SH Model Ray Path Concept

In this figure, collimated light is directed toward the grating at an incidence angle that is greater than the minus one order diffraction angle (Figure 23a). The diffraction grating splits the collimated beam into different orders (Figure 23b) that are reflected from secondary mirrors. Upon diffraction, the new minus one order from the upper mirror is recombined with the new zero order from the lower mirror (Figure 23c). The recombined rays then proceed to the detector where an interference pattern is sensed.

Just as in the spherical grating model, it is desirable to eliminate the unused diffraction orders to maximize the intensity of the desired orders. This is accomplished by making the diffraction angle $\theta_d \geq 90°$ for the $m = 1$ order, and $\theta_d \leq -90°$ for the $m = -2$ order. For a given wavelength,

this is accomplished by selecting the proper grating rule density (ρ) to keep the desired orders. To determine the first condition, set $\theta_d = 90°$ and $m = 1$ in Equation 21 to get

$$\rho\lambda - 1 = \sin\theta_i \quad . \tag{22}$$

Likewise, set $\theta_d = -90°$ and m = -2 in Equation 21 to obtain

$$-2\rho\lambda + 1 = \sin\theta_i \quad . \tag{23}$$

Since the incidence angle is the same for both conditions, Equations 22 and 23 can be set equal to one another. By setting the equations equal and solving for ρ gives

$$\rho = \frac{2}{3\lambda} \quad , \tag{24}$$

which provides the grating ruling density for a given wavelength (λ), that eliminates the undesired orders.

By substituting Equation 24 into Equation 22, the incidence angle may be solved for,

$$(\frac{2}{3\lambda})\lambda - 1 = \sin\theta_i = -\frac{1}{3} \quad , \tag{25}$$

which is an incidence angle of θ_i =-19.47 °. Note that upon substitution of Equations 24 and 25 into Equation 21 and then solving for $\sin\theta_d$,

$$\frac{2}{3\lambda} m\lambda = (-\frac{1}{3} + \sin\theta_d) \quad , \tag{26}$$

$$\frac{2}{3} m + \frac{1}{3} = \sin\theta_d \quad , \tag{27}$$

the incidence angle is equal to the diffraction angle for $m = -1$. This is not desired in this model due to the obstruction of the entrance aperture axis by the minus one order mirror. Therefore, Equation 24 establishes the minimum threshold for grating density that must be exceeded to eliminate the undesirable orders. Cost factors, desired resolution, instrument and optical element dimensions determine just how much of an increase in ruling density is required. With an increased ruling density, the incidence angle may be varied to optimize configuration dimensions without exceeding the diffraction order constraints.

Table 4 provides the ruling density threshold determined by Equation 24, and the recommended commercial grating ruling density for several of the wavelengths of interest. The wavelengths include the green He-Ne laser (5435 Å) for the laboratory test, hydrogen Lyman α emissions at 1216 Å, and the atomic oxygen emission 1304 Å. Although element spacing may require a larger value of ρ for the desired layout, this table provides a guideline for establishing the minimum ruling density acceptable for optimal performance.

TABLE 4

OPTIMUM DIFFRACTION GRATING RULING DENSITY

Emission wavelength Angstroms (Å)	Threshold (lines/mm)	Commercial (lines/mm)
He-Ne Laser: 5435	1227	2400
Lyman α: 1216	5483	6000
Atomic Oxygen: 1304	5113	6000

For the prototype SHS model, a grating with ruling density of 1200 lines/mm was available for the feasibility test, hence, an extra "unused" order existed. For the laboratory test, the loss of intensity due to the unused $m = -2$ diffraction order was considered insignificant since the light source was a Class II He-Ne laser.

To determine the most suitable layout, the diffraction and displacement angles were calculated for a variety of incidence angles. The results of the calculations are shown in Table 5. The Δθ column is the angle measured from the aperture axis to the minus one diffraction order. Based on Table 5 an incidence angle of approximately -28 ° was used for the initial design. This provided reasonable clearance between the optical elements while maintaining a fairly compact total instrument design.

TABLE 5

DIFFRACTION ANGLES (DEGREES) FOR PROTOTYPE SH MODEL

θ_{apert}	-2 ord	-1 ord	0 ord	1 ord	$\Delta\theta$
-18	-84.5	-20.1	18.0	74.0	-2.4
-20	-74.2	-18.1	20.0	83.8	1.5
-22	-68.4	-16.1	22.0	none	5.3
-24	-63.9	-14.2	24.0	none	9.1
-26	-60.0	-12.3	26.0	none	12.8
-28	-56.6	-10.5	28.0	none	16.4
-30	-53.6	-8.8	30.0	none	19.9
-32	-50.8	-7.0	32.0	none	23.3
-34	-48.2	-5.3	34.0	none	26.7
-36	-45.8	-3.7	36.0	none	30.0
-38	-43.5	-2.1	38.0	none	33.2
-40	-41.4	-0.5	40.0	none	36.3
-42	-39.4	1.0	42.0	none	37.4
-44	-37.6	2.4	44.0	none	37.4

B. EXPERIMENT LAYOUT

The laser was mounted on a holder and fitted with a microscope objective lens (Sharp 20X) as a beam expander. In order to collimate the incident light, a convex lens with a 10 cm focal length was placed in the laser output beam at the focal length distance. A lens was adequate for the visible light test. An off-axis parabolic reflector would be used as the collimating element for

follow-on testing. Figure 24 is a photograph of the SH model showing the laser and lens on the right side.

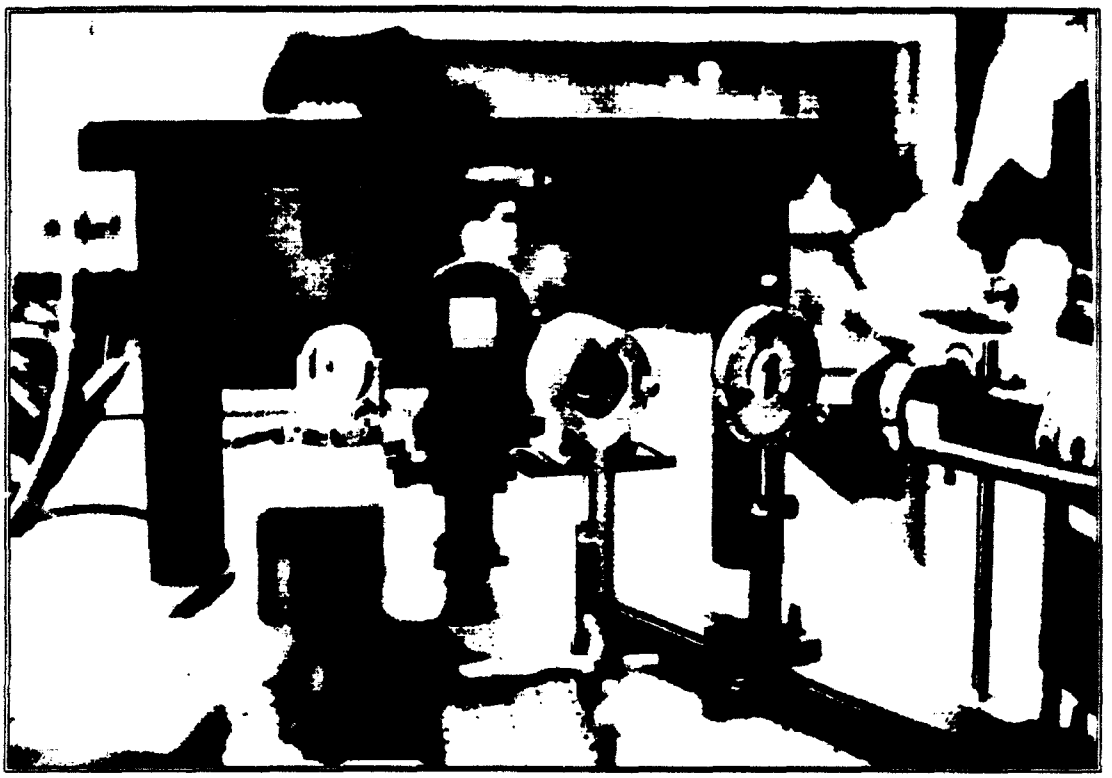

Figure 24 Photograph of Prototype Interferometer (View From Grating Normal)

A new holder was machined to mount the (50 X 50 mm) square holographic grating into the existing grating mount. The grating mount provided micrometer adjustments for the three translational axes and two rotational adjustments about the axes perpendicular to the grating normal. One-inch diameter plane mirrors on adjustable mirror mounts were used as the secondary reflectors. Micrometer adjustments could be made on the mirror mounts for two rotational axes.

A CCD camera without a lens was connected to a black-and-white monitor to display the interference patterns. Figure 25 is another photograph of the prototype SH model. From this oblique view the CCD camera and mirrors can be seen as the elements nearest the observer.

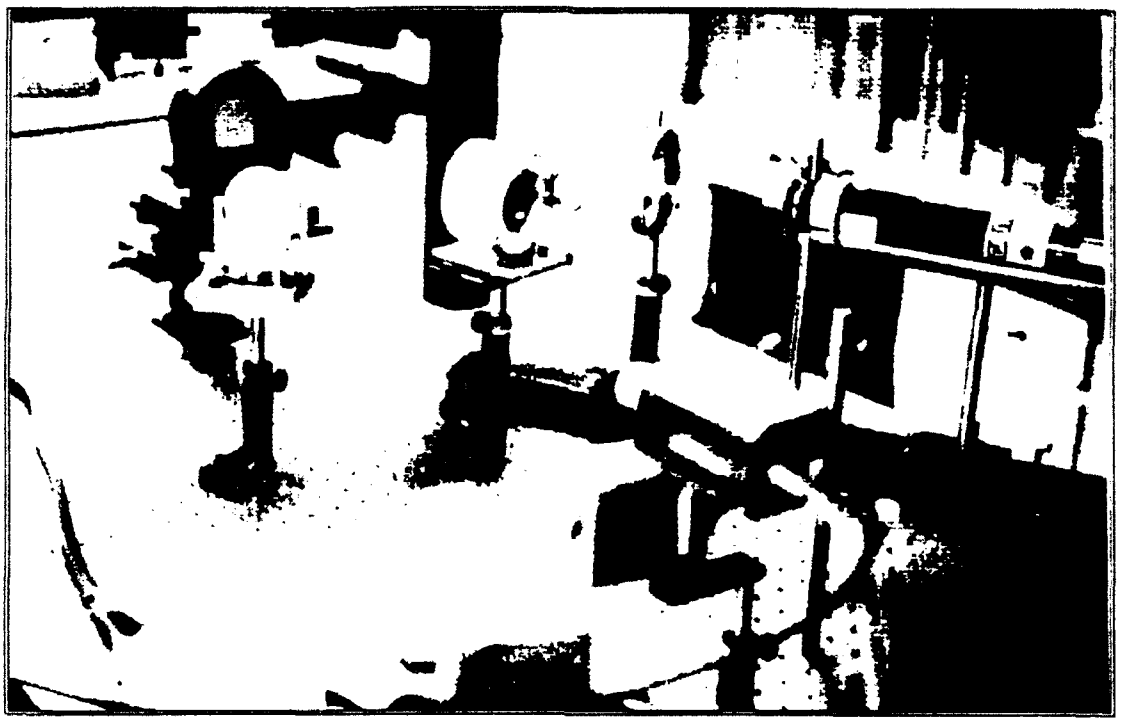

Figure 25 Oblique View of Prototype Interferometer

Initial alignment of the instrument was performed visually. First, the grating was aligned such that the grating grooves ran parallel to the vertical axes of the optics table. To do this, a laser was placed in the source holder approximately 52 cm away from the grating and at the same height as the grating center. The laser was not equipped with a beam expander. After illuminating the grating with the laser, the grating mount was rotated until all of the diffraction orders were intercepted at the same height above the optical table.

The beam expander was then placed on the laser, and the collimating lens was positioned in a lens holder approximately 10 cm in front of the beam expander aperture. The lens position was adjusted along the incident axis until the diameter of the beam was constant for several distant test points away from the lens.

The plane mirrors were placed approximately 30 cm away from the grating. The level and angle of the mirrors was visually positioned to place the diffracted beams at the mirror center

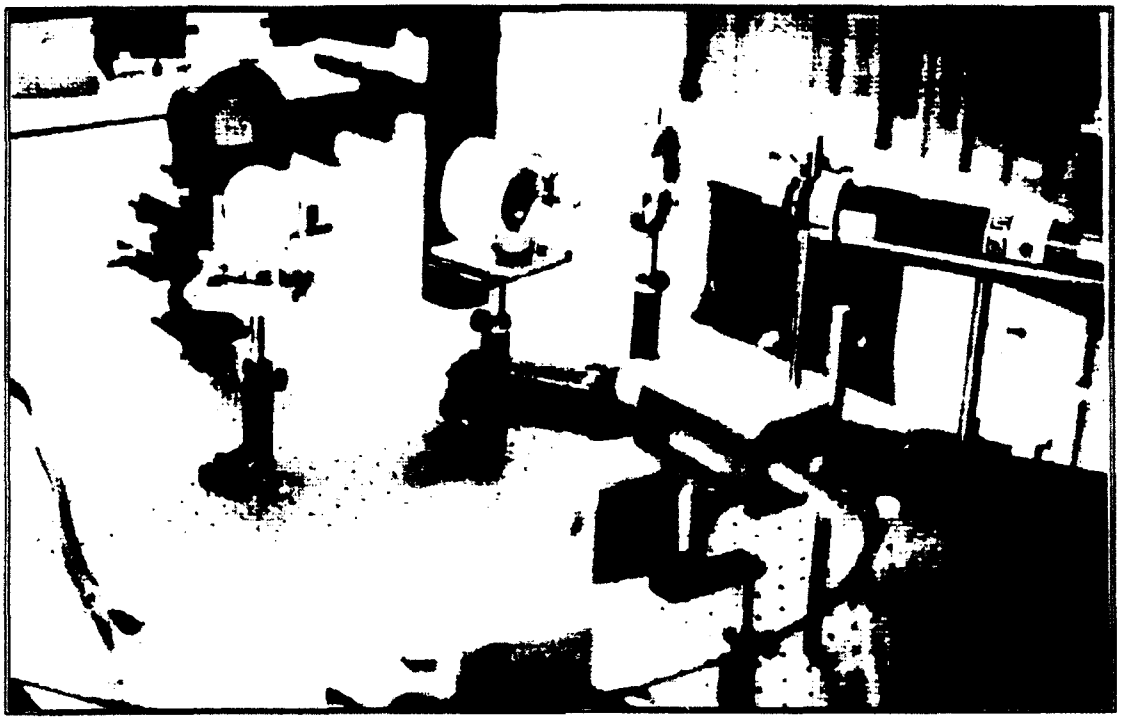

Figure 25 Oblique View of Prototype Interferometer

Initial alignment of the instrument was performed visually. First, the grating was aligned such that the grating grooves ran parallel to the vertical axes of the optics table. To do this, a laser was placed in the source holder approximately 52 cm away from the grating and at the same height as the grating center. The laser was not equipped with a beam expander. After illuminating the grating with the laser, the grating mount was rotated until all of the diffraction orders were intercepted at the same height above the optical table.

The beam expander was then placed on the laser, and the collimating lens was positioned in a lens holder approximately 10 cm in front of the beam expander aperture. The lens position was adjusted along the incident axis until the diameter of the beam was constant for several distant test points away from the lens.

The plane mirrors were placed approximately 30 cm away from the grating. The level and angle of the mirrors was visually positioned to place the diffracted beams at the mirror center

Figure 27 is a diagram showing the dimensions and layout of the SH model. Because the beams are collimated, the distances from the grating to the detector and source could be reduced to make the entire instrument more compact for a space vehicle payload. The mirror distances could be reduced also, but it is important to maintain equivalent distances for these two elements in order to stay within one coherence length of the radiation source. For the laboratory laser, this parameter was not as critical due to the long coherence length.

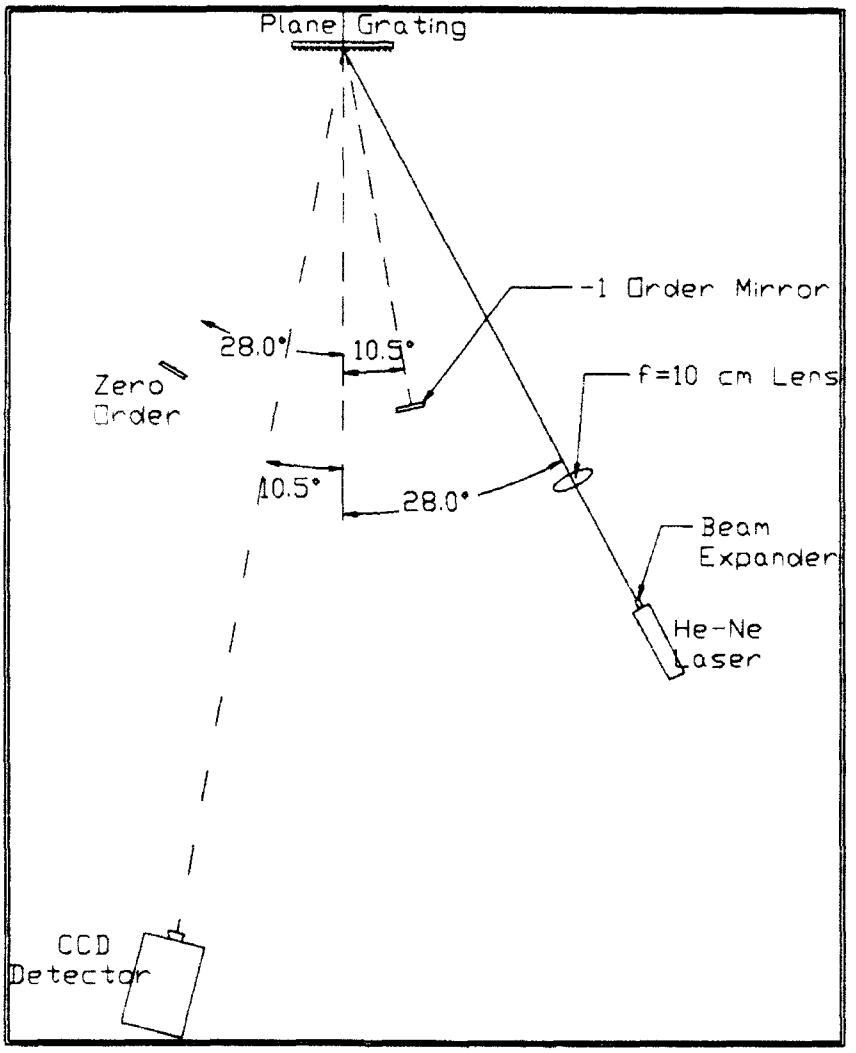

Figure 27 Diagram Of SH Instrument Layout (Overhead View)

As discussed in Chapter III, if the instrument configuration was tuned to the reference wavelength λ_0, and the mirrors were placed so as to provide equivalent path lengths, then plane parallel wave fronts would strike the detector and provide complete constructive interference across the detector. The laser light is nearly monochromatic. In order to simulate a wavelength change ($\Delta\lambda$), the first order mirror was rotated slightly to provide a $\Delta\theta$ (as illustrated in Figures 11 and 12).

C. INTERFERENCE WITH DART PROCEDURES

The interference characteristics of the SH model were evaluated with the DART program. The text files containing the input parameters are contained within Appendix D and E. The interference patterns were first generated by configuring the model to a tuned condition for wavelength λ_0= 5435 Å. The dimensions were equivalent to the physical model. Small changes in wavelength ($\Delta\lambda$) were then input and the resulting interference patterns observed. Wavelength deviations of -0.50, +0.25, +0.50, +1.00, and +2.00 Å were entered for the ray tracing.

The same model was again evaluated with only the "tuned " 5435 Å wavelength source. By changing the first order mirror angle parameter, interference patterns could be created just as they were for the physical model. For the runs, the mirror was rotated 0.025, 0.0125, 0.00625 and 0.00313 degrees from the tuned position.

Finally, a layout of a conceptual SH model was input into DART to observe the atomic oxygen emissions at 1304 Å. The input text file is included in Appendix E. The mirrors and source were placed 25 cm from a 6000 lines/mm grating. The detector was located 30 cm from the grating. A feature of DART was used to make one interference run with multiple wavelengths. The model was tuned to 1302 Å, and wavelengths were input at 1302.17, 1304.87, 1306.04 Å at three representative intensities (Wiese et al., 1966).

D. RESULTS AND DISCUSSION

1. Laboratory Model

An interference fringe pattern was produced by the prototype SH model using the laser light source. The observed contrast was sharp and the quality excellent. A photograph of the monitor showing the fringe pattern is presented in Figure 28.

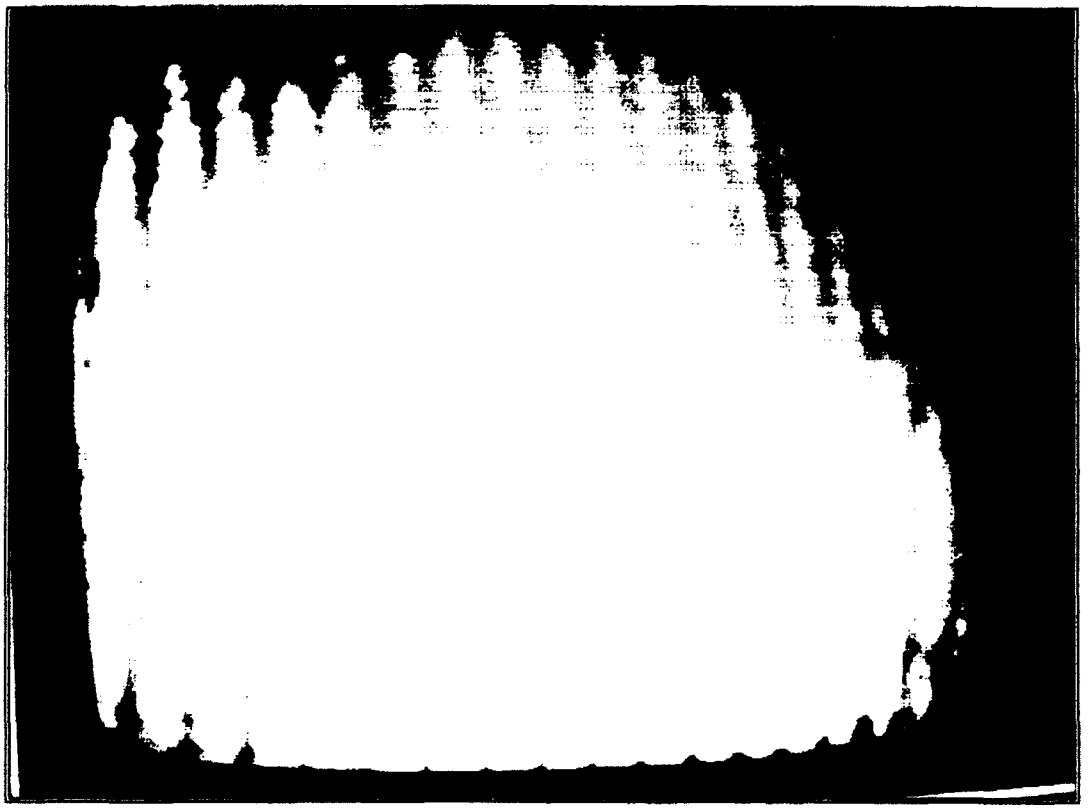

Figure 28 Photograph of SH Model Interference Pattern

Mirror positioning was very sensitive in that very small angular deviations would change the orientation and spacing of the lines in the interference fringe pattern a significant amount. Vertical parallel lines could be produced by ensuring the normals of the optical elements were in the same plane. If one of the mirrors was rotated about the horizontal axis, the interference lines would rotate in a range from vertical to horizontal. Rotation of the mirror about the vertical axis

would change the spacing between the lines. Mirror alignment was critical in producing a fringe pattern with evenly spaced, parallel lines.

The fringe pattern was sensitive to environmental vibrational disturbances. Touching the optical table would cause the pattern to vibrate but not disappear. This becomes important in the final design of the instrument for a spacecraft. The mirror and grating should be mounted together as a single unit to force the components to vibrate together. Mounted as a group, the optical paths would change together, thereby minimizing interference pattern disturbances.

Qualitatively, the vibrational sensitivity was not as severe as the spherical grating model. The cause may be attributed to the spherical grating model having its optical elements mounted twice as high above the optical table compared to the SH model elements. For follow-on testing the optical elements of the SH model will be mounted closer to the optical table surface to help reduce the vibrational sensitivity.

The incident light in the SH model must be collimated. This was accomplished in the prototype SH model with a convex lens. Although a Magnesium Fluoride (MgF_4) lens may serve as a collimator for radiation in the FUV region, a preferred solution would be a reflective surface such as an off--axis parabolic reflector. This adds another reflection into the path for a total of four, but the benefit would be the ability to move into the EUV region which requires the use of all-reflective surfaces. At the close of this writing, the prototype SH model had been modified and successfully tested in the laboratory using an off-axis parabolic reflector as the collimator for incident laser radiation.

2. DART Interference of SH Model

The DART program ray tracing produces similar results as the prototype. The text and interference pattern plots from the prototype SH runs are contained within Appendix D. Figure 29 is a representative interference pattern resulting from a "First Order" mirror rotation.

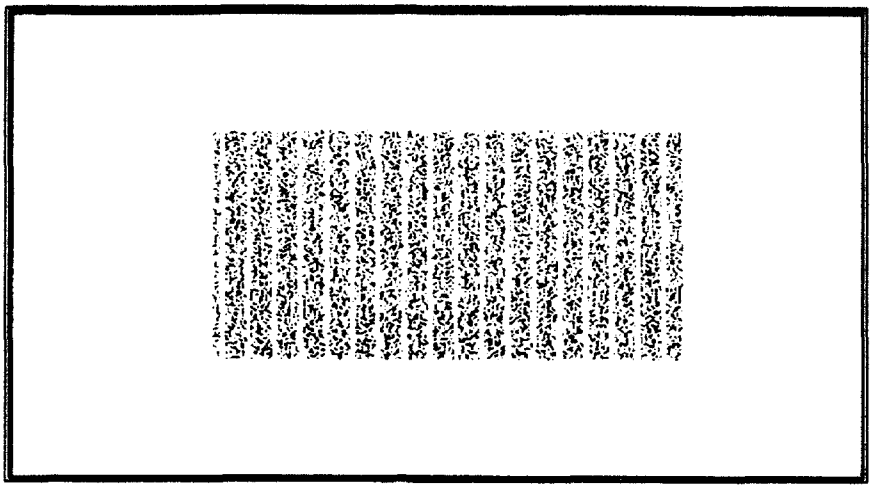

Figure 29 DART Interference Pattern

Recall that the DART interference diagram has over 200 variations of gray scale to represent interference magnitude. The values range from a black pixel representing complete constructive interference, to the white pixel for complete destructive interference. Therefore, the darker points in the interference diagram correspond to the brighter fringe lines in the monitor photograph.

Figure 50 in Appendix D shows the interference pattern diagram for the tuned condition whereby the input wavelength is the tuned condition wavelength λ_0 = 5435 Å. As expected the wave fronts are parallel to the detector surface and result in constructive interference across the entire span of the detector. By inserting small deviations from the tuned wavelength, a recognizable interference pattern results as shown in Figures 51 through 55 for various $\Delta\lambda$. The interference pattern spans across one centimeter for all of the diagrams.

Alternatively, we can reproduce this effect by rotating one of the mirrors slightly to place a small angular deviation ($\Delta\theta$) in the instrument. The interference pattern diagrams shown in Figures 56 through 59 were created by rotating the first order mirror. As can be seen in the diagrams, the instrument is very sensitive to small angular increments. For example, the interference pattern shown in Figures 29 and 59 were from rotating the first order mirror 0.0125

degrees (45 arc seconds). This was the method by which the interference fringes created by the laboratory SH model were adjusted.

The intensity values from Figure 53 is summed in the vertical to produce the Figure 30 interference profile. This is a plot of intensity as a function of detector position and is similar to the curve depicted in Figure 12 and discussed in Chapter III. The Fourier Transform of this pattern would be the delta function of a sine squared function, representing the spatial frequency of the wave form. Recall that the spatial frequency is related to the difference ($\Delta\lambda$) from the reference wavelength and not the input wavelength alone.

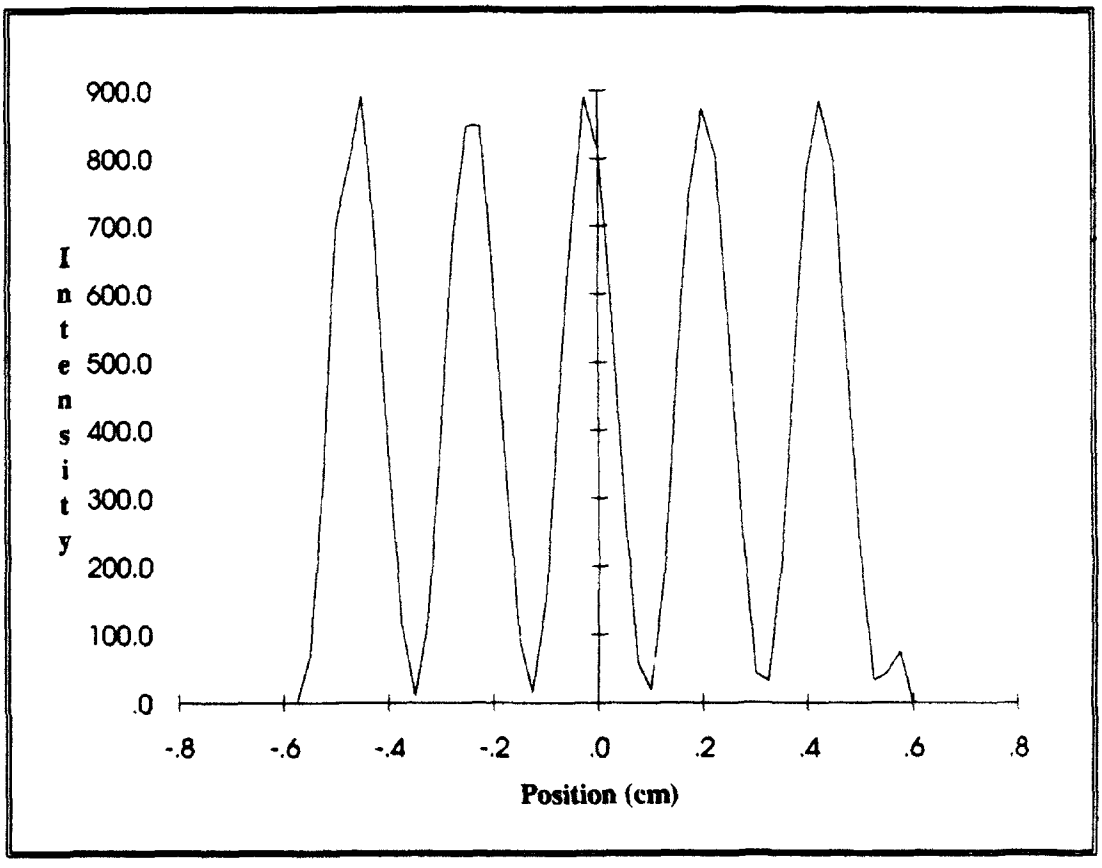

Figure 30 Plot of Intensity vs. Detector Position for 5435.5 Å

A combination of wavelengths such as the atomic oxygen triplet emissions near 1304 Å would produce the intensity profile shown in Figure 31. The SH model used to generate Figure 31 was tuned to 1302 Å and had a grating ruling density of 4800 lines/mm. The data files are presented in Appendix E. The wave form is the superposition of the three input wavelengths at various intensity levels. By taking the Fourier Transform of the pattern, the spatial frequencies could be recovered.

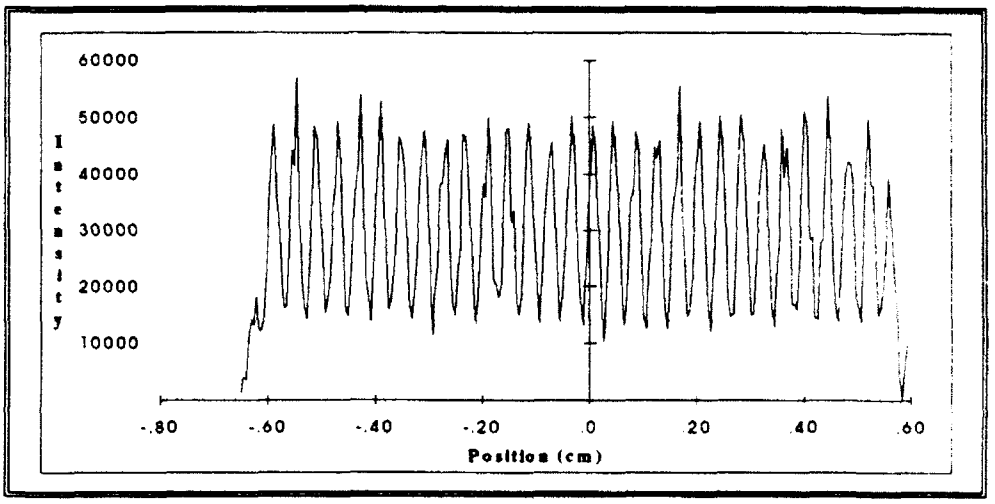

Figure 31 Plot of Intensity vs. Detector Distance for Atomic Oxygen

3. Resolution and Bandwidth

The limit of resolution for the instrument can be calculated by substituting the length of the detector array into Equation 17. For the laboratory SH model, the detector length (L) is one centimeter. The grating ruling value **a** = 8.333 x 10^{-7} m/line, and the tuned or reference wavelength is λ_0 = 5435 Å. Substituting these values into Equation 17 yields

$$\Delta\lambda_{min} = \frac{\lambda_0}{2L}\sqrt{a^2 - (\frac{\lambda_0}{2})^2} = 0.2263\mathring{A} \qquad (28)$$

for the limit of resolution of the prototype SH model. The resolving power is $\lambda/\Delta\lambda$=2.4 x 10^4 .

The atomic oxygen (1304 Å) SH model is anticipated to have a detector array length of 1 inch or 2.54 cm with 1024 elements. The grating would have ruling density of 6000 lines/mm, the inverse of which gives the value of a = 1.6667 x 10^7 m/line. Inserting these values into Equation 17 yields a limit of resolution $\Delta\lambda_{min}$ = 0.00394 Å. The resolving power is $\lambda / \Delta \lambda = 3.3 \times 10^5$.

The bandwidth is determined by the number of detector elements and the Nyquist Sampling criterion. By taking two samples per cycle setting N = 1024 for the number of detector elements, the bandwidth of the atomic oxygen model is

$$(\frac{N}{2})\Delta\lambda_{min} = (512)(0.00394) = 2.02\,\text{Å} \quad . \tag{29}$$

The interferometer can be "optimized" for the emission of interest by manipulating several parameters. For a given λ_0, N and L, the bandwidth can be increased with a lower grating ruling density. This was done for the atomic oxygen ray trace shown in Figures 31 and 60. This may be a desirable trade-off if the loss of light from the "unused" orders and the lower resolution is acceptable.

VI. SUMMARY, CONCLUSIONS AND RECOMMENDATIONS

A. SUMMARY OF FINDINGS

Within the scope of this study, analysis of the spherical grating interferometer ray tracing resulted in the determination that it would be extremely difficult to interpret the data from this instrument due to the non-linear interference patterns it produces. This conclusion was based upon spot diagram ray trace results.

The interferometer was redesigned and a new spatial heterodyne (SH) interferometer model was built and tested using a visible light laser source. The laboratory instrument produced high contrast, linear interference fringes that are suitable for inversion. Although the laboratory feasibility test was conducted with a quasi-monochromatic 5435 Å light source, ray trace results demonstrate the potential for the SH model operate in the EUV and FUV region with resolving powers of nearly 10^6 for $\lambda/\Delta\lambda$. Typical resolution values in this region is one to four milli--angstroms.

The SH model uses a single, holographic diffraction grating for both the splitting and the recombination of the incident radiation. This reduces the problems associated with multiple grating alignment or different ruling densities. The ruling density on the single plane grating can be optimized for the wavelength of interest, thereby eliminating unused diffraction orders and maximizing the throughput of the instrument. A blazed diffraction grating is not required.

The rigid mounting of the optical components enhances the reliability of the devices as there are no moving components. The layout of the elements makes the device easy to tune to the desired reference wavelength. The SH interferometer is simple, compact and lightweight making the device suitable for a spacecraft payload. The optical components are relatively inexpensive for an interferometer with this high resolution.

B. RECOMMENDATIONS FOR FURTHER STUDY

The prototype SH was tested with a single wavelength, long coherence length, visible laser source. Follow-on testing should be made with shorter coherence length sources at a variety of wavelengths. Recommended sources are the sodium and mercury lamps. These sources should be evaluated using the all-reflection SH model incorporating the off-axis parabolic reflector as the collimator.

Although bandwidth was calculated for the SH model, further investigation is required to determine the effects of the broad band of wavelengths surrounding the wavelength of interest. Undesired orders from wavelengths outside of the normal bandwidth can still pose a problem. It may be necessary to implement a filter at the aperture to provide additional band pass. Other alternatives may include optical dimensioning and placement to ensure that undesired background or adjoining emissions are "walked off" of the detector.

A detector suitable for sensing the FUV and EUV portion of the spectrum must be investigated. Detector size should be optimized for the desired resolution and bandwidth when making this choice.

Finally, a suitable arrangement and mount for the optical components must be investigated to conform to sounding rocket or space vehicle payload dimensions, but still offer adequate performance. Vibration and temperature testing of the optical element mounts is recommended prior to flight.

BEAM FOUR OPTICS TABLE FILES
SPHERICAL GRATING
FIRST AND ZERO ORDER TRACE

DETECTOR ON ROWLAND CIRCLE

5 entries Zsgdorc.opt ZERO ORDER Wallace 22 November 1992

Mir/I	Xvx	Zvx	Pitch	Curvature	Shape	Diam	Ord	Gx
Iris	11.73848345	4.04927176	-38.06446295		1.0	0.1		
Grat		19.039053	-19.03223147	-.04965243	1.0	5.08	0	1.2
Mir					1.0	1.00		
Grat		19.039053	-19.03223147	-.04965243	1.0	5.08	-1	1.2
Det					1.0	5.00		

Spherical Grating, Zero Order Mirror Path, Detector on Rowland Circle

5 entries 1sgdorc.opt FIRST ORDER Wallace 22 November 1992

Mir/I	Xvx	Zv x	Pitch	Curvature	Shape	Diam	Ord	Gx
Iris	11.73848345	4.04927176	-38.06446295		1.0	0.1		
Grat		19.039053	-19.03223147	-.04965243	1.0	5.08	1	1.2
Mir	11.73848345	4.04927176	-38.06446295		1.0	1.00		
Grat		19.039053	-19.03223147	-.04965243	1.0	5.08	0	1.2
Det					1.0	5.00		

Beam 4 Optics Table for Spherical Grating, First Order Path,
Detector Located on Rowland Circle

BEAM FOUR OPTICS TABLE FILE
SPHERICAL GRATING
FIRST AND ZERO ORDER TRACE
DETECTOR ON ROWLAND CIRCLE

21 rays ZSGRDORC.RAY 2 Deg Fan Beam in Vert and Horiz Wallace 22 November 1992

X0	Z0	U0	V0	@wavelen		Xfinal	Yfinal	Zfinal	Note	
11.73848345	4.04927176	-0.65145425		.5435	R	0.0004	0.0000	0.0000	ok	5
11.73848345	4.04927176	-0.64447292		.5435	R	0.0002	0.0000	-0.0000	ok	5
11.73848345	4.04927176	-0.63749162		.5435	R	0.0001	0.0000	-0.0000	ok	5
11.73848345	4.04927176	-0.6305103		.5435	R	0.0000	0.0000	-0.0000	ok	5
11.73848345	4.04927176	-0.62352899		.5435	R	0.0000	0.0000	-0.0000	ok	5
11.73848345	4.04927176	-0.61654767		.5435	G	-0.0000	0.0000	0.0000	ok	5
11.73848345	4.04927176	-0.60956635		.5435	R	-0.0000	0.0000	-0.0000	ok	5
11.73848345	4.04927176	-0.60258504		.5435	R	-0.0000	0.0000	-0.0000	ok	5
11.73848345	4.04927176	-0.59500372		.5435	R	-0.0001	0.0000	0.0000	ok	5
11.73848345	4.04927176	-0.5886224		.5435	R	-0.0002	0.0000	-0.0000	ok	5
11.73848345	4.04927176	-0.58164108		.5435	R	-0.0004	0.0000	0.0000	ok	5
11.73848345	4.04927176	-0.61654767	0.03490659	.5435	Y	-0.0019	-0.2226	-0.0000	ok	5
11.73848345	4.04927176	-0.61654767	0.02792527	.5435	Y	-0.0012	-0.1781	-0.0000	ok	5
11.73848345	4.04927176	-0.61654767	0.02094395	.5435	Y	-0.0007	-0.1336	0.0000	ok	5
11.73848345	4.04927176	-0.61654767	0.01396263	.5435	Y	-0.0003	-0.0890	0.0000	ok	5
11.73848345	4.04927176	-0.61654767	0.00698132	.5435	Y	-0.0001	-0.0445	0.0000	ok	5
11.73848345	4.04927176	-0.61654767	-.00698132	.5435	Y	-0.0001	0.0445	0.0000	ok	5
11.73848345	4.04927176	-0.61654767	-.01396263	.5435	Y	-0.0003	0.0890	0.0000	ok	5
11.73848345	4.04927176	-0.61654767	-.02094395	.5435	Y	-0.0007	0.1336	0.0000	ok	5
11.73848345	4.04927176	-0.61654767	-.02792527	.5435	Y	-0.0012	0.1781	-0.0000	ok	5
11.73848345	4.04927176	-0.61654767	-.03490659	.5435	Y	-0.0019	0.2226	-0.0000	ok	5

Ray Table for +- Two Degree Fan Beam, Zero Order Path, Detector on Rowland Circle
Green Color is the Chief Ray, Red is In-Plane Horiz Fan, Yellow is Vertical Plane

BEAM FOUR RAY TABLE FILE
SPHERICAL GRATING
FIRST ORDER TRACE
DETECTOR ON ROWLAND CIRCLE

21 rays 1SGRDORC.RAY 2 Deg Fan Beam in Vert and Horiz Wallace 22 November 1992

X0	Z0	U0	V0	@wavelen		Xfinal	Yfinal	Zfinal	Note	
11.73848345	4.04927176	-0.65145425		.5435	R	0.0004	0.0000	0.0000	ok	5
11.73848345	4.04927176	-0.64447292		.5435	R	0.0002	0.0000	0.0000	ok	5
11.73848345	4.04927176	-0.63749162		.5435	R	0.0001	0.0000	0.0000	ok	5
11.73848345	4.04927176	-0.6305103		.5435	R	0.0000	0.0000	-0.0000	ok	5
11.73848345	4.04927176	-0.62352899		.5435	R	0.0000	0.0000	-0.0000	ok	5
11.73848345	4.04927176	-0.61654767		.5435	G	-0.0000	0.0000	0.0000	ok	5
11.73848345	4.04927176	-0.60956635		.5435	R	-0.0000	0.0000	-0.0000	ok	5
11.73848345	4.04927176	-0.60258504		.5435	R	-0.0000	0.0000	0.0000	ok	5
11.73848345	4.04927176	-0.59500372		.5435	R	-0.0001	0.0000	-0.0000	ok	5
11.73848345	4.04927176	-0.5886224		.5435	R	-0.0002	0.0000	0.0000	ok	5
11.73848345	4.04927176	-0.58164108		.5435	R	-0.0004	0.0000	-0.0000	ok	5
11.73848345	4.04927176	-0.61654767	0.03490659	.5435	Y	0.0029	-0.2226	-0.0000	ok	5
11.73848345	4.04927176	-0.61654767	0.02792527	.5435	Y	0.0019	-0.1781	-0.0000	ok	5
11.73848345	4.04927176	-0.61654767	0.02094395	.5435	Y	0.0011	-0.1336	0.0000	ok	5
11.73848345	4.04927176	-0.61654767	0.01396263	.5435	Y	0.0005	-0.0890	-0.0000	ok	5
11.73848345	4.04927176	-0.61654767	0.00698132	.5435	Y	0.0001	-0.0445	0.0000	ok	5
11.73848345	4.04927176	-0.61654767	-.00698132	.5435	Y	0.0001	0.0445	0.0000	ok	5
11.73848345	4.04927176	-0.61654767	-.01396263	.5435	Y	0.0005	0.0890	-0.0000	ok	5
11.73848345	4.04927176	-0.61654767	-.02094395	.5435	Y	0.0011	0.1336	0.0000	ok	5
11.73848345	4.04927176	-0.61654767	-.02792527	.5435	Y	0.0019	0.1781	-0.0000	ok	5
11.73848345	4.04927176	-0.61654767	-.03490659	.5435	Y	0.0029	0.2226	-0.0000	ok	5

Ray Table for +- Two Degree Fan Beam, First Order Path, Detector on Rowland Circle
Green Color is the Chief Ray, Red is In-Plane Horiz Fan, Yellow is Vertical Plane

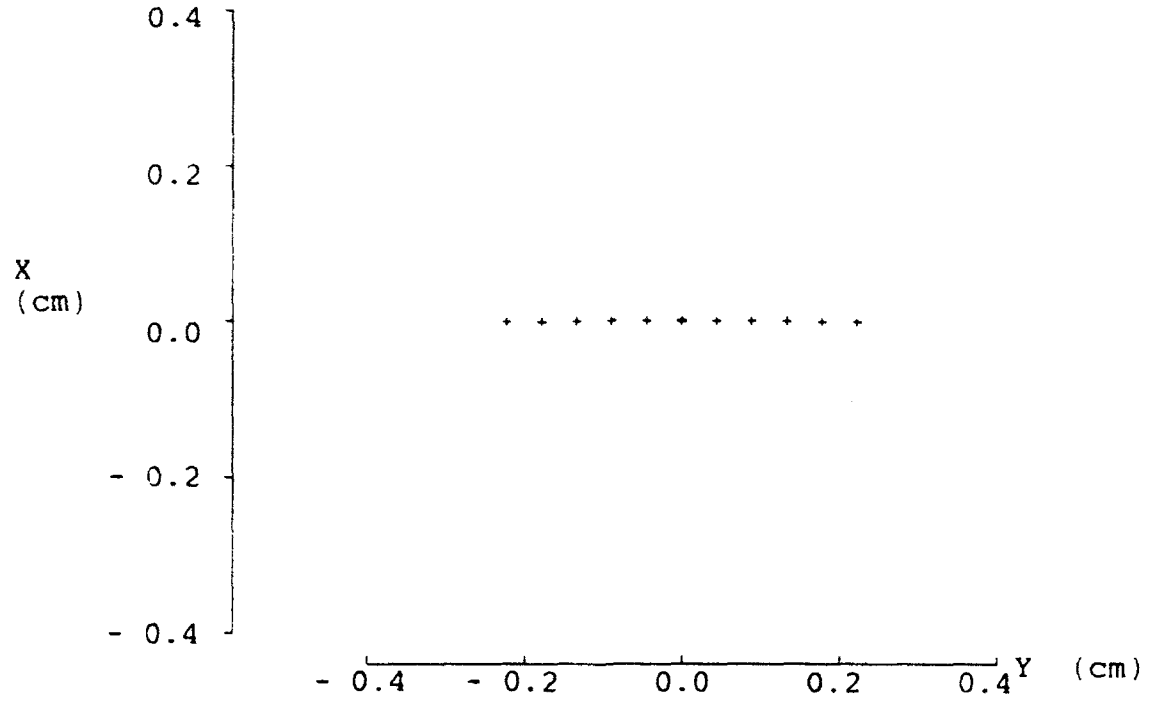

Figure 32 Zero Order Spot Diagram (Detector on Rowland Circle)

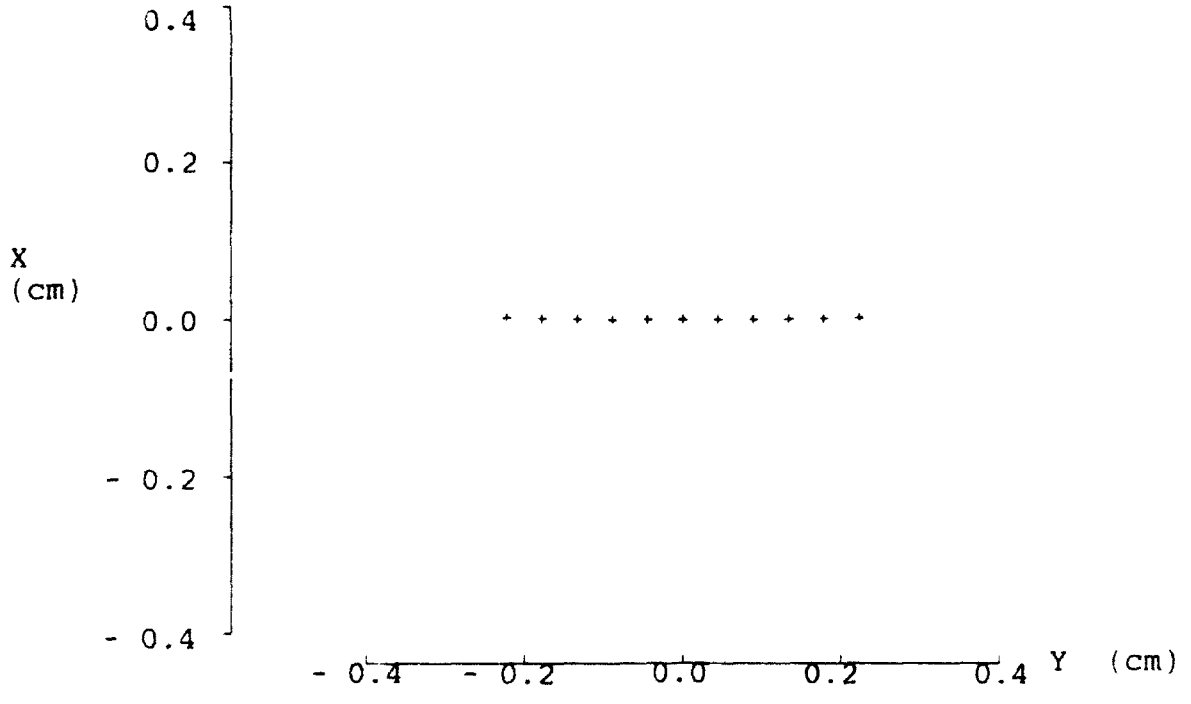

Figure 33 First Order Spot Diagram (Detector on Rowland Circle)

BEAM FOUR OPTICS TABLE FILES
SPHERICAL GRATING
FIRST AND ZERO ORDER TRACE

TANGENTIAL FOCAL PLANE SEARCH

5 entries Zsgtanx.opt ZERO ORDER Wallace 22 November 1992

Mir/I	Xvx	Zvx	Pitch	Curvatur	Shape	Diam	Ord	Gx
Iris	11.73848345	4.04927176	-38.06446295		1.0	0.1		
Grat		19.039053	-19.03223147	-.04965243	1.0	5.08	0	1.2
Mir					1.0	1.00		
Grat		19.039053	-19.03223147	-.04965243	1.0	5.08	-1	1.2
Det		-0.00607?			1.0	5.00		

Beam 4 Optics Table for Spherical Grating, Zero Order Path,
AUTOADJUST search for Tangential Focal Plane (x min)

5 entries 1sgtanx.opt FIRST ORDER Wallace 22 November 1992

Mir/I	Xvx	Zvx	Pitch	Curvatu	Shape	Diam	Ord	Gx
Iris	11.73848345	4.04927176	-38.06446295		1.0	0.1		
Grat		19.039053	-19.03223147	-.04965243	1.0	5.08	1	1.2
Mir	11.73848345	4.04927176	-38.06446295		1.0	1.00		
Grat		19.039053	-19.03223147	-.04965243	1.0	5.08	0	1.2
Det		-0.00676?			1.0	5.00		

Beam 4 Optics Table for Spherical Grating, First Order Path,
AUTOADJUST search for Tangential Focal Plane (x min)

BEAM FOUR RAY TABLE FILE
SPHERICAL GRATING
ZERO ORDER TRACE
TANGENTIAL FOCAL PLANE

21 rays SGTANX.RAY +- 2 deg fan in vert and hor Wallace 8 Jul 92

X0	Z0	U0	V0	@wavelen	xgoal	Xfinal	Yfinal	Zfinal	Note
11.73848345	4.04927176	-0.65145425		.5435	R.0001	0.0002	0.0000	-0.0061	ok 5
11.73848345	4.04927176	-0.64447292		.5435	R.0001	-0.0000	0.0000	-0.0061	ok 5
11.73848345	4.04927176	-0.63749162		.5435	R.0001	-0.0001	0.0000	-0.0061	ok 5
11.73848345	4.04927176	-0.6305103		.5435	R.0001	-0.0001	0.0000	-0.0061	ok 5
11.73848345	4.04927176	-0.62352899		.5435	R.0001	-0.0001	0.0000	-0.0061	ok 5
11.73848345	4.04927176	-0.61654767		.5435	G.0001	-0.0000	0.0000	-0.0061	ok 5
11.73848345	4.04927176	-0.60956635		.5435	R.0001	0.0001	0.0000	-0.0061	ok 5
11.73848345	4.04927176	-0.60258504		.5435	R.0001	0.0001	0.0000	-0.0061	ok 5
11.73848345	4.04927176	-0.59500372		.5435	R.0001	0.0001	0.0000	-0.0061	ok 5
11.73848345	4.04927176	-0.5886224		.5435	R.0001	0.0000	0.0000	-0.0061	ok 5
11.73848345	4.04927176	-0.58164108		.5435	R.0001	-0.0001	0.0000	-0.0061	ok 5
11.73848345	4.04927176	-0.61654767	0.03490659	.5435	Y.0001	-0.0019	-0.2226	-0.0061	ok 5
11.73848345	4.04927176	-0.61654767	0.02792527	.5435	Y.0001	-0.0012	-0.1780	-0.0061	ok 5
11.73848345	4.04927176	-0.61654767	0.02094395	.5435	Y.0001	-0.0007	-0.1335	-0.0061	ok 5
11.73848345	4.04927176	-0.61654767	0.01396263	.5435	Y.0001	-0.0003	-0.0890	-0.0061	ok 5
11.73848345	4.04927176	-0.61654767	0.00698132	.5435	Y.0001	-0.0001	-0.0445	-0.0061	ok 5
11.73848345	4.04927176	-0.61654767	-.00698132	.5435	Y.0001	-0.0001	0.0445	-0.0061	ok 5
11.73848345	4.04927176	-0.61654767	-.01396263	.5435	Y.0001	-0.0003	0.0890	-0.0061	ok 5
11.73848345	4.04927176	-0.61654767	-.02094395	.5435	Y.0001	-0.0007	0.1335	-0.0061	ok 5
11.73848345	4.04927176	-0.61654767	-.02792527	.5435	Y.0001	-0.0012	0.1780	-0.0061	ok 5
11.73848345	4.04927176	-0.61654767	-.03490659	.5435	Y.0001	-0.0019	0.2226	-0.0061	ok 5

BEAM FOUR RAY TABLE FILE
SPHERICAL GRATING
FIRST ORDER TRACE
TANGENTIAL FOCAL PLANE

21 rays SGTANX.RAY +- 2 deg fan in vert and hor Wallace 8 Jul 92

X0	Z0	U0	V0	@wavelen	xgoal	Xfinal	Yfinal	Zfinal	Note
11.73848345	4.04927176	-0.65145425		.5435	R.0001	0.0001	0.0000	-0.0068	ok 5
11.73848345	4.04927176	-0.64447292		.5435	R.0001	-0.0000	0.0000	-0.0068	ok 5
11.73848345	4.04927176	-0.63749162		.5435	R.0001	-0.0001	0.0000	-0.0068	ok 5
11.73848345	4.04927176	-0.6305103		.5435	R.0001	-0.0001	0.0000	-0.0068	ok 5
11.73848345	4.04927176	-0.62352899		.5435	R.0001	-0.0001	0.0000	-0.0068	ok 5
11.73848345	4.04927176	-0.61654767		.5435	G.0001	-0.0000	0.0000	-0.0068	ok 5
11.73848345	4.04927176	-0.60956635		.5435	R.0001	0.0001	0.0000	-0.0068	ok 5
11.73848345	4.04927176	-0.60258504		.5435	R.0001	0.0001	0.0000	-0.0068	ok 5
11.73848345	4.04927176	-0.59500372		.5435	R.0001	0.0001	0.0000	-0.0068	ok 5
11.73848345	4.04927176	-0.5886224		.5435	R.0001	0.0000	0.0000	-0.0068	ok 5
11.73848345	4.04927176	-0.58164108		.5435	R.0001	-0.0001	0.0000	-0.0068	ok 5
11.73848345	4.04927176	-0.61654767	0.03490659	.5435	Y.0001	0.0029	-0.2226	-0.0068	ok 5
11.73848345	4.04927176	-0.61654767	0.02792527	.5435	Y.0001	0.0019	-0.1780	-0.0068	ok 5
11.73848345	4.04927176	-0.61654767	0.02094395	.5435	Y.0001	0.0011	-0.1335	-0.0068	ok 5
11.73848345	4.04927176	-0.61654767	0.01396263	.5435	Y.0001	0.0005	-0.0890	-0.0068	ok 5
11.73848345	4.04927176	-0.61654767	0.00698132	.5435	Y.0001	0.0001	-0.0445	-0.0068	ok 5
11.73848345	4.04927176	-0.61654767	-.00698132	.5435	Y.0001	0.0001	0.0445	-0.0068	ok 5
11.73848345	4.04927176	-0.61654767	-.01396263	.5435	Y.0001	0.0005	0.0890	-0.0068	ok 5
11.73848345	4.04927176	-0.61654767	-.02094395	.5435	Y.0001	0.0011	0.1335	-0.0068	ok 5
11.73848345	4.04927176	-0.61654767	-.02792527	.5435	Y.0001	0.0019	0.1780	-0.0068	ok 5
11.73848345	4.04927176	-0.61654767	-.03490659	.5435	Y	0.0029	0.2226	-0.0068	ok 5

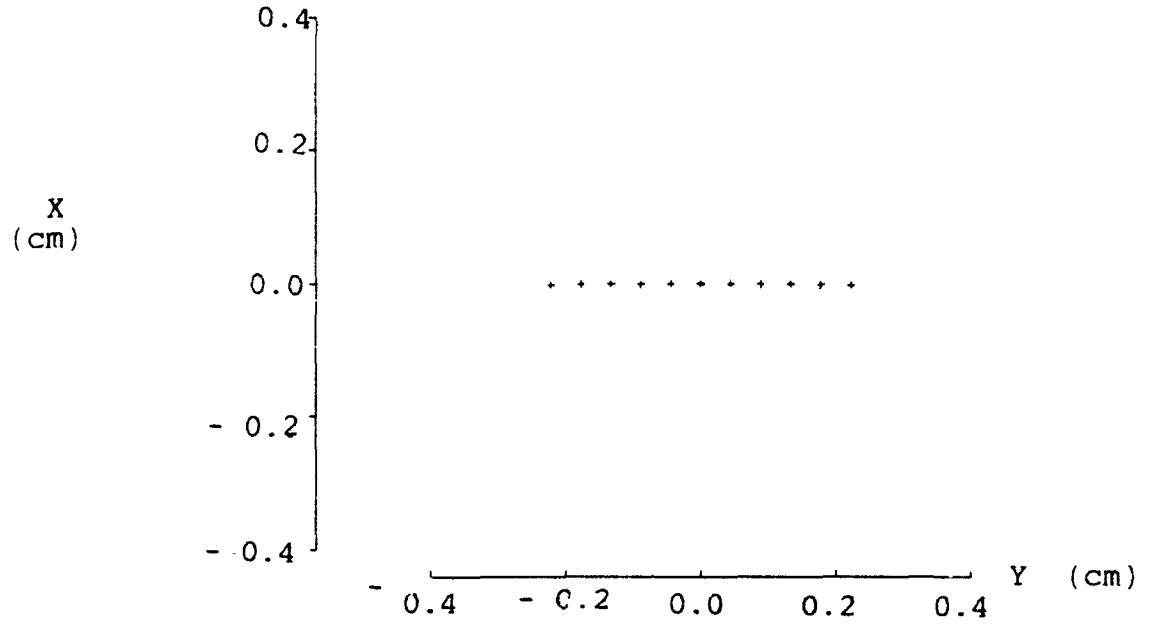

Figure 34 Zero Order Spot Diagram (Tangential)

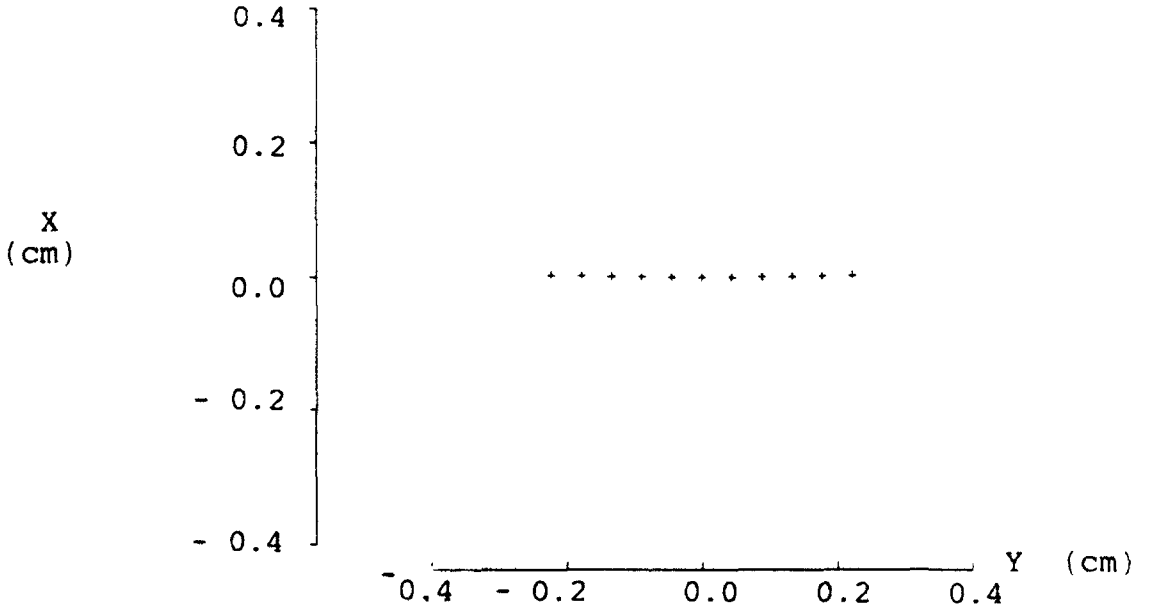

Figure 35 First Order Spot Diagram (Tangential)

BEAM FOUR OPTICS TABLE FILES
SPHERICAL GRATING
FIRST AND ZERO ORDER TRACE

SAGITTAL FOCAL PLANE SEARCH

5 entries Zsgsagy.opt ZERO ORDER Wallace 22 November 1992

Mir/I	Xvx	Zvx	Pitch	Curvatur	Shape	Diam	Ord	Gx
Iris	11.73848345	4.04927176	-38.06446295		1.0	0.1		
Grat		19.039053	-19.03223147	-.04965243	1.0	5.08	0	1.2
Mir					1.0	1.00		
Grat		19.039053	-19.03223147	-.04965243	1.0	5.08	-1	1.2
Det		-26.57449?			1.0	5.00		

5 entries 1sgsagy.opt FIRST ORDER Wallace 22 November 1992

Mir/I	Xvx	Zvx	Pitch	Curvatu	Shape	Diam	Ord	Gx
Iris	11.73848345	4.04927176	-38.06446295		1.0	0.1		
Grat		19.039053	-19.03223147	-.04965243	1.0	5.08	1	1.2
Mir	11.73848345	4.04927176	-38.06446295		1.0	1.00		
Grat		19.039053	-19.03223147	-.04965243	1.0	5.08	0	1.2
Det		-26.61126?			1.0	5.00		

BEAM FOUR RAY TABLE FILE
SPHERICAL GRATING
ZERO ORDER TRACE
SAGITTAL FOCAL PLANE

21 rays SGSAGY.RAY +- 2 deg fan in vert and hor Wallace 8 Jul 92

X0	Z0	U0	V0	@wavelen	ygoal	Xfinal	Yfinal	Zfinal	Note
11.73848345	4.04927176	-0.65145425		.5435	R.0001	-1.2182	0.0000	-26.5772	ok 5
11.73848345	4.04927176	-0.64447292		.5435	R.0001	-0.9680	0.0000	-26.5772	ok 5
11.73848345	4.04927176	-0.63749162		.5435	R.0001	-0.7211	0.0000	-26.5772	ok 5
11.73848345	4.04927176	-0.6305103		.5435	R.0001	-0.4776	0.0000	-26.5772	ok 5
11.73848345	4.04927176	-0.62352899		.5435	R.0001	-0.2372	0.0000	-26.5772	ok 5
11.73848345	4.04927176	-0.61654767		.5435	G.0001	-0.0000	0.0000	-26.5772	ok 5
11.73848345	4.04927176	-0.60956635		.5435	R.0001	0.2341	0.0000	-26.5772	ok 5
11.73848345	4.04927176	-0.60258504		.5435	R.0001	0.4653	0.0000	-26.5772	ok 5
11.73848345	4.04927176	-0.59500372		.5435	R.0001	0.7129	0.0000	-26.5772	ok 5
11.73848345	4.04927176	-0.5886224		.5435	R.0001	0.9187	0.0000.	26.5772	ok 5
11.73848345	4.04927176	-0.58164108		.5435	R.0001	1.1410	0.0000	-26.5772	ok 5
11.73848345	4.04927176	-0.61654767	0.03490659	.5435	Y.0001	-0.0114	0.0001	-26.5772	ok 5
11.73848345	4.04927176	-0.61654767	0.02792527	.5435	Y.0001	-0.0073	0.0000	-26.5772	ok 5
11.73848345	4.04927176	-0.61654767	0.02094395	.5435	Y.0001	-0.0041	-0.0000	-26.5772	ok 5
11.73848345	4.04927176	-0.61654767	0.01396263	.5435	Y.0001	-0.0018	-0.0000	-26.5772	ok 5
11.73848345	4.04927176	-0.61654767	0.00698132	.5435	Y.0001	-0.0005	-0.0000	-26.5772	ok 5
11.73848345	4.04927176	-0.61654767	-.00698132	.5435	Y.0001	-0.0005	0.0000	-26.5772	ok 5
11.73848345	4.04927176	-0.61654767	-.01396263	.5435	Y.0001	-0.0018	0.0000	-26.5772	ok 5
11.73848345	4.04927176	-0.61654767	-.02094395	.5435	Y.0001	-0.0041	0.0000	-26.5772	ok 5
11.73848345	4.04927176	-0.61654767	-.02792527	.5435	Y.0001	-0.0073	-0.0000	-26.5772	ok 5
11.73848345	4.04927176	-0.61654767	-.03490659	.5435	Y	-0.0114	-0.0001	-26.5772	ok 5

BEAM FOUR RAY TABLE FILE
SPHERICAL GRATING
FIRST ORDER TRACE
SAGITTAL FOCAL PLANE

21 rays SGSAGY.RAY +- 2 deg fan in vert and hor Wallace 8 Jul 92

X0	Z0	U0	V0	@wavelen	ygoal	Xfinal	Yfinal	Zfinal	Note
11.73848345	4.04927176	-0.65145425		.5435	R.0001	-1.1823	0.0000	-26.6113	ok 5
11.73848345	4.04927176	-0.64447292		.5435	R.0001	-0.9454	0.0000	-26.6113	ok 5
11.73848345	4.04927176	-0.63749162		.5435	R.0001	-0.7088	0.0000	-26.6113	ok 5
11.73848345	4.04927176	-0.6305103		.5435	R.0001	-0.4723	0.0000	-26.6113	ok 5
11.73848345	4.04927176	-0.62352899		.5435	R.0001	-0.2361	0.0000	-26.6113	ok 5
11.73848345	4.04927176	-0.61654767		.5435	G.0001	-0.0000	0.0000	-26.6113	ok 5
11.73848345	4.04927176	-0.60956635		.5435	R.0001	0.2359	0.0000	-26.6113	ok 5
11.73848345	4.04927176	-0.60258504		.5435	R.0001	0.4715	0.0000	-26.6113	ok 5
11.73848345	4.04927176	-0.59500372		.5435	R.0001	0.7273	0.0000	-26.6113	ok 5
11.73848345	4.04927176	-0.5886224		.5435	R.0001	0.9423	0.0000	-26.6113	ok 5
11.73848345	4.04927176	-0.58164108		.5435	R.0001	1.1775	0.0000	-26.6113	ok 5
11.73848345	4.04927176	-0.61654767	0.03490659	.5435	Y.0001	-0.0071	-0.0000	-26.6113	ok 5
11.73848345	4.04927176	-0.61654767	0.02792527	.5435	Y.0001	-0.0046	0.0000	-26.6113	ok 5
11.73848345	4.04927176	-0.61654767	0.02094395	.5435	Y.0001	-0.0026	0.0000	-26.6113	ok 5
11.73848345	4.04927176	-0.61654767	0.01396263	.5435	Y.0001	-0.0011	0.0000	-26.6113	ok 5
11.73848345	4.04927176	-0.61654767	0.00698132	.5435	Y.0001	-0.0003	0.0000	-26.6113	ok 5
11.73848345	4.04927176	-0.61654767	-.00698132	.5435	Y.0001	-0.0003	-0.0000	-26.6113	ok 5
11.73848345	4.04927176	-0.61654767	-.01396263	.5435	Y.0001	-0.0011	-0.0000	-26.6113	ok 5
11.73848345	4.04927176	-0.61654767	-.02094395	.5435	Y.0001	-0.0026	-0.0000	-26.6113	ok 5
11.73848345	4.04927176	-0.61654767	-.02792527	.5435	Y.0001	-0.0046	-0.0000	-26.6113	ok 5
11.73848345	4.04927176	-0.61654767	-.03490659	.5435	Y.0001	-0.0071	0.0000	-26.6113	ok 5

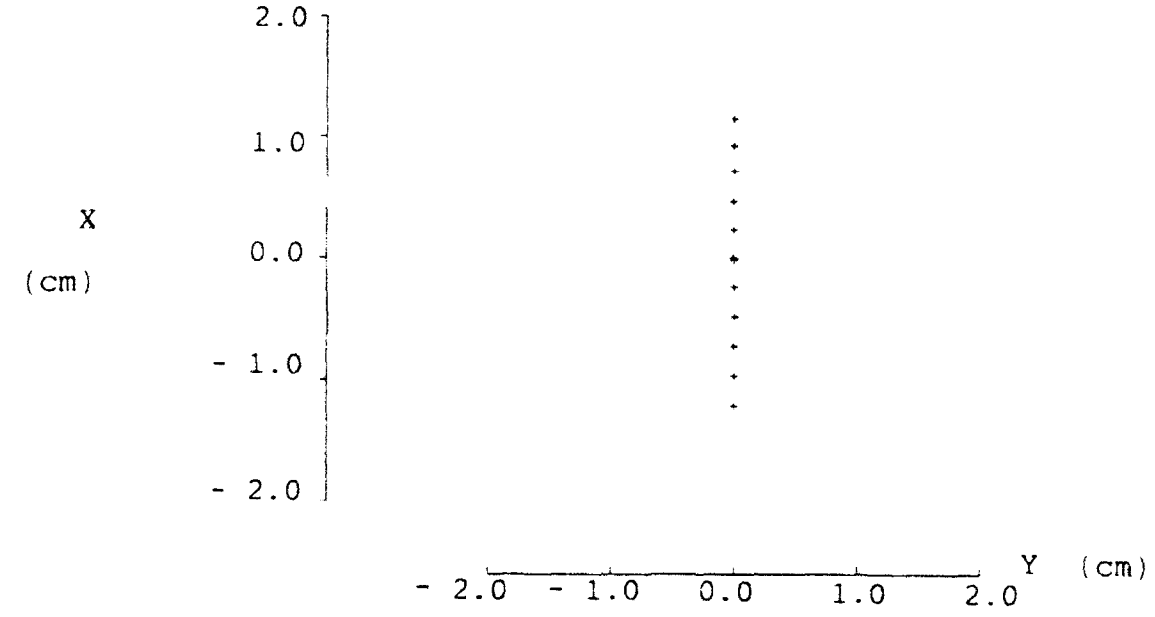

Figure 36 Zero Order Spot Diagram (Sagittal)

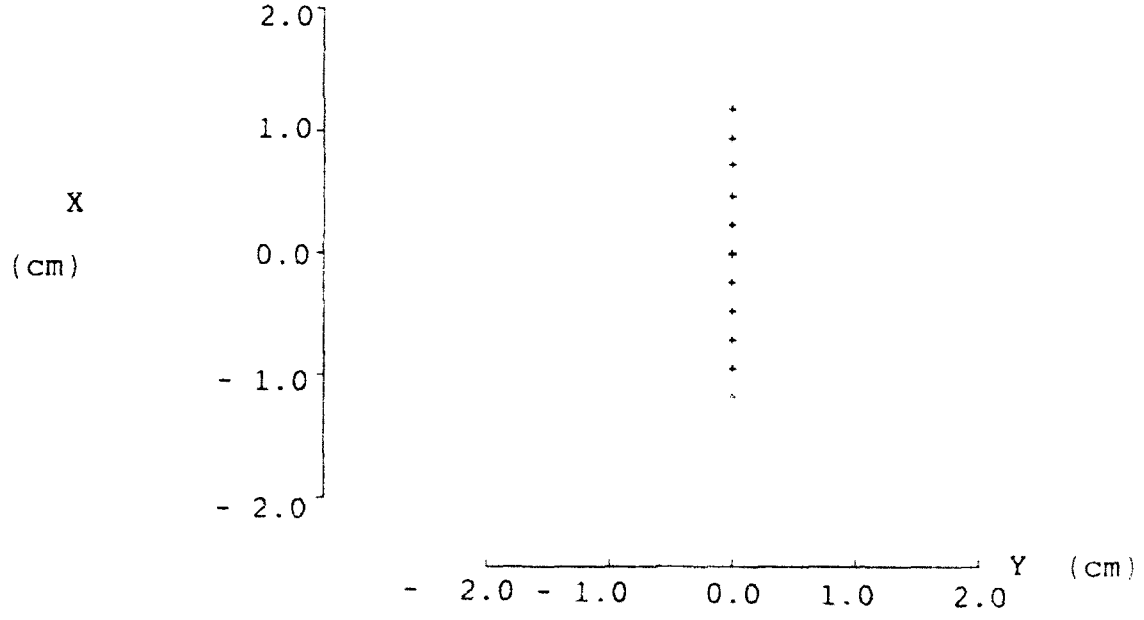

Figure 37 First Order Spot Diagram (Sagittal)

BEAM FOUR OPTICS TABLE FILES
SPHERICAL GRATING
FIRST AND ZERO ORDER TRACE

CIRCLE OF LEAST CONFUSION

5 entries Zsgdorc.opt Wallace 22 November 1992

Mir/I	Xvx	Zvx	Pitch	Curvatur	Shape	Diam	Ord	Gx
Iris	11.73848345	4.04927176	-38.06446295		1.0	0.1		
Grat		19.039053	-19.03223147	-.04965243	1.0	5.08	0	1.2
Mir					1.0	1.00		
Grat		19.039053	-19.03223147	-.04965243	1.0	5.08	-1	1.2
Det		-0.91545?			1.0	5.00		

5 entries 1SGXYMIN.OPT Wallace 22 November 1992

Mir/I	Xvx	Zvx	Pitch	Curvatu	Shape	Diam	Ord	Gx
Iris	11.73848345	4.04927176	-38.06446295		1.0	0.1		
Grat		19.039053	-19.03223147	-.04965243	1.0	5.08	1	1.2
Mir	11.73848345	4.04927176	-38.06446295		1.0	1.00		
Grat		19.039053	-19.03223147	-.04965243	1.0	5.08	0	1.2
Det		-0.91679?			1.0	5.00		

BEAM FOUR RAY TABLE FILE
SPHERICAL GRATING
ZERO ORDER TRACE
CIRCLE OF LEAST CONFUSION

21 rays SGXYMIN.RAY +- 2 deg fan in vert and hor Wallace 22 November 1992

X0	Z0	U0	V0	@wavelen	xgoal	ygoal	Xfinal	Yfinal	Zfinal	Note
11.73848345	4.04927176	-0.65145425		.5435	R.0001	.0001	-0.0415	0.0000	-0.9155	ok 5
11.73848345	4.04927176	-0.64447292		.5435	R.0001	.0001	-0.0331	0.0000	-0.9155	ok 5
11.73848345	4.04927176	-0.63749162		.5435	R.0001	.0001	-0.0248	0.0000	-0.9154	ok 5
11.73848345	4.04927176	-0.6305103		.5435	R.0001	.0001	-0.0164	0.0000	-0.9154	ok 5
11.73848345	4.04927176	-0.62352899		.5435	R.0001	.0001	-0.0082	0.0000	-0.9155	ok 5
11.73848345	4.04927176	-0.61654767		.5435	G.0001	.0001	-0.0000	0.0000	-0.9155	ok 5
11.73848345	4.04927176	-0.60956635		.5435	R.0001	.0001	0.0081	0.0000	-0.9154	ok 5
11.73848345	4.04927176	-0.60258504		.5435	R.0001	.0001	0.0160	0.0000	-0.9154	ok 5
11.73848345	4.04927176	-0.59500372		.5435	R.0001	.0001	0.0245	0.0000	-0.9155	ok 5
11.73848345	4.04927176	-0.5886224		.5435	R.0001	.0001	0.0315	0.0000	-0.9155	ok 5
11.73848345	4.04927176	-0.58164108		.5435	R.0001	.0001	0.0390	0.0000	-0.9155	ok 5
11.73848345	4.04927176	-0.61654767	0.03490659	.5435	Y.0001	.0001	-0.0022	-0.2150	-0.9154	ok 5
11.73848345	4.04927176	-0.61654767	0.02792527	.5435	Y.0001	.0001	-0.0014	-0.1720	-0.9154	ok 5
11.73848345	4.04927176	-0.61654767	0.02094395	.5435	Y.0001	.0001	-0.0008	-0.1290	-0.9155	ok 5
11.73848345	4.04927176	-0.61654767	0.01396263	.5435	Y.0001	.0001	-0.0004	-0.0860	-0.9154	ok 5
11.73848345	4.04927176	-0.61654767	0.00698132	.5435	Y.0001	.0001	-0.0001	-0.0430	-0.9154	ok 5
11.73848345	4.04927176	-0.61654767	-.00698132	.5435	Y.0001	.0001	-0.0001	0.0430	-0.9154	ok 5
11.73848345	4.04927176	-0.61654767	-.01396263	.5435	Y.0001	.0001	-0.0004	0.0860	-0.9154	ok 5
11.73848345	4.04927176	-0.61654767	-.02094395	.5435	Y.0001	.0001	-0.0008	0.1290	-0.9155	ok 5
11.73848345	4.04927176	-0.61654767	-.02792527	.5435	Y.0001	.0001	-0.0014	0.1720	-0.9154	ok 5
11.73848345	4.04927176	-0.61654767	-.03490659	.5435	Y.0001	.0001	-0.0022	0.2150	-0.9154	ok 5

BEAM FOUR RAY TABLE FILE
SPHERICAL GRATING
FIRST ORDER TRACE
CIRCLE OF LEAST CONFUSION

21 rays 1SGXYMIN.RAY +- 2 deg fan in vert and hor Wallace 22 November 1992

X0	Z0	U0	V0	@wavelen	xgoal	ygoal	Xfinal	Yfinal	Zfinal	Note
11.73848345	4.04927176	-0.65145425		.5435	R.0001	.0001	-0.0403	0.0000	-0.9168	ok 5
11.73848345	4.04927176	-0.64447292		.5435	R.0001	.0001	-0.0324	0.0000	-0.9168	ok 5
11.73848345	4.04927176	-0.63749162		.5435	R.0001	.0001	-0.0243	0.0000	-0.9168	ok 5
11.73848345	4.04927176	-0.6305103		.5435	R.0001	.0001	-0.0162	0.0000	-0.9168	ok 5
11.73848345	4.04927176	-0.62352899		.5435	R.0001	.0001	-0.0081	0.0000	-0.9168	ok 5
11.73848345	4.04927176	-0.61654767		.5435	G.0001	.0001	-0.0000	0.0000	-0.9168	ok 5
11.73848345	4.04927176	-0.60956635		.5435	R.0001	.0001	0.0081	0.0000	-0.9168	ok 5
11.73848345	4.04927176	-0.60258504		.5435	R.0001	.0001	0.0162	0.0000	-0.9168	ok 5
11.73848345	4.04927176	-0.59500372		.5435	R.0001	.0001	0.0250	0.0000	-0.9168	ok 5
11.73848345	4.04927176	-0.5886224		.5435	R.0001	.0001	0.0323	0.0000	-0.9168	ok 5
11.73848345	4.04927176	-0.58164108		.5435	R.0001	.0001	0.0402	0.0000	-0.9168	ok 5
11.73848345	4.04927176	-0.61654767	0.03490659	.5435	Y.0001	.0001	0.0026	-0.2150	-0.9168	ok 5
11.73848345	4.04927176	-0.61654767	0.02792527	.5435	Y.0001	.0001	0.0016	-0.1720	-0.9168	ok 5
11.73848345	4.04927176	-0.61654767	0.02094395	.5435	Y.0001	.0001	0.0009	-0.1290	-0.9168	ok 5
11.73848345	4.04927176	-0.61654767	0.01396263	.5435	Y.0001	.0001	0.0004	-0.0860	-0.9168	ok 5
11.73848345	4.04927176	-0.61654767	0.00698132	.5435	Y.0001	.0001	0.0001	-0.0430	-0.9168	ok 5
11.73848345	4.04927176	-0.61654767	-.00698132	.5435	Y.0001	.0001	0.0001	0.0430	-0.9168	ok 5
11.73848345	4.04927176	-0.61654767	-.01396263	.5435	Y.0001	.0001	0.0004	0.0860	-0.9168	ok 5
11.73848345	4.04927176	-0.61654767	-.02094395	.5435	Y.0001	.0001	0.0009	0.1290	-0.9168	ok 5
11.73848345	4.04927176	-0.61654767	-.02792527	.5435	Y.0001	.0001	0.0016	0.1720	-0.9168	ok 5
11.73848345	4.04927176	-0.61654767	-.03490659	.5435	Y.0001	.0001	0.0026	0.2150	-0.9168	ok 5

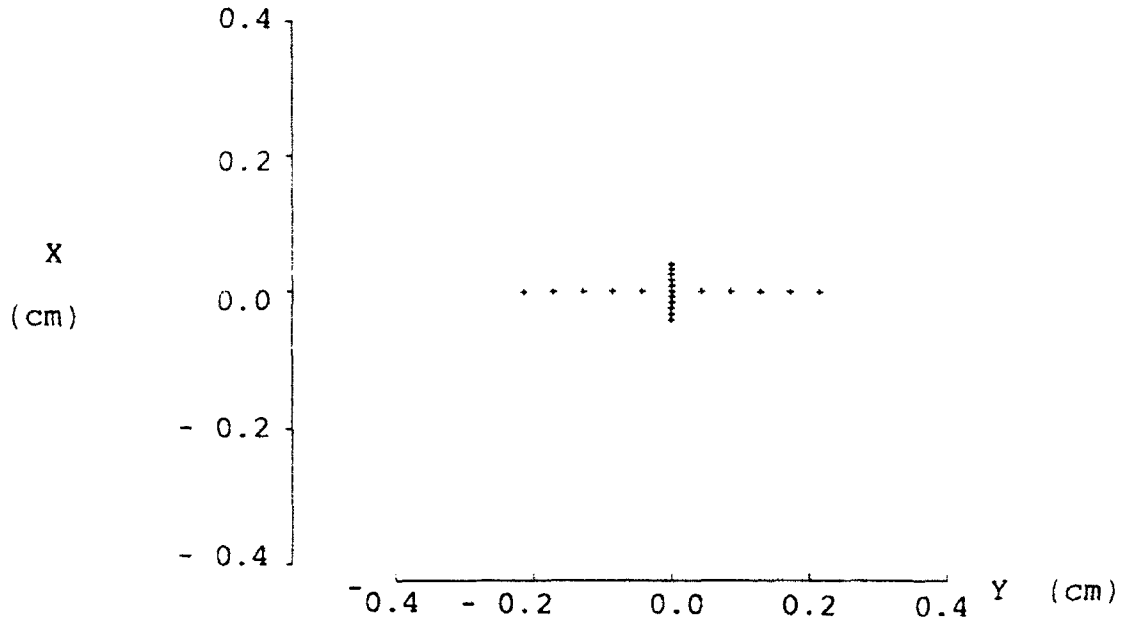

Figure 38 Zero Order Spot Diagram (Circle of Least Confusion)

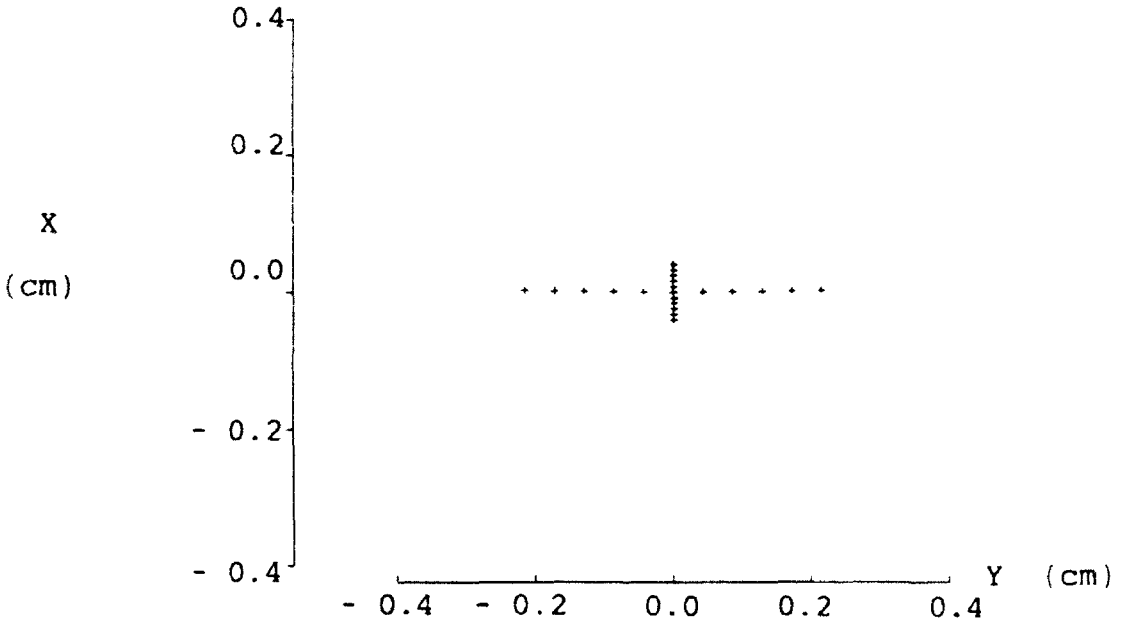

Figure 39 First Order Spot Diagram (Circle of Least Confusion)

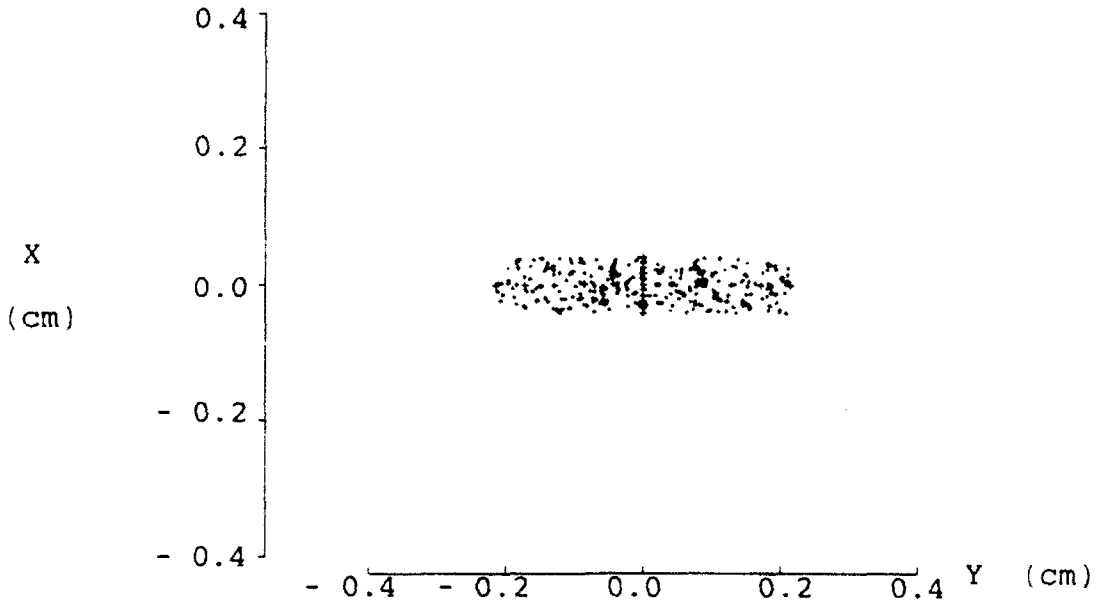

Figure 40 Zero Order Spot Diagram (Circle of Least Confusion)
300 rays

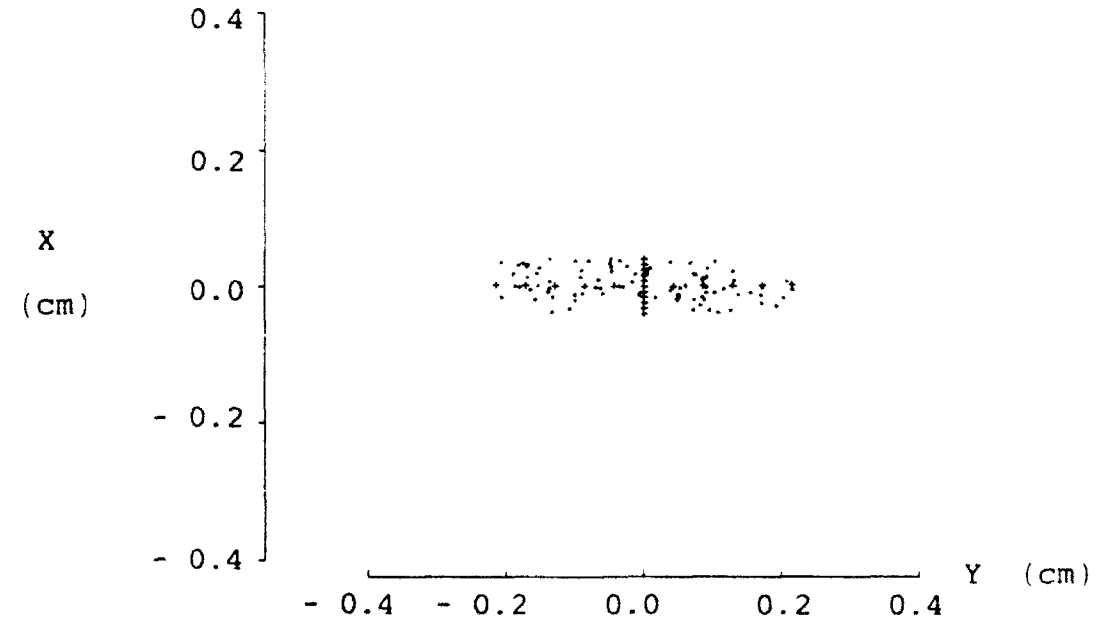

Figure 41 First Order Spot Diagram (Circle of Least Confusion)
100 rays

BEAM FOUR OPTICS TABLE FILES
SPHERICAL GRATING
FIRST AND ZERO ORDER TRACE

CYLINDRICAL MIRROR SEARCH

5 entries Zsgcylm.opt ZERO ORDER Wallace 22 November 1992

Mir/I	Xvx	Zvx	Pitch	Curvature	Cx	Roll	Shape	Diam	Ord	Gx
Iris	11.73848345	4.04927176	-38.06446295				1.0	0.1		
Grat		19.039053	-19.03223147	-.04965243			1.0	5.08	0	1.2
Mir					-0.195?	90		1.00		
Grat		19.039053	-19.03223147	-.04965243			1.0	5.08	-1	1.2
Det		-0.00637?					1.0	5.00		

5 entries 1SGCYLM.OPT FIRST ORDER Wallace 22 November 1992

Mir/I	Xvx	Zvx	Pitch	Curvature	Cx	Roll	Shape	Diam	Ord	Gx
Iris	11.73848345	4.04927176	-38.06446295				1.0	0.1		
Grat		19.039053	-19.03223147	-.04965243			1.0	5.08	1	1.2
Mir	11.73848345	4.04927176	-38.06446295		-0.1946?	90		1.00		
Grat		19.039053	-19.03223147	-.04965243			1.0	5.08	0	1.2
Det		-0.00608?					1.0	5.00		

BEAM FOUR RAY TABLE FILE
SPHERICAL GRATING
ZERO ORDER TRACE
CYLINDRICAL MIRROR

21 rays ZSGCYLM.RAY +- 2 deg fan in vert and hor Wallace 22 November 1992

X0	Z0	U0	V0	@wavelen	xgoal	ygoal	Xfinal	Yfinal	Zfinal	Note	
11.73848345	4.04927176	-0.65145425		.5435	R.0001	.0001	0.0001	0.0000	-0.0064	ok	5
11.73848345	4.04927176	-0.64447292		.5435	R.0001	.0001	-0.0000	0.0000	-0.0064	ok	5
11.73848345	4.04927176	-0.63749162		.5435	R.0001	.0001	-0.0001	0.0000	-0.0064	ok	5
11.73848345	4.04927176	-0.6305103		.5435	R.0001	.0001	-0.0001	0.0000	-0.0064	ok	5
11.73848345	4.04927176	-0.62352899		.5435	R.0001	.0001	-0.0001	0.0000	-0.0064	ok	5
11.73848345	4.04927176	-0.61654767		.5435	G.0001	.0001	-0.0000	0.0000	-0.0064	ok	5
11.73848345	4.04927176	-0.60956635		.5435	R.0001	.0001	0.0001	0.0000	-0.0064	ok	5
11.73848345	4.04927176	-0.60258504		.5435	R.0001	.0001	0.0001	0.0000	-0.0064	ok	5
11.73848345	4.04927176	-0.59500372		.5435	R.0001	.0001	0.0001	0.0000	-0.0064	ok	5
11.73848345	4.04927176	-0.5886224		.5435	R.0001	.0001	0.0000	0.0000	-0.0064	ok	5
11.73848345	4.04927176	-0.58164108		.5435	R.0001	.0001	-0.0001	0.0000	-0.0064	ok	5
11.73848345	4.04927176	-0.61654767	0.03490659	.5435	Y.0001	.0001	-0.0008	0.0004	-0.0064	ok	5
11.73848345	4.04927176	-0.61654767	0.02792527	.5435	Y.0001	.0001	-0.0005	0.0003	-0.0064	ok	5
11.73848345	4.04927176	-0.61654767	0.02094395	.5435	Y.0001	.0001	-0.0003	0.0002	-0.0064	ok	5
11.73848345	4.04927176	-0.61654767	0.01396263	.5435	Y.0001	.0001	-0.0001	0.0002	-0.0064	ok	5
11.73848345	4.04927176	-0.61654767	0.00698132	.5435	Y.0001	.0001	-0.0000	0.0001	-0.0064	ok	5
11.73848345	4.04927176	-0.61654767	-.00698132	.5435	Y.0001	.0001	-0.0000	-0.0001	-0.0064	ok	5
11.73848345	4.04927176	-0.61654767	-.01396263	.5435	Y.0001	.0001	-0.0001	-0.0002	-0.0064	ok	5
11.73848345	4.04927176	-0.61654767	-.02094395	.5435	Y.0001	.0001	-0.0003	-0.0002	-0.0064	ok	5
11.73848345	4.04927176	-0.61654767	-.02792527	.5435	Y.0001	.0001	-0.0005	-0.0003	-0.0064	ok	5
11.73848345	4.04927176	-0.61654767	-.03490659	.5435	Y.0001	.0001	-0.0008	-0.0004	-0.0064	ok	5

BEAM FOUR RAY TABLE FILE
SPHERICAL GRATING
FIRST ORDER TRACE
CYLINDRICAL MIRROR

21 rays 1SGCYLM.RAY +- 2 deg fan in vert and hor Wallace 22 November 1992

X0	Z0	U0	V0	@wavelen	xgoal	ygoal	Xfinal	Yfinal	Zfinal	Note	
11.73848345	4.04927176	-0.65145425		.5435	R.0001	.0001	0.0002	0.0000	-0.0061	ok	5
11.73848345	4.04927176	-0.64447292		.5435	R.0001	.0001	-0.0000	0.0000	-0.0061	ok	5
11.73848345	4.04927176	-0.63749162		.5435	R.0001	.0001	-0.0001	0.0000	-0.0061	ok	5
11.73848345	4.04927176	-0.6305103		.5435	R.0001	.0001	-0.0001	0.0000	-0.0061	ok	5
11.73848345	4.04927176	-0.62352899		.5435	R.0001	.0001	-0.0001	0.0000	-0.0061	ok	5
11.73848345	4.04927176	-0.61654767		.5435	G.0001	.0001	-0.0000	0.0000	-0.0061	ok	5
11.73848345	4.04927176	-0.60956635		.5435	R.0001	.0001	0.0001	0.0000	-0.0061	ok	5
11.73848345	4.04927176	-0.60258504		.5435	R.0001	.0001	0.0001	0.0000	-0.0061	ok	5
11.73848345	4.04927176	-0.59500372		.5435	R.0001	.0001	0.0001	0.0000	-0.0061	ok	5
11.73848345	4.04927176	-0.5886224		.5435	R.0001	.0001	0.0000	0.0000	-0.0061	ok	5
11.73848345	4.04927176	-0.58164108		.5435	R.0001	.0001	-0.0001	0.0000	-0.0061	ok	5
11.73848345	4.04927176	-0.61654767	0.03490659	.5435	Y.0001	.0001	-0.0009	-0.0000	-0.0061	ok	5
11.73848345	4.04927176	-0.61654767	0.02792527	.5435	Y.0001	.0001	-0.0005	0.0000	-0.0061	ok	5
11.73848345	4.04927176	-0.61654767	0.02094395	.5435	Y.0001	.0001	-0.0003	0.0000	-0.0061	ok	5
11.73848345	4.04927176	-0.61654767	0.01396263	.5435	Y.0001	.0001	-0.0001	0.0000	-0.0061	ok	5
11.73848345	4.04927176	-0.61654767	0.00698132	.5435	Y.0001	.0001	-0.0000	0.0000	-0.0061	ok	5
11.73848345	4.04927176	-0.61654767	-.00698132	.5435	Y.0001	.0001	-0.0000	-0.0000	-0.0061	ok	5
11.73848345	4.04927176	-0.61654767	-.01396263	.5435	Y.0001	.0001	-0.0001	-0.0000	-0.0061	ok	5
11.73848345	4.04927176	-0.61654767	-.02094395	.5435	Y.0001	.0001	-0.0003	-0.0000	-0.0061	ok	5
11.73848345	4.04927176	-0.61654767	-.02792527	.5435	Y.0001	.0001	-0.0005	-0.0000	-0.0061	ok	5
11.73848345	4.04927176	-0.61654767	-.03490659	.5435	Y.0001	.0001	-0.0009	0.0000	-0.0061	ok	5

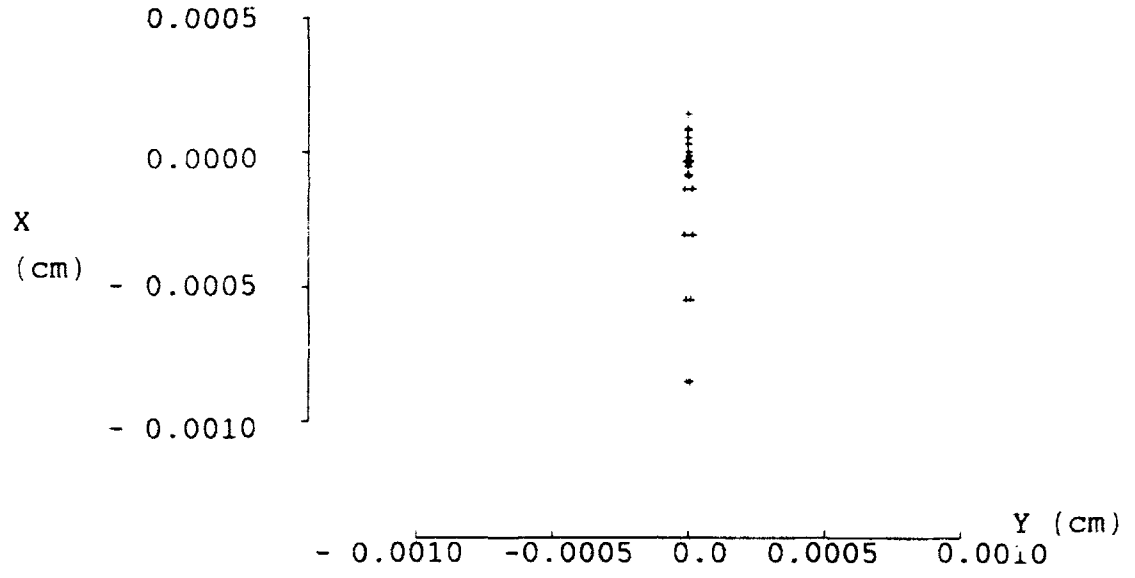

Figure 42 Zero Order Spot Diagram (Cylindrical Mirror)

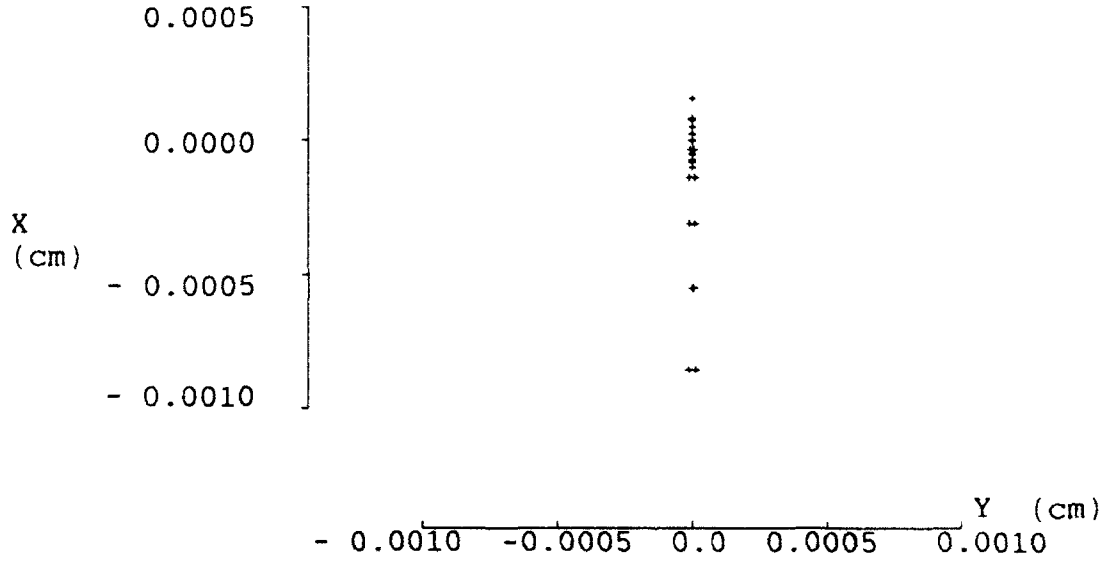

Figure 43 First Order Spot Diagram (Cylindrical Mirror)

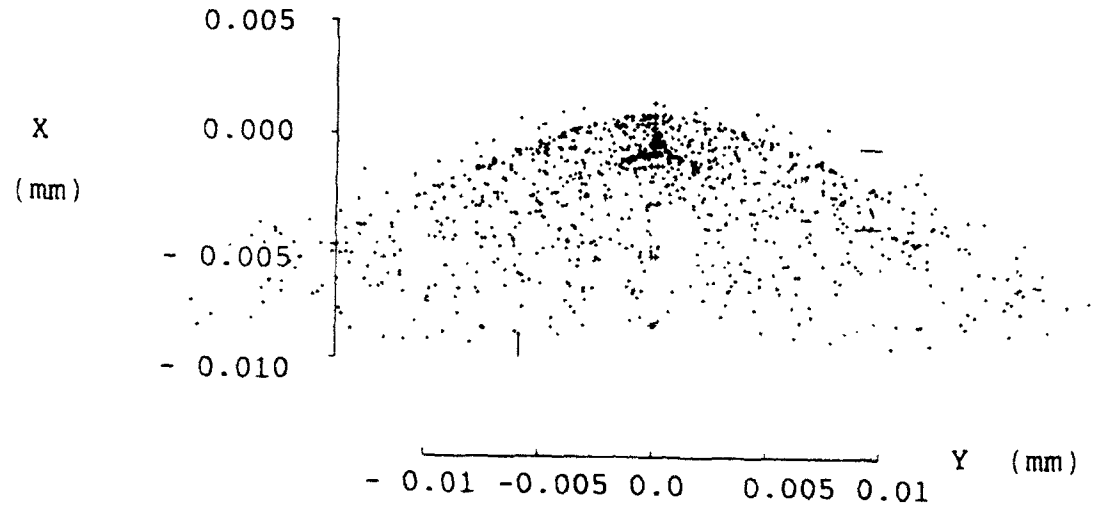

Figure 44 Zero Order Spot Diagram (Cylindrical Mirror)
1000 rays

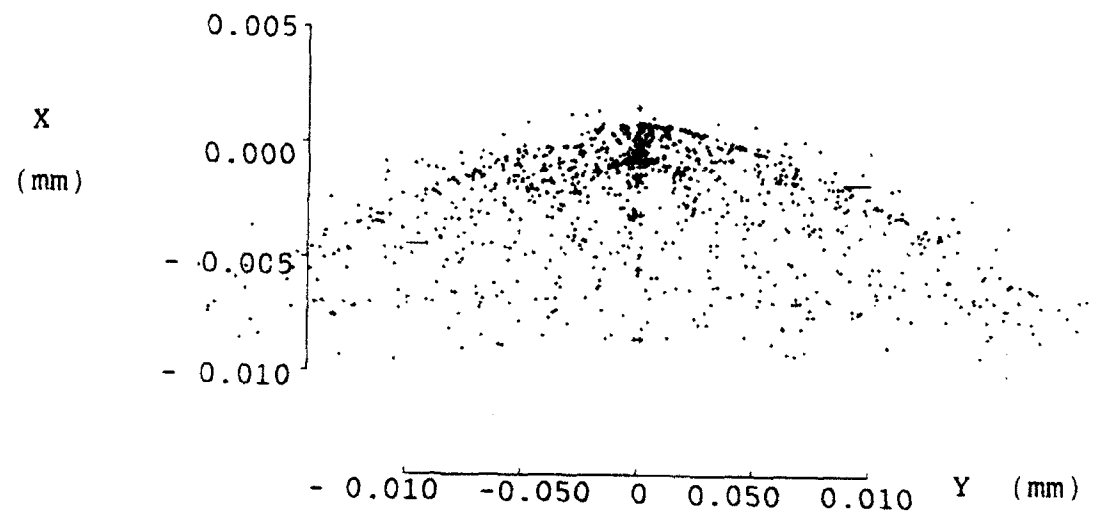

Figure 45 First Order Spot Diagram
1000 rays

APPENDIX C

Spherical Grating 2-D Model Ray Trace Text File : Zero Order (5435 Å Example)

The analysis wavelength is 5435.0000 angstroms.
Aperture data:
Center of Opening (x,y,z): [0.00000, 0.00000, 0.00000]
Aperture dimensions (x,y): [0.01000, 0.01000]
Points across opening (x,y): [1, 1]
Angular beam spread (x,y): [2.000, 2.000]
Number of angles in spread (x,y): [100,100]
Center angle of beam rays (x,y): [0.000, 0.000]
No offset angles are traced.
Aperture shape is rectangular.
Beam spread shape is rectangular.
There are 4 elements:

	x	y	z
The Center of Element 1 coordinate System is	0.000000	0.000000	19.039053
Euler Angles in Degrees:	0.000000	160.967770	0.000000

Spherical Grating with radius of curvature: 20.140 cm and 12000.000 grooves per cm (effective)
Element mask is circular with width 5.000 and height 5.000 cm.

	x	y	z
The Center of Element 2 coordinate System is	11.738483	0.000000	4.049272
Euler Angles in Degrees:	0.000000	321.935537	0.000000

Plane Mirror
Element mask is circular with width 5.000 and height 5.000 cm.

	x	y	z
The Center of Element 3 coordinate System is	0.000000	0.000000	19.039053
Euler Angles in Degrees:	0.000000	160.967770	0.000000

Spherical Grating with radius of curvature: 20.140 cm and 12000.000 grooves per cm (effective)
Element mask is circular with width 5.000 and height 5.000 cm.

	x	y	z
The Center of Element 4 coordinate System is	15.413692	0.000000	-0.643887
Euler Angles in Degrees:	0.000000	321.935537	0.000000

Plane Surface
Element mask is circular with width 1.000 and height 1.000 cm.

There were 10000 rays from all points and angles.
10000 rays hit the detector.
0 failed to hit first element.
0 were stopped after the first.

Spherical Grating 2-D Model Ray Trace Text File : First Order (5435 Å Sample)

The analysis wavelength is 5435.0000 angstroms.

Aperture data:
Center of Opening (x,y,z): [0.00000, 0.00000, 0.00000]
Aperture dimensions (x,y): [0.01000, 0.01000]
Points across opening (x,y): [1, 1]
Angular beam spread (x,y): [2.000, 2.000]
Number of angles in spread (x,y): [100,100]
Center angle of beam rays (x,y): [0.000, 0.000]
No offset angles are traced.
Aperture shape is rectangular.
Beam spread shape is rectangular.

There are 4 elements:

	x	y	z
The Center of Element 1 coordinate System is	0.000000	0.000000	19.039053
Euler Angles in Degrees:	0.000000	160.967769	0.000000

Spherical Grating with radius of curvature: 20.140 cm and 12000.000 grooves per cm (effective)
Element mask is circular with width 5.000 and height 5.000 cm.

	x	y	z
The Center of Element 2 coordinate System is	0.000000	0.000000	0.000006
Euler Angles in Degrees:	0.000000	0.000000	0.000000

Plane Mirror
Element mask is circular with width 5.000 and height 5.000 cm.

	x	y	z
The Center of Element 3 coordinate System is	0.000000	0.000000	19.039053
Euler Angles in Degrees:	0.000000	160.967769	0.000000

Spherical Grating with radius of curvature: 20.140 cm and 12000.000 grooves per cm (effective)
Element mask is circular with width 5.000 and height 5.000 cm.

	x	y	z
The Center of Element 4 coordinate System is	15.413692	0.000000	-0.643887
Euler Angles in Degrees:	0.000000	321.935537	0.000000

Plane Surface
Element mask is circular with width 1.000 and height 1.000 cm.

There were 10000 rays from all points and angles.
10000 rays hit the detector.
0 failed to hit first element.
0 were stopped after the first.

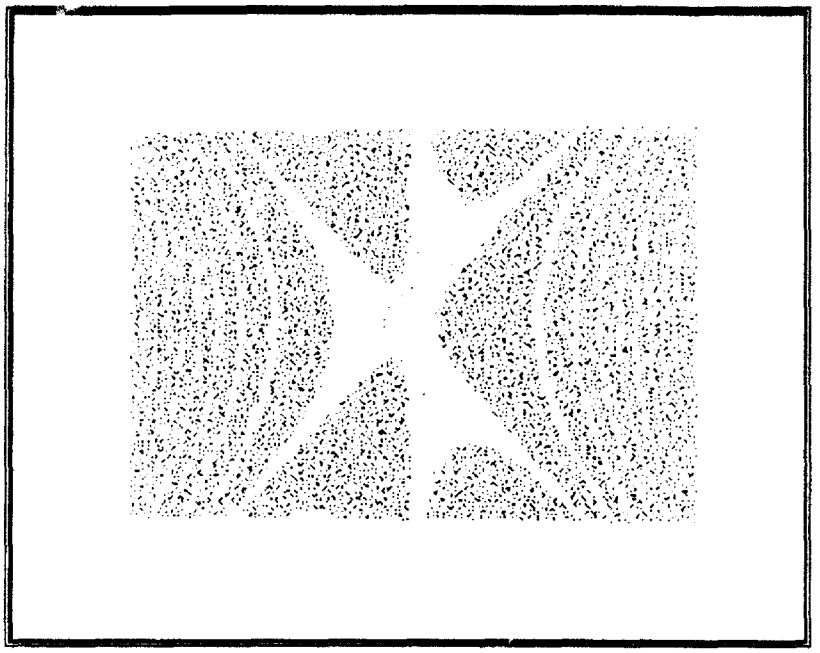

Figure 46 Spherical Grating 5435 Å Interference Pattern

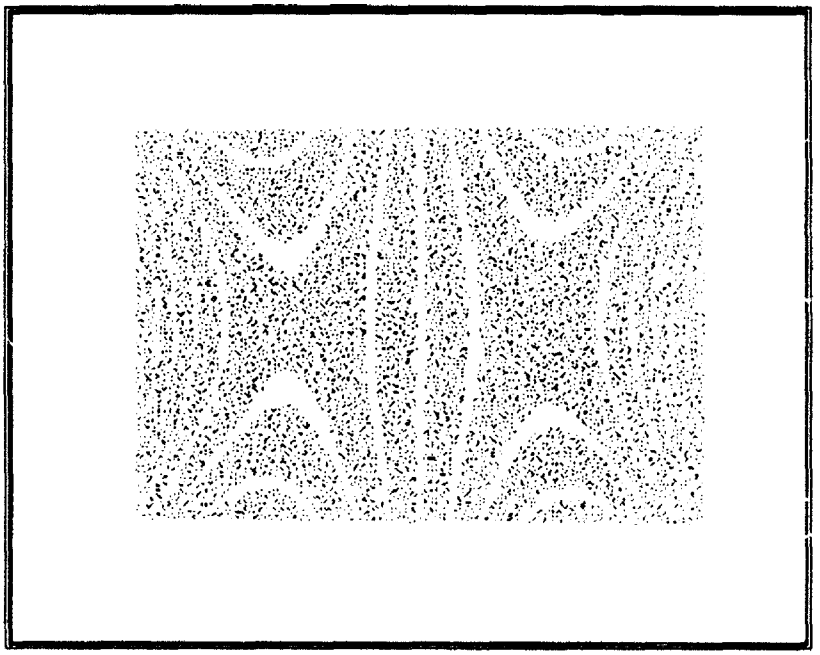

Figure 47 Spherical Grating 5435.5 Å Interference

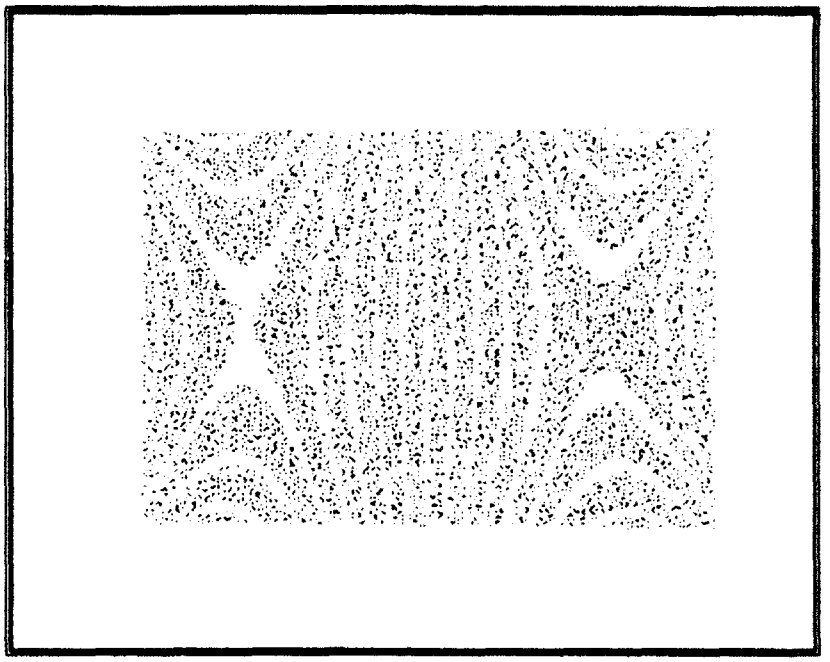

Figure 48 Spherical Grating 5436 Å Interference

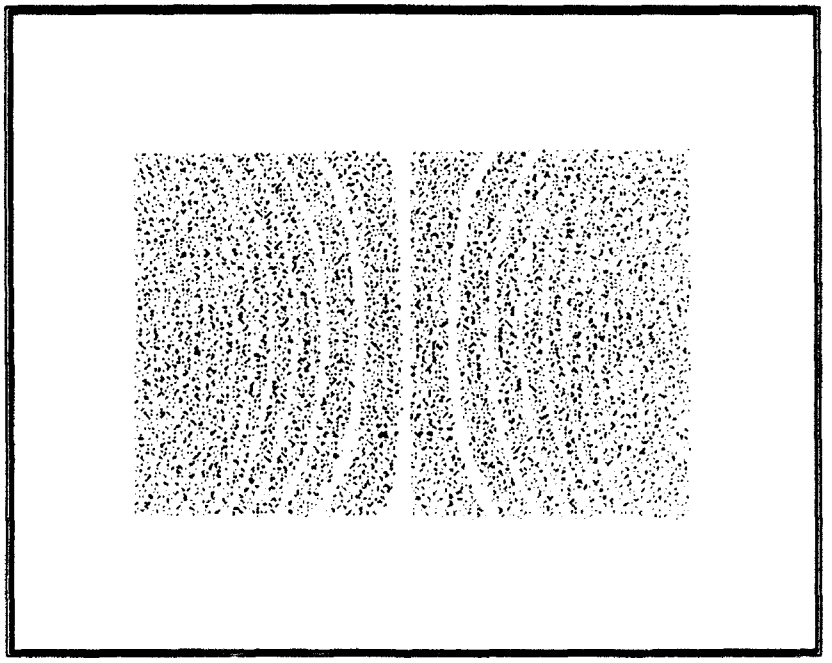

Figure 49 Spherical Grating 5434.5 Å Interference

APPENDIX D

Spatial Heterodyne Model Ray Trace : Zero Order Path Example

The analysis wavelength is 5435.0000 angstroms.
Aperture data:
Center of Opening (x,y,z): [0.00000, 0.00000, 0.00000]
Aperture dimensions (x,y): [1.00000, 1.00000]
Points across opening (x,y): [100, 100]
Angular beam spread (x,y): [0.000, 0.000]
Number of angles in spread (x,y): [1, 1]
Center angle of beam rays (x,y): [0.000, 0.000]
No offset angles are traced.
Aperture shape is rectangular.
Beam spread shape is rectangular.
There are 4 elements:

	x	y	z
The Center of Element 1 coordinate System is	0.000000	0.000000	50.000000
Euler Angles in Degrees:	0.000000	152.000000	0.000000

Plane Grating with 12000.000 grooves per cm and order 0.
Element mask is rectangular with width 3.000 and height 3.000 cm.

	x	y	z
The Center of Element 2 coordinate System is	24.871130	0.000000	33.224210
Euler Angles in Degrees:	0.000000	304.000000	0.000000

Plane Mirror
Element mask is circular with width 2.000 and height 2.000 cm.

	x	y	z
The Center of Element 3 coordinate System is	0.000000	0.000000	50.000000
Euler Angles in Degrees:	0.000000	152.000000	0.000000

Plane Grating with 12000.000 grooves per cm and order 1.
Element mask is rectangular with width 3.000 and height 3.000 cm.

	x	y	z
The Center of Element 4 coordinate System is	47.963830	0.000000	-10.236790
Euler Angles in Degrees:	0.000000	321.471280	0.000000

Plane Surface
Element mask is rectangular with width 2.000 and height 2.000 cm.
There were 10000 rays from all points and angles.
10000 rays hit the detector.
0 failed to hit first element.
0 were stopped after the first.

Spatial Heterodyne Model Ray Trace : Minus One Order Example

The analysis wavelength is 5435.0000 angstroms.

Aperture data:
Center of Opening (x,y,z): [0.00000, 0.00000, 0.00000]
Aperture dimensions (x,y): [1.00000, 1.00000]
Points across opening (x,y): [100, 100]
Angular beam spread (x,y): [0.000, 0.000]
Number of angles in spread (x,y): [1, 1]
Center angle of beam rays (x,y): [0.000, 0.000]
No offset angles are traced.
Aperture shape is rectangular.
Beam spread shape is rectangular.

There are 4 elements:

	x	y	z
The Center of Element 1 coordinate System is	0.000000	0.000000	50.000000
Euler Angles in Degrees:	0.000000	152.000000	0.000000

Plane Grating with 12000.000 grooves per cm and order -1.
Element mask is rectangular with width 3.000 and height 3.000 cm.

	x	y	z
The Center of Element 2 coordinate System is	9.006830	0.000000	21.383970
Euler Angles in Degrees:	0.000000	342.528720	0.000000

Plane Mirror
Element mask is circular with width 2.000 and height 2.000 cm.

	x	y	z
The Center of Element 3 coordinate System is	0.000000	0.000000	50.000000
Euler Angles in Degrees:	0.000000	152.000000	0.000000

Plane Grating with 12000.000 grooves per cm and order 0.
Element mask is rectangular with width 3.000 and height 3.000 cm.

	x	y	z
The Center of Element 4 coordinate System is	47.963830	0.000000	-10.260828
Euler Angles in Degrees:	0.000000	321.471280	0.000000

Plane Surface
Element mask is rectangular with width 2.000 and height 2.000 cm.

There were 10000 rays from all points and angles.

10000 rays hit the detector.
0 failed to hit first element.
0 were stopped after the first.

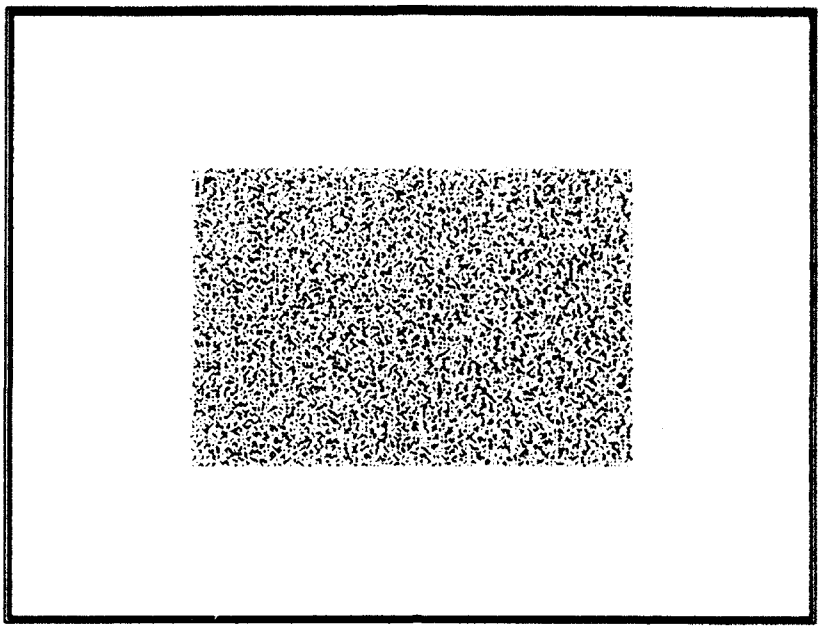

Figure 50 SH Interference at 5435 Å

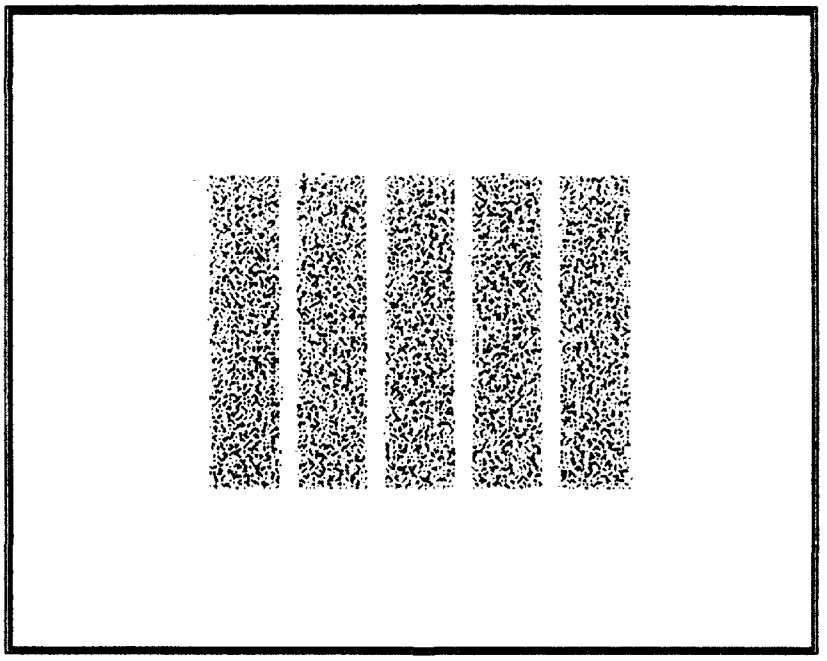

Figure 51 SH Interference at 5434.5 Å

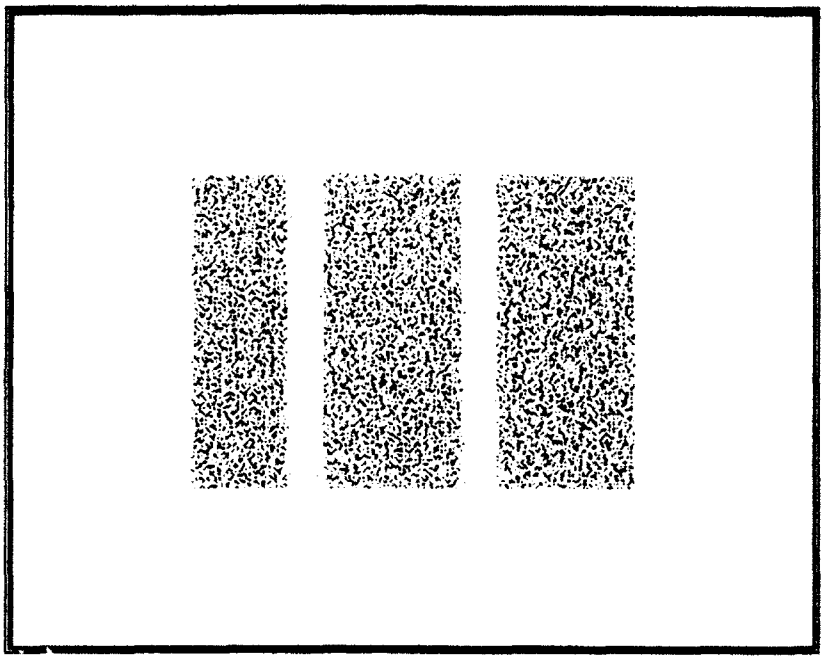

Figure 52 SH Interference at 5435.25 Å

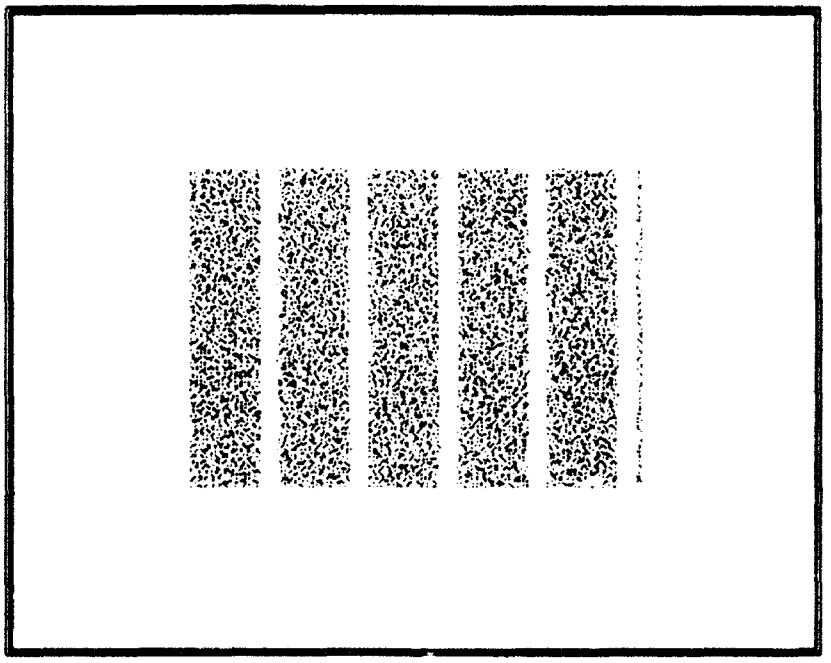

Figure 53 SH Interference for 5435.5 Å

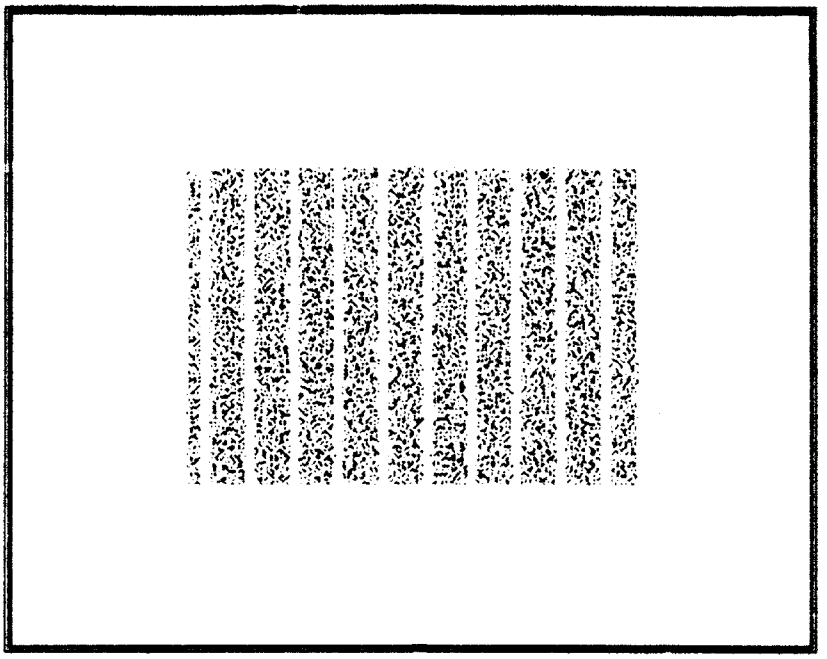

Figure 54 SH Interference at 5436 Å

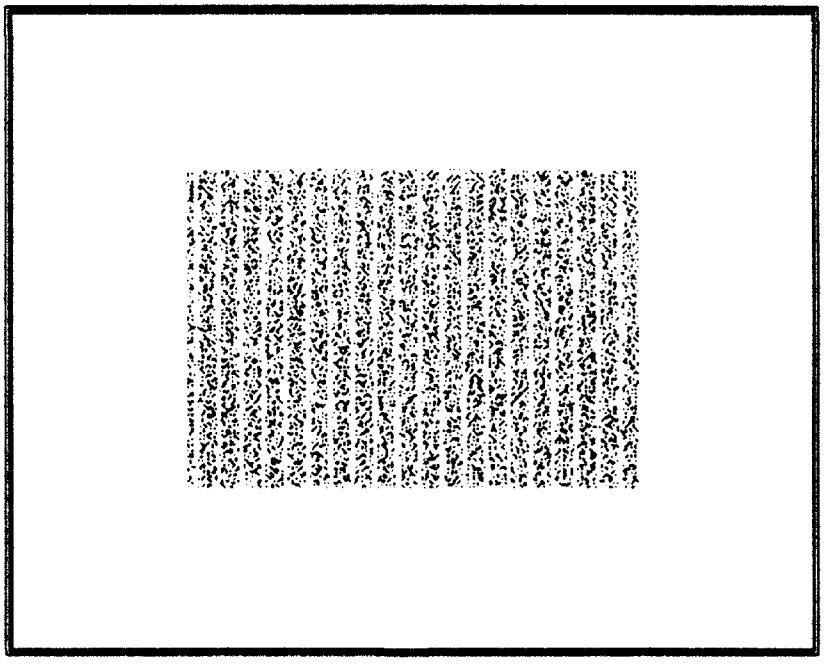

Figure 55 SH Interference 5437 Å

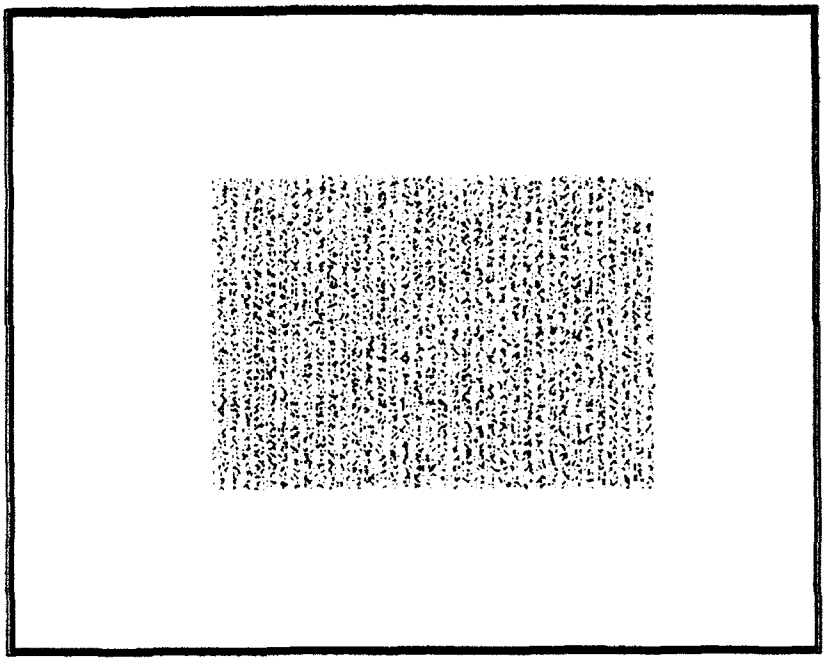

Figure 56 SH Interference First Mirror Rotated 0.025 Degree

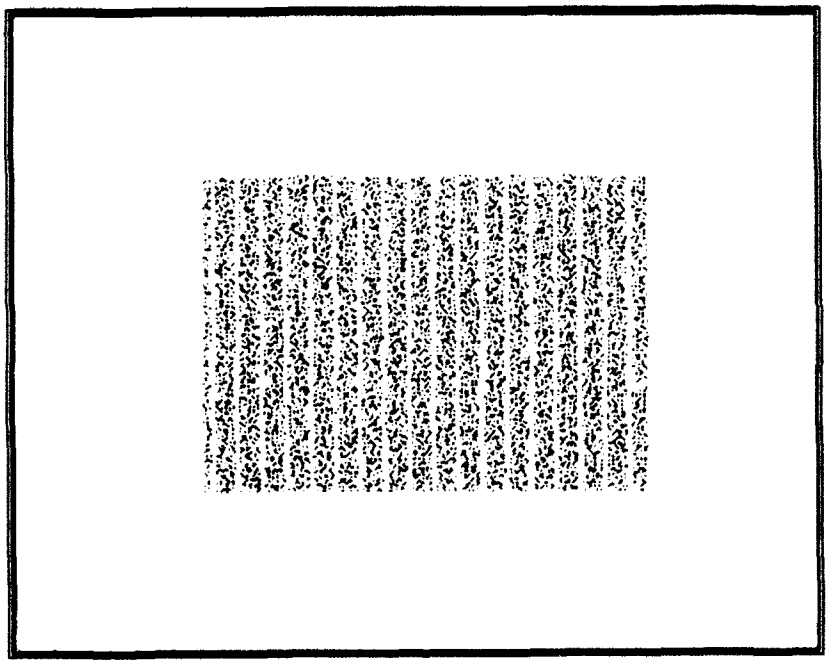

Figure 57 SH Interference First Mirror Rotated 0.0125 Degree

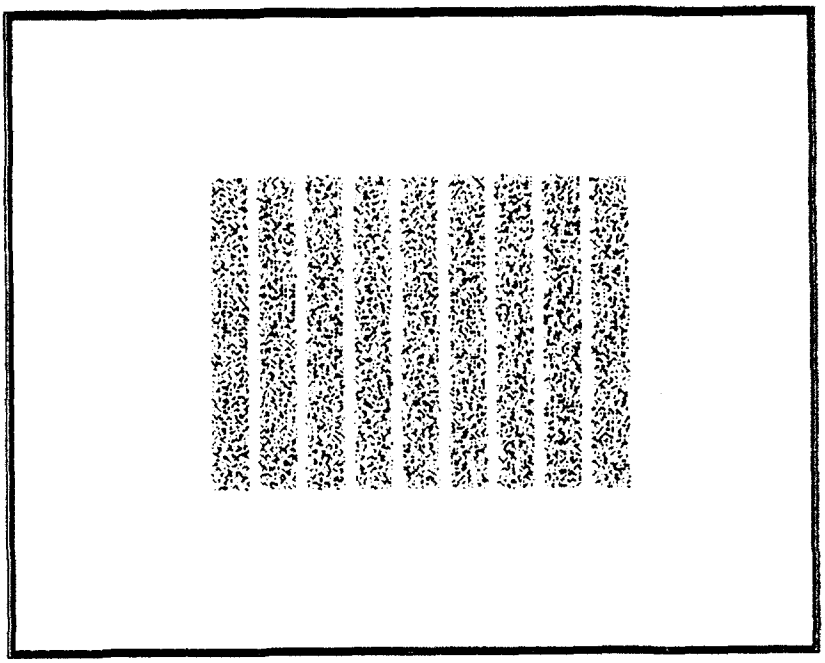

Figure 58 SH Interference First Mirror Rotated 0.00625 Degree

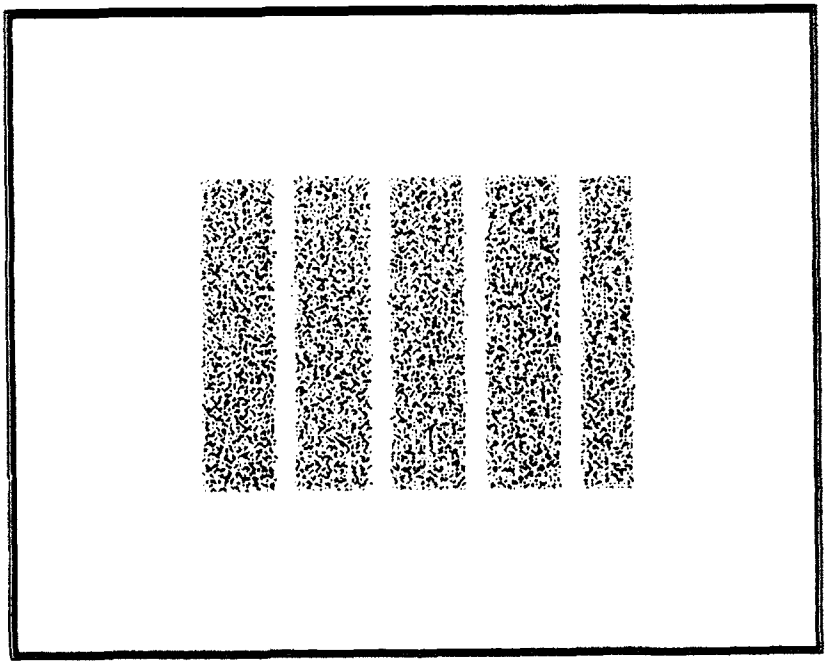

Figure 59 SH Interference First Mirror Rotated 0.00313 Degree

APPENDIX E

SHS Zero Order Oxygen triplet
The analysis wavelength is 1302.17, 1304.87, 1306.04 angstroms.
Aperture data:
Center of Opening (x,y,z): [0.00000, 0.00000, 0.00000]
Aperture dimensions (x,y): [1.00000, 1.00000]
Points across opening (x,y): [100, 100]
Angular beam spread (x,y): [0.000, 0.000]
Number of angles in spread (x,y): [1, 1]
Center angle of beam rays (x,y): [0.000, 0.000]
No offset angles are traced.
Aperture shape is rectangular.
Beam spread shape is rectangular.
There are 4 elements:

	x	y	z
The Center of Element 1 coordinate System is	0.000000	0.000000	25.000000
Euler Angles in Degrees:	0.000000	147.000000	0.000000

Plane Grating with 48000.000 grooves per cm and order 0.
Element mask is rectangular with width 3.000 and height 3.000 cm.

	x	y	z
The Center of Element 2 coordinate System is	22.838640	0.000000	14.831580
Euler Angles in Degrees:	0.000000	294.000000	0.000000

Plane Mirror
Element mask is circular with width 2.000 and height 2.000 cm.

	x	y	z
The Center of Element 3 coordinate System is	0.000000	0.000000	25.000000
Euler Angles in Degrees:	0.000000	147.000000	0.000000

Plane Grating with 48000.000 grooves per cm and order 1.
Element mask is rectangular with width 3.000 and height 3.000 cm.

	x	y	z
The Center of Element 4 coordinate System is	18.307260	0.000000	1.233550
Euler Angles in Degrees:	0.000000	322.392980	0.000000

Plane Surface
Element mask is rectangular with width 2.000 and height 2.000 cm.

There were 30000 rays from all points and angles.
30000 rays hit the detector.
0 failed to hit first element.
0 were stopped after the first.

SHS First Order Oxygen triplet

The analysis wavelength is 1302.17, 1304.87, 1306.04 angstroms.

Aperture data:
Center of Opening (x,y,z): [0.00000, 0.00000, 0.00000]
Aperture dimensions (x,y): [1.00000, 1.00000]
Points across opening (x,y): [100, 100]
Angular beam spread (x,y): [0.000, 0.000]
Number of angles in spread (x,y): [1, 1]
Center angle of beam rays (x,y): [0.000, 0.000]
No offset angles are traced.
Aperture shape is rectangular.
Beam spread shape is rectangular.

There are 4 elements:

	x	y	z
The Center of Element 1 coordinate System is	0.000000	0.000000	25.000000
Euler Angles in Degrees:	0.000000	147.000000	0.000000

Plane Grating with 48000.000 grooves per cm and order -1.
Element mask is rectangular with width 3.000 and height 3.000 cm.

	x	y	z
The Center of Element 2 coordinate System is	11.887910	0.000000	3.007330
Euler Angles in Degrees:	0.000000	331.607020	0.000000

Plane Mirror
Element mask is circular with width 2.000 and height 2.000 cm.

	x	y	z
The Center of Element 3 coordinate System is	0.000000	0.000000	25.000000
Euler Angles in Degrees:	0.000000	147.000000	0.000000

Plane Grating with 48000.000 grooves per cm and order 0.
Element mask is rectangular with width 3.000 and height 3.000 cm.

	x	y	z
The Center of Element 4 coordinate System is	18.307260	0.000000	1.233550
Euler Angles in Degrees:	0.000000	322.392980	0.000000

Plane Surface
Element mask is rectangular with width 2.000 and height 2.000 cm.

There were 30000 rays from all points and angles.
30000 rays hit the detector.
0 failed to hit first element.
0 were stopped after the first.

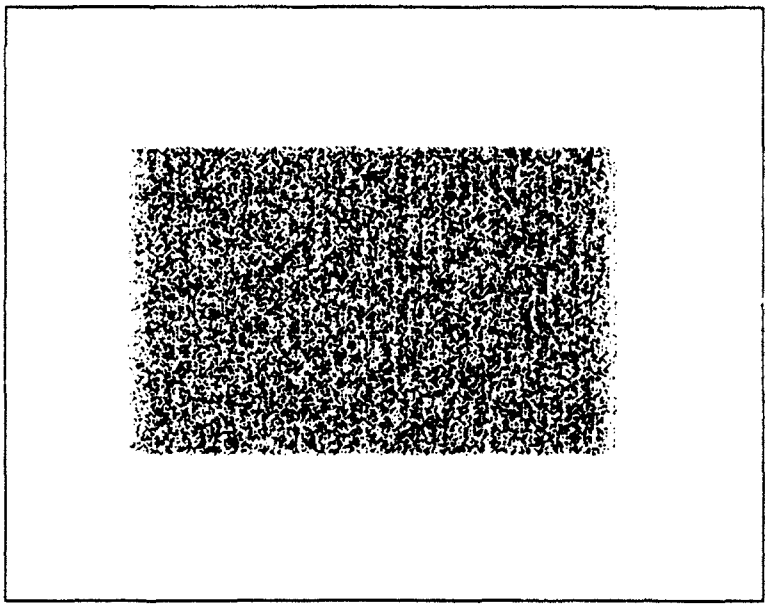

Figure 60 Atomic Oxygen Triplet Interference Pattern

LIST OF REFERENCES

Anderson, C. K., *A Calibration of the Naval Postgraduate School Middle Ultraviolet Spectrograph and an Analysis of the OII 2470 Å and OI 2972 Å Emissions Obtained from Mid-Latitude Rocket Observations*, Masters's Thesis, Naval Postgraduate School, Monterey, California, September 1990.

Atkinson, D., *Implementation and Use of a Computational Ray-Tracing Program for the Design and Analysis of Complex Optical Systems*, Master's Thesis, Naval Postgraduate School, Monterey, California, March 1993.

Banks, P. M. and Kockarts, G., *Aeronomy*, Academic Press, 1973.

Chase, B.E., *A Calibration of the Naval Postgraduate School Middle Ultraviolet Spectrograph (MUSTANG)*, Master's Thesis, Naval Postgraduate School, Monterey, California, September 1992.

Cleary, D. D., Nichols, J. W., and Davis, D. S., "Design for an All-reflection Michelson Interferometer", *Applied Optics*, 31, 433, 1992.

Fonck, R. J., A. Huppler, F. L. Roesler, D. H. Tracy, and M. Daehler, "All-Reflection Michelson Interferometer: Analysis and Test for Far IR Fourier Spectroscopy," *Applied Optics*, 17, 1739, 1978.

Green, A. E. S., and Wyatt, P. J., *Atomic and Space Physics*, Addison-Wesley Publishing Company, Inc., 1965.

Harlander, J., Roesler, F. L., Chakrabarti, S., "Spatial Heterodyne Spectroscopy: A Novel Interferometric Technique for the FUV", *Proceedings of the SPIE*, 1344, 1990.

Hecht, E., *Optics*, 2nd Ed., Addison-Wesley Publishing Company, 1987.

Jenkins, F. A., and White, H. E., *Fundamentals of Optics*, Fourth Ed., McGraw Hill, New York, 1976.

Kingslake, R., *Lens Design Fundamentals*, Academic Press, New York, 1978.

Kruger, R.A., Anderson, L. W., and Roesler, F.L. "All-Reflection Interferometer for Use as a Fourier-Transform Spectrometer," *Journal of the Optical Society of America, 62,938,1972.*

Kruger, R.A., Anderson, L. W., and Roesler, F. L., "New Fourier Transform All-Reflection Interferometer," *Applied Optics*, 12, 533, 1973.

Mihalas, D., *Stellar Atmospheres*, W.H. Freeman and Company, New York, 1978.

Nichols, J., *The Design of a New Far Ultraviolet Interferometer for Ionospheric Spectroscopy*, Master's Thesis, Naval Postgraduate School, Monterey, California, December 1990.

Tousey R., "Ultraviolet Spectroscopy of the Sun," *Space Astrophysics*, McGraw Hill, New York, 1961.

Webb, R. H., *Elementary Wave Optics*, Academic Press, New York, 1969.

Wiese, W. L., Smith, M. W., and Glennon, B. M., *Atomic Transition Probabilities*, U.S.Government Printing Office, 1966.

Young M., *Optics and Lasers*, 3rd Ed., Springer-Verlag, 1986.

BIBLIOGRAPHY

Chang, B.J., Alferness, R.,and Leith, E.N., "Space-invariant Achromatic Grating Interferometers: Theory," *Applied Optics*, 14,1592, 1975.

Cheng, Y., "Fringe Formation in Incoherent Light with a Two-Grating Interferometer," *Applied Optics*, 23, 3057, 1984.

Duffieux, P. M., *The Fourier Transform and Its Applications to Optics*, John Wiley & Sons, 1983.

National Research Council, *The Upper Atmosphere and Magnetosphere*, National Academy of Sciences, 1977.

Steel, W.H., *Interferometry*, 2nd Ed., Cambridge University Press, 1987.

Wu, J., Chen, L., and Jiang, T., "*Imaging 2-D Objects with a Grating Interferometer: Two Methods*," *Applied Optics*, 29, 1225, 1990.

Young, H. D., *Optics and Modern Physics*, McGraw Hill, 1968.

INITIAL DISTRIBUTION LIST

1.	Defense Technical Information Center Cameron Station Alexandria, VA 22304-6145	2
2.	Library, Code 52 Naval Postgraduate School Monterey, CA 93943-5002	2
3.	Dr. K. W. Woehler, Chairman PH Physics Department Naval Postgraduate School Monterey, CA 93943-5000	1
4.	Dr. D. J. Collins, Chairman AA Aeronautics and Astronautics Department Naval Postgraduate School Monterey, CA 93943-5000	1
5.	Dr. D. D. Cleary, Code PH/Cl Physics Department Naval Postgraduate School Monterey, CA 93943-5000	3
6.	Dr. O. Biblarz, Code AA/Bi Aeronautics and Astronautics Department Naval Postgraduate School Monterey, CA 93943-5000	1
7.	LCDR Kenneth Wallace 2603 Rollingwood Drive Austin, TX 78746	1
8.	Dr. Larry Paxton Mail Stop 24-E115 Applied Physics Laboratory Johns Hobkins Road Laurel, MD 20723	1